SANDIA REPORT
SAND2009- 0244
Unlimited Release
Printed JAN 2009

Microscale Immune Studies Laboratory

Anup K Singh, Tony Martino, Jean-Loup Faulon, Chris Apblett, Mark van Benthem, Cathy Branda, Steve Branda, Allan Brasier, Jim Brennan, Susan Brozik, Elizabeth Carles, Amanda Carroll-Portillo, Bryan Carson, Ryan Davis, Elsa Ndiaye-Dulac, Jean-Loup Faulon, Paul Gemperline, David Haaland, Amy Herr, Conrad James, Howland Jones, Jaewook Joo, Julie Kaiser, Glenn Kubiak, Todd Lane, Diane Lidke, Ron Manginell, Shawn Martin, Milind Misra, Matt Moorman, Jaclyn Murton, Kamlesh Patel, Thomas Perroud, Steve Plimpton, Jens Poschet, Roberto Rebeil, Susan Rempe, Ron Renzi, Bryce Ricken, Ken Sale, William Seaman, Mike Sinclair, Nimisha Srivastava, Dan Throckmorton, Meiye Wu, Zhaoduo Zhang

Sandia National Laboratories, Albuquerque and Livermore, CA

Prepared by
Sandia National Laboratories
Albuquerque, New Mexico 87185 and Livermore, California 94550

Sandia is a multiprogram laboratory operated by Sandia Corporation,
a Lockheed Martin Company, for the United States Department of Energy's
National Nuclear Security Administration under Contract DE-AC04-94AL85000.

Approved for public release; further dissemination unlimited.

Sandia National Laboratories

Issued by Sandia National Laboratories, operated for the United States Department of Energy by Sandia Corporation.

NOTICE: This report was prepared as an account of work sponsored by an agency of the United States Government. Neither the United States Government, nor any agency thereof, nor any of their employees, nor any of their contractors, subcontractors, or their employees, make any warranty, express or implied, or assume any legal liability or responsibility for the accuracy, completeness, or usefulness of any information, apparatus, product, or process disclosed, or represent that its use would not infringe privately owned rights. Reference herein to any specific commercial product, process, or service by trade name, trademark, manufacturer, or otherwise, does not necessarily constitute or imply its endorsement, recommendation, or favoring by the United States Government, any agency thereof, or any of their contractors or subcontractors. The views and opinions expressed herein do not necessarily state or reflect those of the United States Government, any agency thereof, or any of their contractors.

Printed in the United States of America. This report has been reproduced directly from the best available copy.

Available to DOE and DOE contractors from
U.S. Department of Energy
Office of Scientific and Technical Information
P.O. Box 62
Oak Ridge, TN 37831

Telephone: (865)576-8401
Facsimile: (865)576-5728
E-Mail: reports@adonis.osti.gov
Online ordering: http://www.osti.gov/bridge

Available to the public from
U.S. Department of Commerce
National Technical Information Service
5285 Port Royal Rd
Springfield, VA 22161

Telephone: (800)553-6847
Facsimile: (703)605-6900
E-Mail: orders@ntis.fedworld.gov
Online order: http://www.ntis.gov/help/ordermethods.asp?loc=7-4-0#online

SAND 2009- 0244
Unlimited Release
Printed January 2009

Microscale Immune Studies Laboratory

Anup Singh, Tony Martino, Jean-Loup Faulon, Chris Apblett, Mark van Benthem, Cathy Branda, Steve Branda, Allan Brasier[1], Jim Brennan, Susan Brozik, Elizabeth Carles, Amanda Carroll-Portillo, Bryan Carson, Ryan Davis, Elsa Ndiaye-Dulac, Jean-Loup Faulon, Paul Gemperline[2], David Haaland, Amy Herr, Conrad James, Howland Jones, Jaewook Joo, Julie Kaiser, Glenn Kubiak, Todd Lane, Diane Lidke[3], Ron Manginell, Shawn Martin, Milind Misra, Matt Moorman, Jaclyn Murton, Kamlesh Patel, Thomas Perroud, Steve Plimpton, Jens Poschet, Roberto Rebeil, Susan Rempe, Ron Renzi, Bryce Ricken, Ken Sale, William Seaman[4], Mike Sinclair, Nimisha Srivastava, Dan Throckmorton, Meiye Wu, Zhaoduo Zhang

Sandia National Laboratories, Albuquerque, NM and Livermore, CA
[1] The University of Texas Medical Branch, Galveston, TX
[2] East Carolina University, Greenville, NC
[3] University of New Mexico, Albuquerque, NM
[4] University of California, San Francisco, CA

OVERVIEW

Our overarching goal is to develop novel technologies to elucidate molecular mechanisms of the innate immune response in host cells to pathogens such as bacteria and viruses including the mechanisms used by pathogens to subvert/suppress/obfuscate the immune response to cause their harmful effects.

Innate immunity is our first line of defense against a pathogenic bacteria or virus. A comprehensive “system-level” understanding of innate immunity pathways such as

toll-like receptor (TLR) pathways is the key to deciphering mechanisms of pathogenesis and can lead to improvements in early diagnosis or developing improved therapeutics. Current methods for studying signaling focus on measurements of a limited number of components in a pathway and hence, fail to provide a systems-level understanding.

We have developed a systems biology approach to decipher TLR4 pathways in macrophage cell lines in response to exposure to pathogenic bacteria and their lipopolysaccharide (LPS). Our approach integrates biological reagents, a microfluidic cell handling and analysis platform, high-resolution imaging and computational modeling to provide spatially- and temporally-resolved measurement of TLR-network components. The integrated microfluidic platform is capable of imaging single cells to obtain dynamic translocation data as well as high-throughput acquisition of quantitative protein expression and phosphorylation information of selected cell populations. The platform consists of multiple modules such as single-cell array, cell sorter, and phosphoflow chip to provide confocal imaging, cell sorting, flow cytomtery and phosphorylation assays. The single-cell array module contains fluidic constrictions designed to trap and hold single host cells. Up to 100 single cells can be trapped and monitored for hours, enabling detailed statistically-significant measurements. The module was used to analyze translocation behavior of transcription factor NF-kB in macrophages upon activation by E. coli and Y. pestis LPS. The chip revealed an oscillation pattern in translocation of NF-kB indicating the presence of a negative feedback loop involving IKK. Activation of NF-kB is preceded by phosphorylation of many kinases and to correlate the kinase activity with translocation, we performed flow cytomteric assays in the PhosphoChip module. Phopshorylated forms of p38, ERK and RelA were measured in macrophage cells

challenged with LPS and showed a dynamic response where phosphorylation increases with time reaching a maximum at ~30-60min. To allow further downstream analysis on selected cells, we also implemented an optical-trapping based sorting of cells. This has allowed us to sort macrophages infected with bacteria from uninfected cells with the goal of obtaining data only on the infected (the desired) population. The various microfluidic chip modules and the accessories required to operate them such as pumps, heaters, electronic control and optical detectors are being assembled in a bench-top, semi-automated device. The data generated is being utilized to refine existing TLR pathway model by adding kinetic rate constants and concentration information.

The microfluidic platform allows high-resolution imaging as well as quantitative proteomic measurements with high sensitivity (<pM) and time-resolution (~15 s) in the same population of cells, a feat not achievable by current techniques. Furthermore, our systems approach combining the microfluidic platform and high-resolution imaging with the associated computational models and biological reagents will significantly improve our ability to study cell-signaling involved in host-pathogen interactions and other diseases such as cancer.

The advances made in this project have been presented at numerous national and international conferences and are documented in many peer-reviewed publications as listed below. Finer details of many of the component technologies are described in these publications. The chapters to follow in this report are also adapted from other manuscripts that are accepted for publication, submitted or in preparation to be submitted to peer-reviewed journals.

MISL- List of Publications:

nature Molecular Descriptor." Bioinformatics 24 (2008): 225-33.

2. Gray, G.A., Williams, P.J., Brown, W.M, Faulon, J-L., Sale K.L. "Disparate Data Fusion for Protein Phosphorylation Prediction." Annals of Operations Research Special Volume on Data Mining, in press, 2008.
3. Hatch A. V., AE Herr, DJ Throckmorton, JS Brennan, and AK Singh. "Integrated Preconcentration SDS-PAGE of Proteins in Microchips Using Photopatterned Cross-Linked Polyacrylamide Gels." *Analytical Chemistry*, 2006, 78(14), 4976 – 4984
4. James, C.D., Reuel, N., Lee, E.S., Davalos, R.V., Mani, S.S., Carroll-Portillo, A., Rebeil, R., Martino, A., Apblett, C. "Impedimetric and Optical Interrogation of Single Cells in a Microfluidic Device for Real-Time Viability and Chemical Response Assessment." Biosensors and Bioelectronics 23 (2008): 845-861.
5. Joo, J., Plimpton, S., Martin, S., Swiler, L., Slepoy, A., Faulon, J-L. "Sensitivity Analysis of Computational Model of the NF-κB-IκB-A20 Signal Transduction Network." Ann N Y Acad Sci. 1115 (2007): 221-39.
6. Martin, S., Zhang, Z., Martino, A. Faulon, J-L. "Boolean Dynamics of Genetic Regulatory Networks Inferred From Microarray Time Series Data." Bioinformatics 23 (2007): 866-74.
7. Perroud, T.D.; Kaiser, J.N.; Sy, J.C.; Lane, T.W.; Branda, C.S.; Singh, A.K.; Patel, K.D. "Microfluidic-Based Cell Sorting of *Francisella tularensis* Infected Macrophages using Optical Forces." Analytical Chemistry, 2008.
8. Sinclair, M.B, Haaland, D.M., Timlin, J.A., Jones, H.D.T. "Hyperspectral Confocal Microscope." Applied Optics 45, (2006) 6283-6291.
9. Van Benthem, M.H., Keenan, M.R., Davis, R., Liu, P., Jones, H.D.T., Haaland, D.M., Sinclair, M.B., Brasier, A.R. "Trilinear Analysis Of Images Obtained With A Hyperspectral Imaging Confocal Microscope." Journal of Chemometrics, 2008.
10. Van Benthem, M.H., Keenan, M.R. "Tucker1 Model Algorithms For Fast Solutions To Large Parafac Problems." Journal of Chemometrics, 2008.
11. Perroud, T.D.; Renzi, R.; Singh, A.K.; Patel, K.D Overlapping Wet Etch Fronts for 3D Hydrodynamic Focusing, Particle Concentration, and Trapping Single Cells, Lab Chip, 2009, in press.
12. Jones, H.D.T., Haaland, D.M., Sinclair, M.B., Melgaard, D.K., Van Benthem, M.H., Pedroso, M.C. "Weighting Hyperspectral Image Data for Improved Multivariate Curve Resolution Results." Journal of Chemometrics, January 2008.
13. Patrick J. Cutler, David M. Haaland, Erik Andries, and Paul J. Gemperline, "Methods for Kinetic Modeling of Temporally Resolved Hyperspectral Confocal Fluorescence Images," Applied Spectroscopy, 2009, in press.
14. Patrick J. Cutler, David M. Haaland, and Paul J. Gemperline, "Systematic Method for the Kinetic Modeling of Temporally-Resolved Hyperspectral Microscope Images of Fluorescently Labeled Cells," Applied Spectroscopy, 2009, in press.
15. David M. Haaland, Howland D. T. Jones, Mark H. Van Benthem, Michael B. Sinclair, David K. Melgaard, Christopher L. Stork, Maria C. Pedroso, Ping Liu, Allan R. Brasier, Nicholas L. Andrews, and Diane S. Lidke, "Hyperspectral

Confocal Fluorescence Imaging: Exploring Alternative Multivariate Curve Resolution Approaches," Applied Spectroscopy, 2009, in press.

.

Contents

1. Introduction **8**

2. Microfluidic Single-Cell Array for Live Imaging of Host-Pathogen Interaction **10**

3. Microfluidically-unified cell challenge, preparation and flow cytometry allows automated phosphoprofiling of macrophage response to lipopolysaccharide **37**

4. Microfluidic-Based Cell Sorting of Francisella tularensis Infected Macrophages using Optical Forces **70**

5. Dosage-dependent heterogeneous NF-kB response to LPS stimulation: computational model and single cell experiment **98**

6. Novel statistical ensemble analysis for simulating heterogeneous response in NF-kB signaling network **127**

7. Different lipopolysaccharide chemotypes provoke a common Toll-like receptor 4 mediated response to different degrees **165**

42

1. Introduction

While considerable progress has been made towards understanding signaling pathways of the innate immune system, as toll-like receptor (TLR) signaling (Comelis, 2002), serious gaps exist in our knowledge. (Janssens and Beyaert, 2003; Comelis et al., 1998) For example, the interconnections between pathways, the interactions between proteins, and the modifications to proteins that occur during signaling are incompletely understood. Moreover, the existing signaling pathway models lack both quantitative and kinetic information. Furthermore, existing techniques do not provide detailed spatial information (e.g., localization) regarding the signaling events inside a cell.

To develop a molecular- and cellular-level understanding of the innate immune system, protein concentrations and reaction kinetics of pathway activation must be quantified at the single-cell level. Cells in a population do not all have the same initial physiological state or degree of infection.(McAdams, Arkin, *PNAS*, 1997; Swain *et al.*, *PNAS*, 2002; Blake *et al. Nature* 2003). Consequently, measurement of the cellular signaling pathway is not accurately represented from data averaged over a population of cells.(Irish *et al.*, *Cell* 2004; Irish *et al.*, *Nat Rev Cancer*, 2006) Further compounding the challenge are feedback characteristics (primary *vs*. secondary signaling) inherent to the innate immune system, which can be lost in population-averaged measurements.(e.g., Paszek *et al.*, *J Theor Biol.* 2005). Thus, to construct a cellular-level understanding of the innate immune response, an ensemble of responses – measured at the level of the individual cells – is required. (Lipniacki *et al.*, *Biophys J*, 2006)

Our approach aims to tease apart the response of the TLR4 signaling pathway by quantifying this signaling network in macrophage and epithelial cells challenged with lipopolysaccharide (LPS) and pathogenic bacteria. Through development of a high-throughput measurement and analysis

instrument capable of measuring protein concentrations, states, and interactions in host cells, we will obtain temporal, spatial, and cell-state information comprising the basis of the innate immune system. Specifically, the instrument design enables multiplexed measurements of single cells, individually or as part of a population, under well-controlled conditions – something nearly impossible with current bench top technologies. Validation of the system is achieved by integrating data generated through bench top biological experimentation and information acquired through use of the nascent microengineered platform with predictive models. In short, ***we propose to develop an integrated high-throughput experimental and computational approach that provides "system-level" quantitative spatio-temporal data with single-cell resolution for the TLR pathway.***

2. Microfluidic Single-Cell Array for Live Imaging of Host-Pathogen Interactions

Conrad D. James, Matthew W. Moorman, Ronald P. Manginell, Jeffrey W. Lantz, Catherine S. Branda, Bryan Carson, Roberto Rebeil, Anthony Martino, Anup K. Singh

Abstract:

We have developed a microfluidic single cell array (SCA) device that provides host cell immobilization and long-term high-resolution imaging to monitor toll-like receptor (TLR) signaling pathways involved in host-pathogen interactions. The device contains fluidic constrictions designed to trap and hold single host cells and to minimize the pressure gradient across trapped cells. Up to 100 single cells can be trapped and monitored for hours, enabling detailed statistically-significant measurements on immune response in host cells. The device contains the key advantage of fluidic isolation of single host cells by preventing direct contact between cells and eliminating interactions with substances secreted by neighboring cells. This provides the capability to differentiate between primary and secondary signaling in innate immune response. Here, we examine the cell trapping and fluidic isolation capabilities of the device through computational simulations and experimental verification. In addition, we have quantitatively measured the effect of lipopolysaccharide (LPS) and live pathogenic bacteria on activation of the TLR4 pathway in the RAW264.7 murine macrophage-like cell line. This was achieved by activating RAW264.7 cells with the pathogen challenge and monitoring the subsequent cytoplasm-to-nucleus translocation kinetics of a green fluorescent protein fusion construct to the transcription factor subunit RelA (GFP-RelA). This work presents the

first demonstration of single host-cell infection on a microfluidic platform with live imaging of the infection sequence and early immune signaling events.

Keywords: macrophage, immune response, microfluidics, single cell analysis, TLR4

Introduction

The innate immune system represents our first line of defense against microbial pathogens. In this system, sentry cells such as macrophages detect pathogen-associated molecular patterns (PAMPs) using single-pass integral membrane proteins called Toll-like receptors (TLRs) [1]. Macrophages express at least ten different TLRs, each recognizing a particular PAMP; for instance, TLR4 is a cell-surface receptor that specifically recognizes lipopolysaccharide (LPS) components of the bacterial cell envelope [Fig. 1a]. Activation of a TLR sets in motion a signal transduction cascade that ultimately regulates the activity of transcription factors such as NFκB, which in turn regulate production of effector proteins such as pro-inflammatory enzymes and secreted signaling molecules such as cytokines. Specifically, NFkB, which is a heterodimer of the proteins RelA and p50, translocates from the cytoplasm to the nucleus during host cell activation [2]. This sequence of events constitutes the TLR network's “primary” response to the PAMP. Follow-on “secondary” responses are induced through two different mechanisms: 1) intracellular feedback loops, whereby proteins up-regulated during the primary response act directly on the TLR network; and 2) extracellular signaling, whereby proteins (such as cytokines) secreted by the host cell during the primary

response activate receptor-mediated signaling pathways that cross-talk with the TLR network. Summation of these responses is thought to largely determine the macrophage's initial reaction to a pathogen. Indeed, TLR networks are specifically targeted for subversion by *F. tularensis* and *Y. pestis*, pathogens which successfully escape being killed by the macrophage.

Due to its central importance in combating these and other pathogens, the TLR4 network has been intensively studied in recent years. Many of the protein components of the networks have been identified, but our current understanding of whole-network behavior is still lacking, especially at the level of single cell responses. Current analyses with conventional techniques such as microarrays, ELISAs, and westerns are all performed at the population level. This presents significant challenges to interpreting measured responses for several reasons. First, cells in a population do not all reside in the same initial physiological state or degree of infection [3-5], consequently, measurement of the cellular signaling pathway is not accurately represented from data averaged over a population of cells [6-11]. Second, feedback characteristics (primary *vs*. secondary signaling) inherent to the innate immune system can be lost in population-averaged measurements [12]. Thus, to construct a cellular-level understanding of the innate immune response, an ensemble of responses – measured at the level of the individual cells – is required [13].

Several interrogation techniques have been implemented in microfluidic systems in order to monitor dynamic changes in single living cells over time, including impedance spectroscopy [14, 15], electrochemical detection [16], and optical microscopy [17, 18]. Recently, microfluidics technology has been extended to study host-pathogen interactions

[19]. In addition, microfluidic systems have been developed to assess the response of osteoblasts to secreted factors from stimulated macrophages [20], and to measure changes in gene transcription in HeLa cells after cytokine exposure [21]. However, all of these studies have utilized host cells that are pooled into common chambers where cells are in direct contact with or within the near vicinity of other cells. Thus, it is difficult to determine the role of primary vs. secondary signaling in the host cell response.

We report here a single cell array (SCA) microfluidic chip for holding single host cells in pre-defined locations for long-term live-cell imaging of host-pathogen interactions. Host cells are prevented from having direct contact with other host cells, and the microfluidic architecture of the chip design prevents chemical communication between host cells through diffusible secreted substances. These features enable novel experiments to be performed in which the effects of such cell-cell interactions can be examined. The device was demonstrated with RAW264.7 macrophage-like cells challenged with live *E. coli* bacteria or LPS purified from *E. coli* bacteria. Host cell activation was measured quantitatively with a GFP-RelA fusion construct through optically monitoring the translocation of RelA from the cytoplasm to the nucleus upon pathogen-induced activation of NFκB.

Materials and methods

Host cell and pathogen preparation

RAW264.7 murine macrophage-like cells were prepared to express a GFP construct to visualize translocation of RelA from the cytoplasm to the nucleus. The $p_{\beta Actin}$-EGFP-RelA construct was derived from pECFP-F-RelA, a kind gift from Dr. Allan Brasier (University of Texas Medical Branch). ECFP was replaced with EGFP between the Age1 and BsrG1 sites, and the cytomegalovirus (CMV) promoter was replaced with a minimal 106bp human βActin promoter [22] cloned between the Ase1 and Nhe1 sites to reduce the average expression below toxic levels. The plasmid pBA-GFP-RelA was linearized with AflII (New England Biolabs) and used to transfect RAW264.7 murine macrophage-like cells (ATCC) by Nucleofection (Amaxa Biosystems). Transfected cells were grown for 12 days in the presence of 800 ug/ml G418, and a clone stably expressing GFP-RelA was isolated. For subsequent experiments, cells were grown on untreated polystyrene dishes in DMEM supplemented with 10% fetal bovine serum (ATCC), 2mM L-glutamine, 1mM sodium pyruvate, 1x MEM nonessential amino acids, 20mM HEPES, 100 I.U./ml penicillin, and 100µg/ml streptomycin (all supplements from Mediatech) at 37°C with 5% CO_2. Cells were harvested at 50-80% confluence using a non-enzymatic cell dissociation reagent (CellStripper, Mediatech), and >95% viability was verified by Trypan blue staining. Harvested cells were resuspended at 5-10x10^5 cells/ml in complete pre-equilibrated (37°C, 5% CO_2 in air, >30min) medium containing 250ng/ml propidium iodide (PI, Calbiochem) and 2ug/ml Hoechst 33258 (Molecular Probes) dyes for live/dead cell and cell nucleus visualization, respectively.

Immune response experiments on RAW264.7 cells were conducted by preparing *E. coli* LPS (Sigma Aldrich) in pre-equilibrated medium at different concentrations (1,

100, and 1000 nM). The first panel of Figure 1b shows a quiescent population of RAW264.7 cells grown on a coverslip with GFP-RelA concentrated within the cytoplasm. The second panel shows a different field of view on the same coverslip fifteen minutes after continuous incubation with 1 μM *E. coli* LPS. By this time, the GFP-RelA has translocated into the nucleus. Here, we see that direct contact and diffusion of chemical substances between cells is difficult to eliminate using conventional experiments on coverslips.

Immune response experiments with live bacteria were also performed. TOP10 *E. coli* (Invitrogen) were transformed with pAsRed2 (Clontech) and grown to stationary phase in LB with 100ug/ml ampicillin. Prior to use, fresh cultures were started at 0.05 OD600 in DMEM-10 mammalian cell culture medium without penicillin or streptomycin but with 100ug/ml ampicillin. Cells were grown to mid log phase (0.4-0.8 OD600), pelleted at 2000xg for 10min, then resuspended in fresh DMEM-10 immediately prior to the experiment. After RAW264.7 cells were challenged with E. coli, GFP-RelA translocated from the cytoplasm to the nucleus in similar fashion to the purified LPS experiments.

SCA Device Design

The single cell array chip is designed to capture multiple single cells in predefined locations for high-resolution imaging of host cell immune response to stimulants. The SCA architecture provides the ability to physically isolate single cells from direct contact with other cells, and to fluidically isolate cells from diffusible substances secreted by

other cells. Figure 2 shows the layout of the SCA chip. The chip contains two separate inlet channels with 200 μm diameter inlet/outlet ports. Channels are initially 100 μm wide and neck down to 50 μm wide prior to the cell imaging regions. Both channels feed to a common outlet on the other side of the chip. The inlets and outlet were spaced to accommodate Nanoport fittings (Upchurch Scientific, Oak Harbor, WA). The multiple imaging chambers enable two experiments to be performed simultaneously. Fig. 2b shows the initial section of the cell trapping regions in both channels. The inlet channels deliver cells into a set of 50-150 triangular traps. In this design, the trap inlet is initially 150 μm at the top and over the 110 μm trap length, the trap width narrows down to a point constriction of 3-5 μm at the bottom to prevent cells from passing through the trap. The long trap length provides a degree of fluidic isolation for each trap, meaning that some portion of fluid streamlines that enter one trap exit through the trap constriction and are not carried to another trap. This is an important feature for investigating primary vs. secondary signaling and will be discussed in more detail in the following flow simulation section. Traps in the device are arranged in parallel between the inlet and outlet, and under pressure from the inlets, cells are forced into the trap constrictions. Fig. 2c shows a scanning electron micrograph of an alternative trap design with hemispherical structures to hold single cells. As opposed to the point constriction in the triangular traps, this trap design has a constriction length of 5 μm that will reduce the probability of cells extruding through the trap into the outlet channel. This trap design will also reduce the number of extraneous cells not held in traps due to the minimized length of the trap inlet. However, streamlines will flow easily from one trap to the next, thus compromising the fluidic isolation between traps. The total volume of a single imaging chamber is ~40 nL for a 52

trap device, thus enabling rapid exchange of medium within the device during experiments.

Device fabrication

SCA chips were fabricated using standard microfabrication techniques, starting with 6 inch 450 μm thick double polished silicon wafers. A 30 micron deep front-side silicon etch was performed to define the device channels and trap structures. A through-wafer backside etch was performed to define the device inlets and outlet. After processing, wafers were then treated with an O_2 plasma to remove resist and sonicated in acetone. Wafers were then sawed into individual die in preparation for anodic bonding. No. 1.5 pyrex coverslips (Esco Products) were then bonded to silicon chips using a custom-made anodic bonder system (15 minutes, 350 C, 8 N of pressure, 1.2 kV). After bonding, commercial microfluidic nanoport fittings were adhered to the chip inlets and outlet. SCA chips were imaged with an IX70 Olympus microscope using fluorescein, DAPI, and rhodamine filters, and images were taken with an Olympus DP70 CCD camera. Cells with dim GFP signals in the cytoplasm and strong PI signals in the nucleus were excluded from analysis. Images were analyzed with custom scripts in Matlab.

Results and discussion

Flow simulations in the SCA

To analyze cell delivery and fluidic isolation of cells, simulations of the fluid flow in the SCA chip were performed with commercial code from Computational Fluid Dynamics Research Corporation (CFD ACE 2007.2.23). Simulations were performed in two dimensions with a mesh density of 5-10 μm between nodes near the outer walls of the inlet and outlet channels, and ~1.5 μm between nodes within the trap regions. Conditions were set to room temperature with inlet flowrates set to 20uL/min, 1uL/min, 250nL/min, and 10nL/min. Outlets were set to atmospheric pressure, and device designs with hemispherical and triangular trap designs were both simulated.

Pressure and fluid flow in cell traps

Fig. 3a shows a simulation of a 52 trap device with a set flowrate of 10 nl/min. The fluid velocity magnitude, |v|, is shown for traps 1, 26, and 52. Fig. 3b shows the velocity and pressure profiles down the center of these three traps starting at the trap inlet (y = 0) and proceeding to the trap constriction (y = 110 μm). Due to the large number of traps, the pressure gradient across each individual trap is small (< 6 mPa). Traps near the beginning of the device have substantial flow near the trap inlet, with flow dropping off in the center of the trap inlet until it increases again near the constriction. Traps in the middle of the device have flowrates that drop slowly as the constriction is approached. The last traps have low velocities at the beginning of the trap inlet which steadily increase as the trap constriction is approached. The differences in the flow and pressure profiles will lead to variations in cell trapping depending on the location within the

device. Cells delivered to traps within the center of the device will have an increased probability of settling at the constrictions due to the lower flow velocities, whereas cells in traps at either ends of the device will have a greater probability of extruding through the constrictions to the chip outlet. This general trend has been confirmed in cell trapping experiments.

Fluidic isolation in cell traps

Streamlines were traced in the device simulations to assess flow between traps for fluidic isolation. Fig. 4a-b shows a simulation of fluid streamlines in the device in trap 1 and 26 with the flowrate set to 10 nl/min. The trap depth, D, is the length of the triangular obstruction from the channel inlet to the trap constriction. Each trap has a depth of isolation, D_i, defined as the distance between the trap constriction and a primary flow split that is closest to the constriction. For cells located above D_i in the traps, secretions from an activated cell will be carried to the rest of the traps in the chip. The distribution of the secretion throughout the rest of the chip will be determined by diffusion between streamlines. However, for a cell located below D_i in the traps, fluid will flow past the cell, carrying secretions to the chip outlet and preventing them from reaching other traps in the device. This fluidic isolation scheme requires the Peclet number in the system, $Pe = Lv/D$ (where L is the length scale in the system, v is the flow velocity, and D is the diffusion constant of the secretion) to be >> 1, meaning that convective flow dominates the diffusion of the secretions. Secretions such as cytokines have a molecular weight between ~5-50 kDa, with estimated diffusion constants on the order of 10^{-10} – 10^{-11} m^2/s

[23]. Thus with L ~ v ~ 10^{-5}, the Peclet number is ~ 1-10. A Pe >> 1 can be ensured by increasing the flowrate through the device after cells have attached to the device.

Another consideration is that the presence of the cell in the device must not disrupt flow substantially. Cells adhered to one surface of the device will minimally impact the flow streamlines, while cells attached to both sidewalls in trap constrictions may disrupt flow more substantially. However, given the diameter of the cells (~10 μm) and the height of the trap constriction (30 μm), we still expect the flow to be minimally impacted by cells trapped in the constrictions.

Fig. 4a shows that trap 1 has a primary flow split near the center of D, with flow above D_i returning back to the inlet channel and on to the next trap, and flow below D_i exiting through the trap constriction. For trap 26 (Fig. 4b), D_i is much closer to the trap constriction. A secondary flow split (red arrow) that is closer to the inlet channel is noted in trap 26 with an associated eddy current on the other side of the trap channel. This secondary flow split emerges in trap 14 and then disappears after trap 36. Since our objective is to prevent the diffusion of cell secretions into streamlines that leave the trap and flow to other traps, the true isolation depth remains located at the primary split nearest the trap constriction.

A plot of the fraction D_i/D is shown for each trap in Fig. 4c. A minimum D_i of ~20 μm occurs in the center of the device, with larger D_i in the beginning and end of the device. The dashed line in Fig. 4c indicates the position of the secondary flow splits that exist only in traps 14-36. Experimental assessment of the flow in the SCA was performed by injecting fluorescently labeled *E. coli* bacteria into the device after RAW cells were trapped. Estimates for D_i were made by examining the lowest depth reached in four traps

(#1, 2, 26, and 51) by bacteria that were then carried back up out of the trap and on to the next trap. The lowest depth reached by six bacteria in each of the four traps was averaged to estimate D_i. Experimentally observed D_i agreed well with flow simulations at the beginning of the device, even with RAW cells captured in some of the trap constrictions. The experimental estimate for D_i/D at trap #26 more closely matches the secondary flow split position, while the largest deviation between the simulation and experimental assessment occurred with trap #51. This trend of an increasing divergence between the simulated and actual flow could be due to the cumulative effect of having trap constrictions partially blocked by trapped RAW cells.

Live cell imaging during pathogen challenges

Host cell capture in the SCA

Cell trapping experiments in the single cell array chips were performed with RAW cells containing the GFP-RelA construct in order to visualize the translocation of RelA from the cytoplasm to the nucleus following immune stimulation. Devices were connected to 1/32 PEEK tubing and placed on an inverted fluorescence microscope for live imaging. Chips were heated using a custom-made heating stage and a temperature controller (Warner Instruments). Syringes were connected and fluid was delivered to the chip using a syringe pump (Harvard Apparatus). SCA devices were first purged with endotoxin-free water, followed by degassed cell growth media to passivate the chip surfaces. Immediately prior to injection into the SCA, the cell suspension was passed

through a 40μm nylon mesh filter and loaded into a 3ml syringe containing two 3mm glass beads. The syringe was kept rocking at room temperature during infusion at 10-1000 nl/min until a sufficient number of cells was captured in the imaging chamber. After the capture procedure is complete, cells are incubated with a constant flow of growth media for 30 minutes to ensure RelA translocation does not occur absent the pathogen challenge. Fluorescence images of the GFP-RelA signal and the nuclear signal were taken to verify that the GFP-RelA is primarily located in the cytoplasm prior to stimulation. RelA activation can occur due to LPS environmental contamination, and has also been shown to occur due to shear stress in a fluidic environment [24]. None of the experimental data documented here contained translocated cells prior to pathogen challenge. After cell capture, the PI signal was also monitored to differentiate between living and dead cells. Background fluorescence from the cell growth media was used as a real-time indicator of continuous fluid flow in the device in that portions of the chip where flow was obstructed had dimmed background fluorescence due to photobleaching.

Figure 5a shows the fluorescence images of the GFP-RelA and nucleus signals in a single RAW cell captured in a triangular trap constriction. Lineplots of the signal intensities in Fig. 5b show that the peaks for the GFP-RelA signal and the nucleus are anti-coincident, indicating that the GFP-RelA is located primarily in the cytoplasm. The minimal PI signal, and specifically the lack of a PI-rich nucleus, indicates that this particular cell is alive.

We examined the ability to capture single cells in traps using both the triangular and hemispherical trap designs. The hemispherical trap design was used in five separate experiments, and the triangular trap design was used in four separate experiments. A total

of 300 cells (hemispherical devices) and 318 cells (triangular devices) were examined. In this data-set, a total of 150 traps were examined in the pooled data for the hemispherical design experiments, and 75 traps were examined in the triangular design experiments. Figure 5c shows the fraction of cells that are single cells in traps (s), multiple cells in traps (m), and cells located in the inlet channel of the imaging chamber (i). Nearly 30% of all cells in the hemispherical devices were single cells in traps, while only ~11% of cells in the triangular devices were single cells in traps. The hemispherical design also yields more cell aggregates in traps and less cells adhered to the inlet channel of the imaging chamber. The triangular design had a smaller percentage of aggregates in traps, but a much larger percentage of cells in the inlet channel. Currently, modified trap designs are being developed to optimize single cell capture and minimize cell attachment in the upstream inlet channel while maintaining fluidic isolation of trapped cells.

GFP-RelA translocation after LPS challenge

For LPS challenge experiments, cells are trapped in the SCA and then incubated with normal growth media for 30 minutes prior to LPS introduction. LPS in gas- and temperature-equilibrated growth media is then injected. Fluidic connections are broken at the upchurch fittings in order to minimize the transit time of LPS to the cell imaging chambers. Images of the RelA signal in trapped cells were taken rapidly in sequence throughout the entire device, with repeated imaging every 5 minutes. Fig. 6 shows an experiment in which a single isolated RAW cell is located in the last trap of an SCA device. The image in Fig. 6a was taken immediately after the 30 minute pre-incubation

period, with a close-up image shown in Fig. 6b. Twelve minutes later, 1 μM *E. coli* LPS was injected into the device at a flowrate of 20 nl/min. Approximately seven minutes after the LPS was injected, the RelA begins to translocate into the nucleus (Fig. 6c). This stage in the translocation process is characterized by a bright GFP-RelA signal throughout the entire cell with no distinct nucleus. Within a minute, translocation of RelA into the nucleus is complete as characterized by the annular shape of the GFP-RelA signal in the nucleus (Fig. 6d). Figure 6e shows intensity lineplots of the GFP-RelA signal at the time-points shown in Fig. 6b-d. The mean ratio of GFP fluorescence in the nucleus and cytoplasm is shown in Fig. 6f as a function of time. The fluorescence was averaged over 20 locations in the nucleus and cytoplasm at each time-point. This particular cell was monitored over the course of a total of two hours, and the GFP-RelA location and distribution within the cell remained stable after the initial translocation event ~20 minutes into the experiment. The mean translocation time of single cells in traps (n = 4) and multiple cells in traps (2 or 3 cells, n = 11) was 13.3 ± 3.9 and 14.9 ± 2.2 min, respectively. ANOVA analysis shows the two means are not significantly different (p value = 0.3).

GFP-RelA translocation after live bacteria challenge

A purified LPS challenge simplifies the analysis of early immune response since LPS-induced stimulation is initially confined to the TLR4 signaling network [25]. Challenges with live bacteria are more difficult to analyze due to the fact that multiple intersecting cell signaling pathways can be stimulated [26, 27]. However, we are

interested in comparing the immune response produced by purified LPS and live bacteria, specifically in regard to GFP-RelA translocation. Figure 7 follows the infection of a single RAW cell in a live *E. coli* bacteria challenge experiment. RAW cells were initially captured and held for 30 minutes in a hemispherical trap device before bacteria suspended in media were flowed into the device. Within a few minutes after injection, bacteria could be visualized interacting and becoming immobilized adjacent to captured RAW cells. The bacteria were delivered continuously to the cells over the course of the next two hours. The peaks in the nucleus and GFP-RelA signals (inset) in the captured cell in Fig. 7b are offset, indicating that the GFP-RelA is initially located in the cytoplasm. Over the next 20 minutes, the GFP-RelA signal becomes flat as the RelA begins moving into the nucleus (Fig. 7c). At 37 minutes after the injection of bacteria, the peaks of the nucleus and GFP-RelA signals are now coincident indicating GFP-RelA translocation is complete (Fig. 7d). The histogram in Fig. 7e shows the number of translocated cells (N_t) out of a total of N_0 cells as a function of time. This data is pooled from two separate *E. coli* challenge experiments with the same experimental conditions. In this experiment, approximately 40% of the total number of RAW cells (N_0 = 59) underwent GFP-RelA translocation during the two hour duration of the experiment. The mean time of translocation for the live *E. coli* challenge experiments was 23.2 ± 9.4 min. The large spread in translocation times for the bacterial challenge is partly due to the uneven distribution of *E. coli* bacteria in the device, resulting in some cells interacting with multiple *E. coli* bacteria and some interacting with none. Also, some RAW cells were observed to contain fragments of red fluorescence, indicating that bacteria were being phagocytosed and digested within the first 20 minutes of the experiment. A last

consideration in these experiments is the fact that *E. coli* bacteria release LPS into the suspending medium, an explanation for the fact that some RAW cells with no *E. coli* bacteria in direct proximity were observed to undergo GFP-RelA translocation.

Conclusions

We have demonstrated the first on-chip infection of multiple single host cells with live imaging of early immune response signaling events. Previous reports [19-21] have infected populations of host cells in microfluidic chambers, a condition that obscures the role played by cell-cell interactions on the initiation and progression of immune response. In our device, cells are not perturbed by the single cell isolation procedure, and are subsequently monitored over the course of several hours after challenge with pathogenic stimulants. The metric of cell activation used here was the translocation of GFP-RelA from the cytoplasm to the nucleus upon stimulation with LPS and live bacteria. The average translocation time for cells stimulated with 1 μM of purified LPS was 14.5 ± 2.7 minutes, while the average translocation time for live *E. coli* bacteria challenges was later and with a much larger distribution (23.2 ± 9.4 min). This is may be due to the difference in concentration of the challenge in the device: at 1 μM, there are ~10^{10} LPS molecules in a 40 nL imaging chamber, whereas the concentration of bacteria observed in the device was substantially less (~10^6). Higher pathogen concentrations in the device lead to faster interactions with host cells and thus faster immune response kinetics. The difference in spread of the responses is likely due to clumping and adhesion of bacteria to the device, which led to broad distributions of bacteria interacting with different host cells. A second

consideration for the experimental results is in regard to the kinetics of immune response in single cells isolated in traps compared to multiple cells in close proximity within a trap. For the purified LPS experiments, the translocation time was invariant with regard to the number of host cells held within a trapping structure. This was an expected result due to the fact that it takes several hours (~4 hours) for cytokines to be produced and secreted from activated cells, thus cell-cell interactions through secreted cytokines are not expected to impact short-term primary immune responses. Future work will include longer challenge times to investigate this phenomenon. In addition, variations in pathogen concentration and source (e.g. *Y. pestis* and *F. tularensis*) will be investigated.

Acknowledgements:

We would like to thank the Microelectronics Development Laboratory staff and management at Sandia National Laboratories for device fabrication. We also extend our gratitude to Jaime McClain and John Anderson for device fabrication. This work was performed as part of the Microscale Immune Studies Laboratory project funded by Sandia's Laboratory Directed Research and Development program. Sandia is a multiprogram laboratory operated by Sandia Corporation, a Lockheed Martin Company, for the United States Department of Energy under contract DE-AC04-94AL85000.

References:

1. S. Akira, K. Takeda and T. Kaisho, *Nature Immunology*, 2001, **2**, 675-680.

2. B.A. Butcher and E.Y. Denkers, *Infection and Immunity*, 2002, **70**, 5216-5224.

3. H. H. McAdams and A. Arkin, *PNAS*, 1997, **94**, 814-819.

4. P.S. Swain, M.B. Elowitz and E. D. Siggia, *PNAS*, 2002, **99**, 20, 12795-12800.

5. W.J. Blake, M. Kaern, C.R. Cantor and J.J. Collins, Nature, 2003, **422**, 6932, 633-637.

6. J.M. Irish, R. Hovland, P.O. Krutzik, O.D. Perez, O. Bruserud, B.T. Gjertsen and G.P. Nolan, *Cell*, 2004, **118**, 2, 217-228.

7. D. Longo and J. Hasty, *Mol. Syst. Biol.*, 2006, **2**, 1-10.

8. M.E. Lidstrom and D.R. Meldrum, *Nat. Rev. Microbiol.*, 2003, 1, 158-164.

9. D. Di Carlo and L.P. Lee, *Anal. Chem.*, 2006, **78**, 7918-7925.

10. B. Huang, H. Wu, D. Bhaya, A. Grossman, S. Granier, B. K. Kobilka and R. N. Zare, *Science*, 2007, **315**, 81-84.

11. Y. Marcy, T. Oshoey, R.S. Lasken, T.B. Stockwell, B.P. Walenz, A.L. Halpern, K.Y. Beeson, S.M.D. Goldberg, S.R. Quake, *PLoS Genet*, 2007, **3**, 9, e155.

12. P. Paszek, T. Lipniacki, A. R. Brasier, B. Tian, D.E. Nowak and M. Kimmel, *J. Theoretical Biology*, 2005, **233**, 3, 423-433.

13. T. Lipniacki, P. Paszek, A.R. Brasier, B.A. Luxon and M. Kimmel, *Biophysical Journal* 2006, **90**, 725-742.

14. A. Han and A.B. Frazier, Lab Chip 2006, **6**, 1412-1414.

15. C.D. James, N. Reuel, E.S. Lee, R.V. Davalos, S.S. Mani, A. Carroll-Portillo, R. Rebeil, A. Martino and C.A. Apblett, *Biosensors and Bioelectronics*, 2008, **23**, 845-851.

16. C. Amatore, S. Arbault, Y. Chen, C. Crozatier and I. Tapsoba, *Lab Chip*, 2007, **7**, 233-238.

17. A. Tourovskaia, X. Figueroa-Masot and A. Folch, *Lab Chip*, 2005, **4**, 14-19.

18. K.J. Wieder, K.R. King, D. Thompson, C. Zia, M.L. Yarmush and A. Jayaraman, *Biomed. Microdevices*, 2005, **7**, 213-222.

19. M. Antia, T. Herricks and P.K. Rathod, *PLoS Pathogens*, 2007, **3**, 0939-0948.

20. C. Wei, J. Cheng and T. Young, *Biomedical Microdevices*, 2006, **8**, 65-71.

21. D.M. Thompson, K.R. King, K.J. Wieder, M. Toner, M.L. Yarmush and A. Jayaraman, *Anal. Chem.*, 2004, **76**, 4098-4103.

22. W.W. Quitschke, Z. Lin, L. DePonti-Zilli and B.M. Paterson, *The Journal of Biological Chemistry*, 1989, **264**, 9539-9546.

23. M.E. Young, P.A. Carroad, and R.L. Bell, *Biotechnol. Bioeng.*, 1980, **22**, 947– 955.

24. Q. Lan, K.O. Mercurius and P.F.Davies, *Biochemical and Biophysical Research Communications*, 1994, **201**, 950-956.

25. S. Akira, *The Journal of Biological Chemistry*, 2003, **278**, 38105-38108.

26. K.J. Moore, L.P. Anderson, R.R. Ingalls, B.G. Monks, R. Li, M.A. Arnaout, D.T. Golenbock and M.W. Freeman, *J Immunology*, 2000, **165**, 4272-4280.

27. F. Wu, N. Vij, L. Roberts, S. Lopex-Briones, S. Joyce and S. Chakravarti, *J. Biol. Chem.*, 2007, **282**, 26409-26417.

Figures

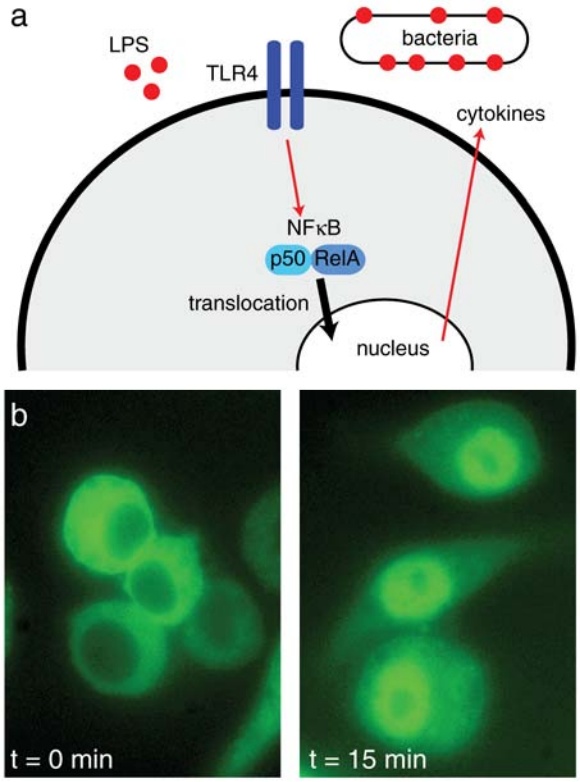

Figure 1: (a) The TLR4 signaling pathway is initiated by soluble LPS and Gram-negative bacteria. After a series of signaling events, the transcription factor NFκB translocates from the cytoplasm to the nucleus, where it initiates cytokine production and release from the host cell. (b) RAW264.7 cells grown on a coverslip at t = 0 min and 15 min after pathogen challenge with *E. coli LPS* (1 μM).

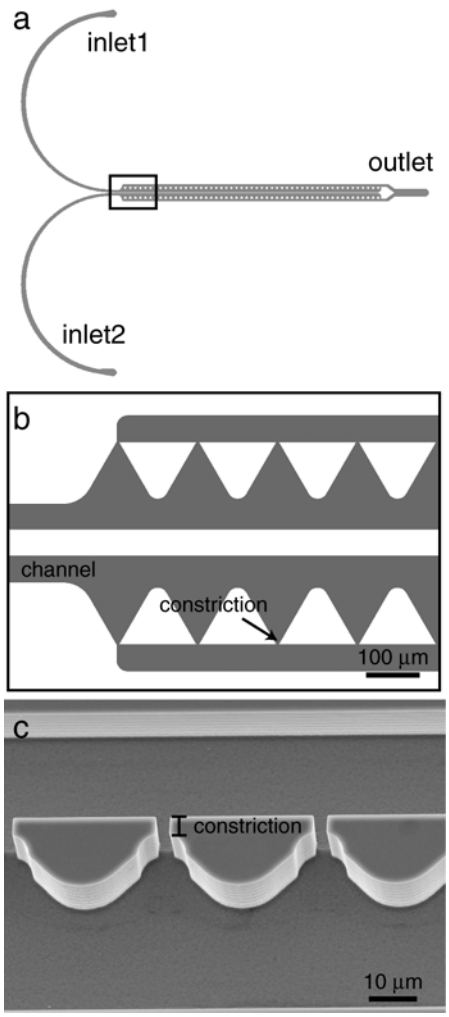

Figure 2: (a) Single cell array (SCA) microfluidic chip design. (b) Close-up of the boxed region in (a), highlighting the imaging chamber inlet channel and triangular point constrictions for capturing cells. (c) SEM image of an alternative hemispherical cell trap design with 5 μm long trap constrictions.

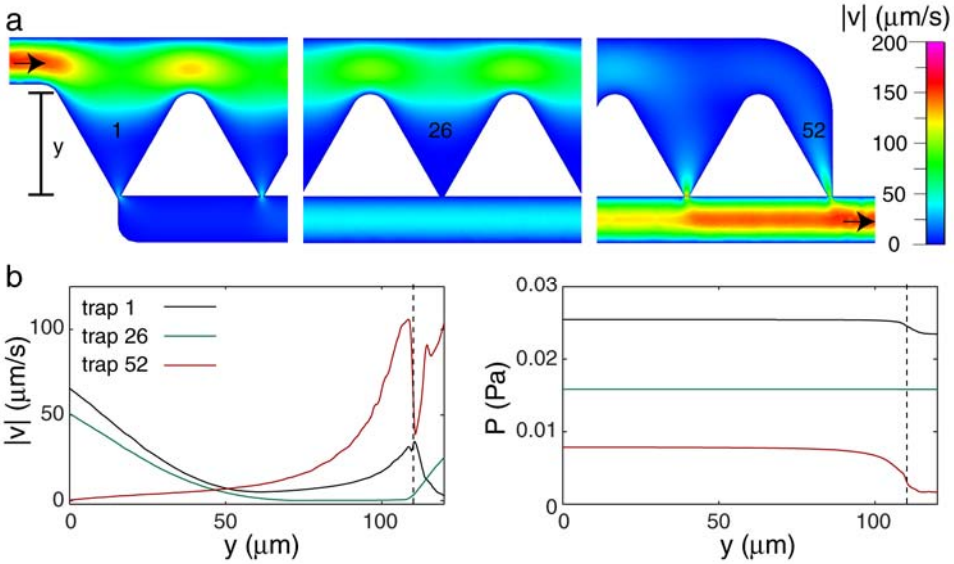

Figure 3: (a) Simulation of the velocity magnitude (|v|) in the SCA device at trap numbers 1, 26, and 52 (flowrate=10 nl/min). (b) Velocity magnitude and pressure across the three traps along the y axis. The location of the trap constriction is noted (dashed line).

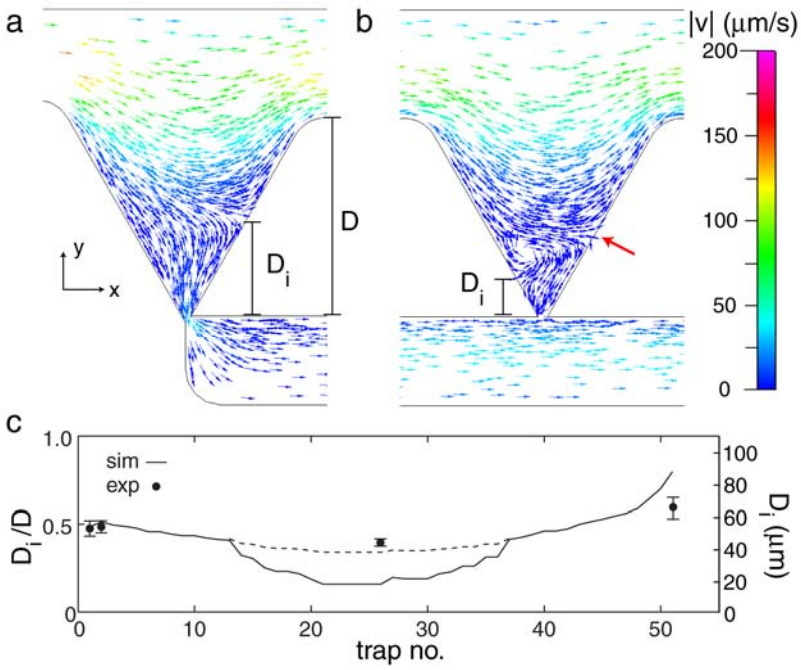

Figure 4: Flow streamlines (10 nL/min) in the device at (a) trap 1 and (b) trap 26. The trap depth (D) and the depth of isolation (D_i) are noted. In (b), a secondary flow split further upstream in the trap is noted (red arrow). (c) The simulated (sim) and experimentally estimated (exp) isolation depth in μm and as a fraction of the total trap depth for each trap. The secondary flow split points are denoted by the dashed line.

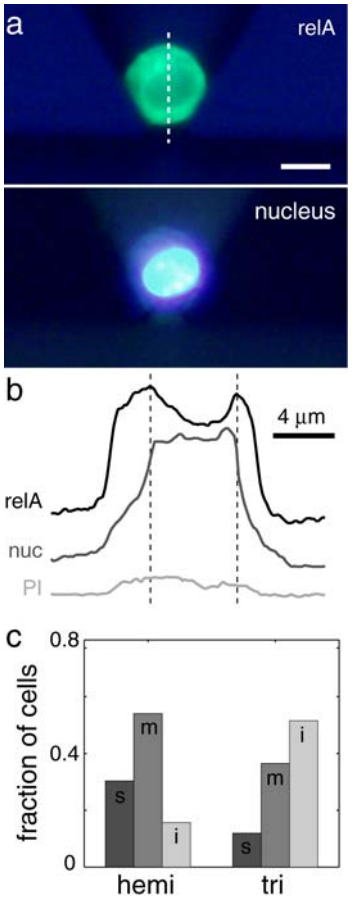

Figure 5: Single RAW cell captured in a triangular cell trap showing the GFP-RelA and nucleus signals. Scale bar = 5 µm. (b) Intensity lineplots at the position shown in (a) for the three signals. The location of the nucleus is noted (dashed lines). (c) Fractional distribution of live cells in the hemispherical (hemi) and triangular (tri) trap devices grouped by: single cells in traps (s), multiple cells in traps (m), and cells in the imaging chamber inlet channel (i).

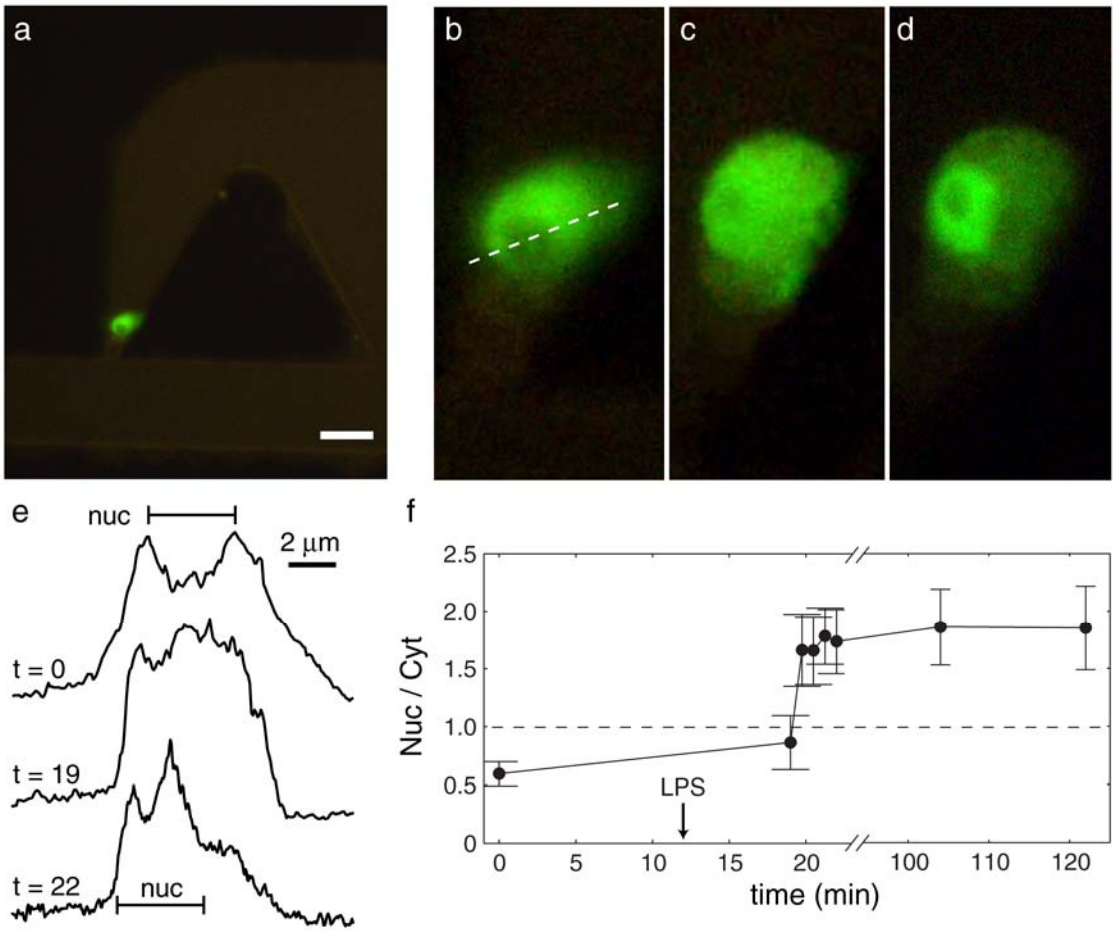

Figure 6: GFP-RelA translocation in a trapped RAW cell at t = 0 (a, zoom in b), 19 (c), and 22 min (d). Scale bar = 30 µm. (d) Lineplots (dashed line in b) of the GFP intensity over time, highlighting the location of the nucleus (nuc). (e) Ratio of the GFP fluorescence in the nucleus and cytoplasm (mean and standard deviation) as a function of time before and after the addition of LPS (*E. coli* 1 µM) at t = 12 min.

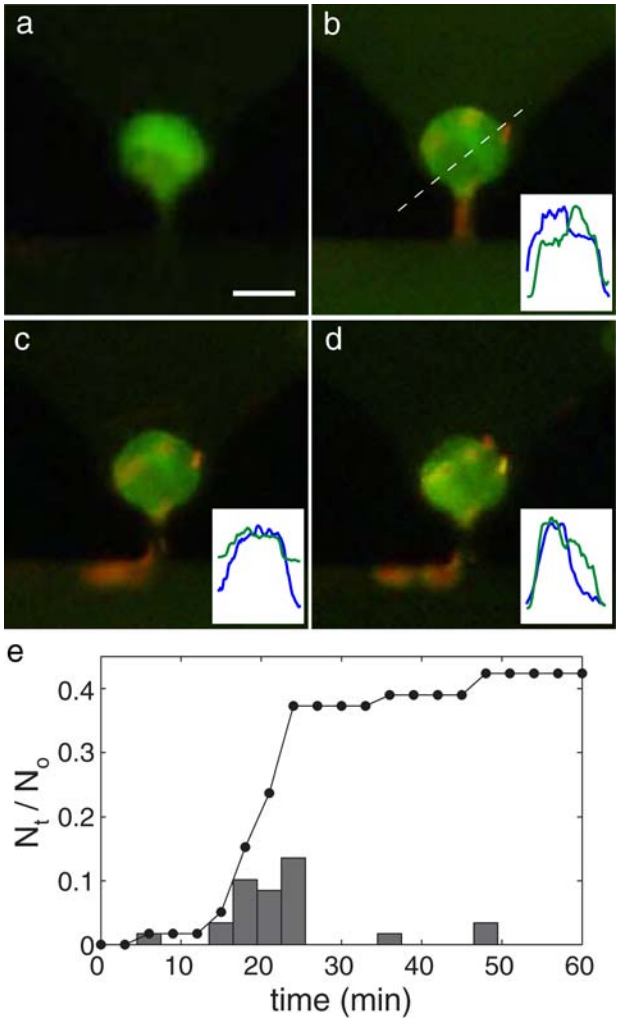

Figure 7: GFP-RelA translocation in a trapped RAW cell at t = 0 (a), 7 min (b), 25 min (c), and 37 min (d). Lineplots (dashed line) of the GFP-RelA (green) and nucleus (blue) intensities are shown in the insets. Scale bar = 10 μm. (e) Discrete (bars) and cumulative (points) fractional number of translocated RAW cells (N_t) after a pathogen challenge with live *E. coli* bacteria as a function of time.

3. Microfluidically-unified cell challenge, preparation and flow cytometry allows automated phosphoprofiling of macrophage response to lipopolysaccharide

Nimisha Srivastava, J. S. Brennan, R. F. Renzi, M. Wu, S. S. Branda, Anup K. Singh and Amy E. Herr

Monitoring of intracellular signaling events is crucial to understanding innate immune defense against invading pathogens. Flow cytometry, microscopy and western blot assays are powerful tools for signaling studies. Nevertheless, each approach is currently standalone and limited by numerous time-consuming, labor-intensive steps. We report a novel assay system that integrates fully-automated single-cell manipulation, microscopy and subsequent flow cytometric analysis. Our phospho Flow Chip (pFC) relies on monolithic microfluidic technology to rapidly conduct phosphoproteomics studies from initial chemical challenge through all preparatory steps and ensuing temporally-and spatially-resolved analyses. While readily adaptable, we employ pFC to monitor phosphorylation of MAP kinase, ERK1/2, in response to E.coli lipopolysaccharide (LPS) stimulation. The pFC tool permits ERK phosphorylation monitoring starting as early as 5min after LPS stimulation with the added advantage of reduced cell aggregation and cell loss. The integrated pFC tool yields complementary imaging and flow cytometry data sets quickly and autonomously.

To elucidate the role of cells in the immune system, new tools to characterize signaling epitopes engaged in early intracellular response are emerging. Until the recent advent of fluorescent reagents for phospho-epitope staining, most assays offered limited, static snapshots of inherently rapid and transitory cellular signaling events1, 2. The ability to

measure fleeting phosphorylation of specific protein epitopes in kinase signaling cascades sheds light on cell activation and dynamic response to extracellular stimuli. Phospho-epitope analysis implemented with flow cytometry supplies single cell-level information required to tease apart stochastic variation among large cell populations[3, 4]. Nevertheless, the multiple sample preparation, handling, and analysis steps required for phospho-profiling using conventional bench-top technology are labor intensive, inefficient, and require large, expensive instrumentation. Recent strides in instrumentation and high-throughput sample preparation strategies (i.e., 96 well plates, liquid autosamplers) have yielded important intracellular phosphorylation data for large sample sets[5]. New, automated technology capable of monitoring phosphorylation levels of key signaling proteins with fine temporal resolution would further increase the data available.

Fine temporal information regarding various intracellular signaling events can be difficult to obtain using bench top handling methods (i.e., petri dishes, centrifuge tubes). Species such as short lived nuclear phosphoproteins (e.g., c-myc protein), rapidly changing cytoplasmic Ca^{2+} levels, aggregation of surface receptors, protein phosphorylation and subsecond protein oscillations in platelets are particularly hard to monitor[6, 7]. To bridge the gap, new cytometry modalities are emerging[8]. Flow cytometry that relies on sample handling via high speed valves facilitates kinetic measurements with a resolution of 300 ms[9]. Extending such fine temporal resolution methodologies to phosphoprofiling combined with completely hands-free operation of multiple preparatory steps (i.e. stimulation, fixation, permeabilization, antibody staining, washing) would allow correlation and synchronization between distinct, yet complementary cellular events.

Such a tool would provide an opportunity to quantify the concentration, location, and dynamic processes associated with intracellular and, perhaps, intercellular signaling.

Use of microfluidic technologies offers compelling advantages to sample preparation, automation and integrated analyses. Microfluidic tools have been demonstrated at the proof-of-concept level for not only flow

1 Currently at Department of Bioengineering, University of California, Berkeley CA 94720

cytometry[10-13] and fluorescence-activated cell sorting[14, 15] but also for functionality such as cell culture[16-19] , surface patterning[20], rapid stimulation[21] , and single cell arrays[22, 23] . Beyond unit analyses, we seek to exploit ready integration of microfluidic components to form the basis for a coherent tool optimized to monitor single-cell intracellular signaling. Of particular relevance to phosphoprofiling, integration of numerous upstream preparatory processes with flow cytometric detection on a monolithic platform would allow programmable control of time point selection, both for dosing of challenge and measurement of response. Minimal consumption of reagents, especially costly antibody stains, is advantageous for monitoring numerous time points in a large experimental design space[24, 25] . While microfluidic methods have yet to prove competitive with the throughput of commercial flow cytometers, reductions in the overall time and manual intervention required for single-cell signaling studies could make integrated microfluidic preparation appealing. Additionally, with microfluidically-enabled reduction in cell aggregation and losses provides the capability to perform flow cytometry on small cell populations, such as primary cells and hematopoietic stem cells.

To construct a cellular level understanding of the innate immune response, an ensemble of responses – measured at the level of individual cells – to exogenous signal is required 26. The endotoxin, lipopolysaccharide (LPS), a major component of Gram-negative pathogenic bacteria (e.g., Yersenia pestis and Francisella tularensis) induces activation of mammalian macrophages through the evolutionary conserved trans-membrane surface protein, Toll-like receptor (TLR4) and its co-receptors, MD-2 and CD-1427, 28 . Upon activation, TLR4 associated with a key adaptor protein, MyD88 (myeloid differentiation factor 88) mediates a pathway which proceeds through a synchronization of molecular events that encompass, among other effects, the phosphorylation of protein kinase ERK, activation of NFκB and eventually, the activation of key transcription factors such as c-Fos, Elk-1 and c-Jun29, 30. This cascade induces the expression of immune activation genes that steer the course for immediate defense against pathogen replication – either directly by phagocytosis or summoning other cells to the site of the infection. The molecular events associated with innate immune response are categorized as "first responders" and typically occur in the first few seconds to minutes30 and therefore, necessitate fine temporal and spatial resolution.

Here we report on the pFC assay system as a means to incorporate and automate all steps necessary for phospho-profiling of adherent cell populations activated through the TLR4 signaling pathway. Pressure-driven fluid flow in quartz microfluidic devices is programmed to automate process steps including: pathogen challenge to host cells (including dosing, rapid mixing, and timed incubations), all phospho-profiling preparatory steps (including cell fixation, plasma membrane permeabilization, fluorescent immuno-staining and numerous intermediate washing steps), and subsequent flow

cytometry. The pFC platform is designed to be compatible with fluorescence microscopy, thus enabling real-time observation of cell phenotype prior to flow cytometry. We demonstrate utility of the pFC assay by monitoring the intracellular phosphorylation of the mitogen¬activated protein (MAP) kinase extracellular signal-regulated kinase (ERK1/2) in response to macrophage stimulation by an endotoxin found on the outer membrane of Gram-negative bacteria.

RESULTS The pFC assay platform

The pFC technique exploits microfluidic technology to combine upstream cell preparation of select cell populations with subsequent flow cytometry (Fig. 1). Nominal user intervention is necessary as programmable flow controllers and valves are implemented to automate the multiple steps required for phosphoprofiling 31 . The core of the pFC technique is a planar quartz microfluidic device mated with an epi-fluorescence microscope and single-point fluorescent detection. The pFC device was optimized for the analysis of adherent cells and relies on continuous pressure driven flow and stopped flow intervals for reagent delivery and incubation.

To initiate the phosphoprofiling assay, a suspension of macrophage cells is pressure-delivered onto the chip from reservoirs containing a cell suspension in culture media (Supplemental movie S1). After the pFC device is seeded with cells, flow is stopped. Having a higher density than the culture media, the macrophage cells settle to the bottom of the spiral incubation chambers (Fig. 1). Settled cells adhere to the bottom surface of the channel within 5 min (data not shown). To chemically challenge the cells, pressure-driven flow is again applied to drive a desired concentration of stimulant into the

incubation chamber. The challenge duration is controlled by an interval of stopped flow. After challenge, flow of a chemical fixative is initiated to immediately wash the stimuli out of the incubation chamber. Fine temporal resolution in the subsequent phosphorylation assays depends on the rapid fluid exchange capability. Rapid fluid exchanges are also useful for efficient preparatory processes.

For phosphoprofiling, an intracellular antibody staining protocol was adapted from conventional flow cytometry31 . As compared to benchtop phosphoprofiling, the pFC method automates all cell handling – from stimulation to flow cytometry – in the monolithic pFC device. As mentioned and will be described in detail, the phosphostaining protocol requires multiple fluidic handling steps for: chemical fixation, permeabilization, antibody staining, and several washing steps. After staining, cell phenotypes are investigated using epi¬fluorescence and bright-field microscopy (Fig. 1) of the pFC incubation chambers. Subsequent flow cytometry is conducted after releasing cells from the microchannel surface using a combination of high shear rates and simultaneous enzyme-assisted digestion (Supplemental movie S2).

pFC microdevice design and automated operation

The pFC channel network consists of two wide spirals (w = 230 µm, d = 35 µm, L = 50 mm, V = 350 nL) that function as incubation chambers. The volume of each incubation chamber was chosen so as provide enough cell holding capacity for statistically relevant single cell assays. The pFC device holds ~2000 cells per chamber per assay. The incubation chambers were fluidically isolated through use of high resistance (much narrower channel width) spiral features. The incubation chambers were designed as

spirals to minimize stagnate volumes, dead volume, and cross-contamination. The curvature inherent to spiral geometries allowed smooth flow and lossless loading of cell suspensions.

To seed macrophage cells into the incubation chamber, visual inspection is used to determine when cells have traversed the channel network and reached the two incubation chambers. At that point, the flow is halted. As described, the macrophage cells settle to the bottom of the channel. The macrophage cell settling time is estimated to be 25 ms by approximating the settling velocity (v) for cells in a dilute suspension using $v = (2/9)r2(\Delta\rho)g/\mu$ where $\Delta\rho$ is the deviation of the density of macrophages from that of the media, μ is the viscosity of the media, r is average size of a macrophage (10 µm) and g is the gravitational force. Density gradient centrifugation yields a ρ of 1.05 g/mL for macrophage cells. For the media, ρ is1.01 g/mL. The viscosity, μ, of the cell suspension was approximated to that of media owing to the low volume fraction ($ø < 0.01$) using the Einstein relationship $\mu suspension = \mu solvent /[1+2.5ø]$. Within 5 min, macrophage cells were observed to have attached to the channel bottom. Through in situ shear flow assays conducted in the incubation chambers, we measured an adhesion force greater than 1.7 nN per cell (Fig. 2a).

The pFC method automates the sequential introduction of the multiple reagents required for infection and the phospho-flow protocol. Dual spiral incubation chambers (Fig. 1, spirals 1 and 2) allow a control experiment to be executed concurrently with a challenge assay. The low volume of the incubation chamber (V = 350 nL) and the accessible volumetric flow rates (Q =5 µL/min) enabled rapid fluid exchange (t = V/Q = 4 s) for stimulation with high temporal resolution (Fig. 2c). Shear stress (100 dyne/cm2) resulting

from high volumetric flow rates (Q = 50 μL/min) neither detached macrophages from the glass surface nor were substantial enough to activate the cells (Fig. 2a, b). The shear stress exerted on the attached cells is comparable to shear experienced during routine pipeting of cells and reagents.

After predetermined stimulation at 37oC (see Supplemental Methods and Fig S2 for detailed operation of the pFC), cells in both incubation chambers were fixed, permeabilized, and stained. Fixation required 2 min, chemical permeabilization required 2 min, and conservative buffer exchange steps required 5 min each. Bright field and fluorescence imaging were conducted just prior to high shear rate and trypsin digestion release, while the cells were still attached to the channel surface. After imaging, phosphostained cells were again fixed with paraformaldehyde prior to trypsin treatment to prevent any damage to intracellular targets. On-chip flow cytometry proceeded by using hydrodynamically focused sheath flow (Fig. 1, bottom channel). Volumetric flow rates were controlled so as to achieve a 10:1 focusing of the sample flow enabling high throughput (100cells/min) flow cytometric detection. For validation and characterization purposes, released cells were also collected from the waste reservoir and analyzed via conventional flow cytometer (see Supplemental Methods).

Characterization of improved cell handing using pFC assay system

We conducted a series of experiments designed to characterize the handling cell loss and the tendency of the macrophage cells to aggregate during and after phosphostaining in the pFC device. While introduced in suspension, the pFC cell preparation protocol employs adhesion of macrophage cells to the glass floor of the incubation chambers. The

attachment of the cells to the chamber floor acts to localize the cells for stimulation, phospho-staining, and microscopy (Fig. 3). Microscopy-based inspection of macrophage-seeded incubation chambers prior to challenge introduction (Fig. 3a) to the same regions after challenge and all subsequent phosphostaining steps reveals negligible cell loss. We attribute the minimal cell losses to both the use of macrophage immobilization during the seeding step and the low dead volumes in the pFC fluid device. Further, after the trypsin release step we observe no retained macrophage cells on the glass surface. Compared to pFC preparation, benchtop phosphostaining protocols resulted in losses of up to ~15% cells during each centrifugation-based washing step. Hemocytometer counts revealed that bench-top preparation resulted in a total loss of up to 75% of cells, especially during the numerous washing steps required after permeabilization of cells.

To characterize the impact of pFC manipulation on generation of debris and large cell aggregates, we compared bench-top flow cytometry preparatory protocols with our pFC preparatory techniques. For minimally manipulated cells fresh from culture, usable single cells comprised 80 % of the total cell population (Fig. 3b). After analysis, the population was split and stimulated, immunostained, and analyzed. One population was manipulated using bulk bench-top preparation and the second population was handled using the pFC method (Fig. 3b). After conventional bench-top preparation, flow cytometry side scatter vs. forward scatter analysis revealed that 45+6 % of the cells obtained were single cells in suspension. In contrast, 70+9 % of the cells obtained by pFC preparation were present in a single cell suspension. Associated flow cytometry histogram data gated on the single cell distribution (R1) for each population shows that bench top preparation led to a fluorescence intensity coefficient of variation (CV) of 46 %. For cells prepared using the

pFC approach, the fluorescence intensity CV was 29 % (Fig. 3b). The fluorescence intensity CV arising from the pFC method closely resembles the population spread of the starting untreated sample (CV~32 %). The favorable coefficient of variation resulting from pFC preparation is attributed to reduced aggregation of activated adherent macrophages, uniform cell-to-cell immunostaining, and elimination of repeated centrifugation-based cell washing steps. Bright field images of the macrophage cells qualitatively reveal and confirm larger cell aggregates with the bench-top preparation, as compared to the on-chip preparation (Fig. 3c). The pFC instrument design enables multiplexed measurements of single cells, individually or as part of a population, under well-controlled, optimized conditions – something nearly impossible with current bench top preparatory technologies. Such an approach, with reduced cell aggregation and losses, will likely appeal to the single-cell analysis of small populations such as primary and stem cells.

pFC analysis of Toll Like Receptor-4 intracellular signaling

As a step towards understanding how the innate immune system responds to LPS and pathogens, we have developed and optimized assays for analyzing phosphorylation of ERK1/2, a key intracellular kinase protein in the MyD88 pathway of the macrophage TLR-4 response to Gram-negative pathogens. We chose to initiate work using the MyD88 pathway, as the most detailed understanding of signaling pathway engagement by TLRs has come from the study of MyD88, a universal adaptor protein32 . Approximately 5x106 cells/mL were introduced into the pFC device and localized to the incubation chambers, as described previously. Cells in the first chamber were stimulated

with 1 µM smooth E. coli LPS at 37oC. The second chamber was not challenged with LPS. At each post-stimulation time point of interest, macrophage cells in both chambers were fixed, permeabilized, immuno-stained, enzymatically released, hydrodynamically focused and analyzed using flow cytometry – all on the same pFC platform with minimal user intervention. Flow cytometry histograms show significant increases in the level of phosphorylated ERK1/2 at 15 min and 30 min post-LPS exposure (Fig. 4a). Bench-top immuno-staining protocols yield flow cytometry and Western blot results that qualitatively display similar macrophage response to LPS over the chosen time course. To assess temporal resolution available from the pFC technique, macrophage cells were challenged using the pFC device with 10 µME. coli LPS for 5 s, 5 min, 10 min, and 15 min (Fig. 4b). At the earliest time point (5 s), the pFC analysis revealed no detectable phosphorylation of ERK1/2. At later time points, pFC analysis revealed that phoshphorylated ERK1/2 peaked faster for the higher concentration of E. coli LPS at 37oC (10 min for 10µM LPS vs. 15 min for 1µM LPS). As previously shown, the range of shear rates applied during the ERK phosphoprofiling assays did not lead to activation of the macrophage cells (Fig. 2c). Researchers have recently begun to appreciate that different levels of ERK1/2 activity directly impact the expression of pro-inflammatory mediators and cytokines29 .

In addition to temporally resolved analysis via flow cytometry, spatial localization of MAP kinases can also be obtained using the pFC assay system. The pFC was operated mounted on an inverted microscope with DIC, phase contrast and fluorescence imaging capabilities to allow real-time monitoring of cell phenotype during the short term culture and challenge steps (Fig. 1, middle panel of the pFC monolith). As has been reported,

cells in a population do not all have the same initial physiological state or degree of infection 33, 34 35 . Fluorescence imaging of macrophage cells after phosphostaining and prior to their release for flow cytometry, revealed that under certain challenge conditions (e.g., 10 µM LPS, 5min), pERK1/2 was localized entirely in the cytoplasm (top image). Different challenge conditions (e.g., 10 µM LPS, 10min) resulted in a large fraction of the intracellular pERK1/2 having translocated into the nucleus (bottom image on the middle panel). Once in the nucleus, pERK regulates the levels and activities of critical transcription factors. Bright field imaging revealed that roughly 80% of the macrophage cell population in the incubation chamber were elongated and spread out on the planar surface. The cells also developed cytoplasmic filaments and filamentous bridges – possibly for inter-cell communication (data not shown). The observed phenotype is consistent with healthy, adherent cells. Further morphological assessment of the macrophage cells was made though visualization of the shape of the nucleus, as well as number of vacuoles and nucleoli inside the nucleus.

DISCUSSION

The pFC technique reported offers advantages over conventional bench top cell preparation methods for flow cytometry. Relying on microfluidic technologies, the pFC approach integrates preparatory processes required for phosphoprofiling studies relevant to characterizing intracellular signaling pathways. The pFC design exploits fine fluid control to manipulate and analyze small, yet statistically significant, numbers of cells (~2,000). The cell-preparation steps demonstrated with the pFC approach include: programmable duration cell-challenge periods, chemical fixation of cells, plasma

membrane permeabilization, fluorescent immunostaining and numerous intermediate buffer exchange and washing steps. To our knowledge, the pFC method is the first report of a comprehensive microfluidics-based tool integrating sophisticated cell challenge and preparation, imaging, and flow cytometric analyses. The pFC approach enables automated, multi-step preparatory protocols – thereby reducing the necessary manual intervention, making fine temporal investigations (~ seconds) accessible, and potentially improving the reproducibility of cell signaling measurements as reported in the present study.

Owing to the small length scales of the microdevice, efficient sample preparation and processing is possible. Low fluid and sample volumes are required, as less than 10 μL of sample is necessary to complete the reported analysis – roughly 0.1% of the volume required for conventional flow cytometry. The pFC-based pERK monitoring study required a fraction of the time needed to complete the analysis using conventional preparatory methods with flow cytometry (30 min plus infection vs. 120 min plus infection with conventional preparation).

To demonstrate monitoring of intracellular signaling after short LPS stimulation periods, we analysed pERK1/2 response in macrophage cells at 5 s post-stimulation. Stimulation periods on the order of a few seconds are difficult to implement with bench top cell handling methods, yet the 5 s period reported here was readily achievable using facile fluid handing enabled by microfluidic technology. In the TLR-4 signaling examined here, we do not expect nor do we observe pERK after a 5 s LPS stimulation interval, as ERK1/2 phosphorylation is reported to initiate no earlier than 5min36, 37. At earlier stimulations intervals (e.g., 2min), phosphorylated levels of ERK1/2 were not detected in

lipopolysaccharide stimulated macrophges36 . After slightly longer LPS stimulation intervals, we do observe both phosphorylation and dephorphorylation of ERK1/2, as would be expected. The shortest stimulation duration attainable using the pFC technology is determined by the time required for fluid exchange in the incubation chambers (i.e., volume of chamber, flushing volumetric flow rate). Based on the geometry of the fluidic network and the hardware used, the pFC tool could support flow rates an order of magnitude higher than the 5 s duration used in the present study. Employing such rapid fluid exchange conditions should yield an ultra-short incubation period of ~100 ms. That said, such high flow rates and short stimulation periods may not be appropriate for all systems. The latter consideration applies to pERK monitoring in the murine macrophage-LPS system currently under study.

An important aspect of the pFC tool design is elimination of conventional centrifuge-based cell washing steps required for phophoprofiling. To eliminate centrifuge-based washing, the pFC approach used in the present study employs channel surfaces (i.e., quartz) that allow macrophage cells to remain adherent under flowing fluid conditions. Such an approach is readily adaptable to other adherent cell types that includes but not limited to HepG2 (heptocellular carcinoma), HUVEC (vascular endothelium) and HeLa (cervical epithelial cells). While not designed for analysis of non-adherent cell types, design modifications to the pFC tool would allow preparation and analysis of non-adherent cell types. One such design modification under development by our group is incorporation of on-chip filters as a means to confine non-adherent cells to incubation chambers while allowing reagent exchange38 . Alternatively, surfaces functionalized with extracellular matrix (ECM) proteins such as fibronectin, collagen and laminin have

been used to enhance adherence of suspension cell lines. For instance, several suspension cell lines such as rat basophilic leukemia (RBL-2H3) used for in vitro studies on mast cells and basophils have responded favorably to ECM coatings39 . Elimination of centrifugation reduced cell losses and aggregate formation – making the pFC method attractive for the analysis of small populations of precious cells (i.e., primary cells, stem cells). Cell clumping, disintegration and cell loss due to centrifugation have been reported to be major obstacle to single cell studies especially in picoeukaryotic cells 40 . Centrifuge-free processing is attractive to low-resource environments (i.e., no centrifuges available). Host-pathogen interaction studies requiring biohazard specialized, space-limited facilities (i.e., Biosafety level 3 or 4 laboratories) could benefit from the monolithic devices demonstrated in this work.

The pFC technology provides phenotype characterization (i.e., morphology, protein translocation, nuclear-cytoplasmic ratio, co-localization of multiple markers) of individual cells in addition to the end-point detection of “averaged” fluorescence permitted by flow cytometry. In-chip imaging using standard epi-microscopy is performed on cells that are subsequently analyzed by flow cytometry, thus allowing correlation between cell phenotype and the biochemical response of the population. Rich data provided by the complementary methods integrated in the hybrid pFC tool make possible detailed characterization of confounding responses, such as bistability within a cell population. A bistable cell response is difficult to characterize using bulk measurement methods (i.e., Western blots, enzyme linked immunosorbent assays). The pFC approach was optimized to monitor and quantitate sub-cellular localization and time-response of intracellular protein phosphorylation events key to macrophage response to

LPS infection. Analysis of intracellular phosphorylation of other key signaling pathway proteins, the process of phagocytosis, and the formation of surface receptor complexes is underway using the pFC tool. Engagement of multiple intracellular signaling pathways defines the specificity, intensity and duration of gene expression that governs the innate and subsequent adaptive immune responses to pathogen challenge 29 . Further studies regarding LPS recognition by macrophage cells promise to contribute to developing novel strategies for therapeutic intervention (e.g., endotoxin shock). That said, the generic and versatile nature of pFC, with the capability of automation, controlled dosages, fast mixing, precisely timed incubation and selective routing of reagents and waste – makes the pFC tool applicable to exploring a wide variety of cell biology, immunology, and cancer biology questions.

METHODS Microfluidic chip design, fabrication, assembly and fluidic control: Chip designs were made in-house using AutoCAD 2000 (Autodesk Inc., San Rafael CA), photomasks were generated at Photo Sciences (Torrance, CA) and quartz microfluidic devices were fabricated by Caliper Life Sciences (Hopkinton, MA).

An array of eight holes (500 µm diameter) provided for fluid inlet. Fluidic connection to the inlet holes was made using an in-house designed plastic (delrin) manifold and PEEK tubing (125 µm ID, 1/32 in OD, Upchurch Scientific). Small ID of the PEEK tubing (125 µm) allowed for low residence time during reagent and cell delivery – which was critical in reducing cell loss by axial dispersion in the tubing. An in-house designed shut¬off electronic valve (response time < 1s, dead volume ~20 nL) was used inline with the PEEK tubing. On the other end, the PEEK tubing was immersed in an airtight sample/reagent reservoir. The reservoir was pressurized using house Nitrogen and

electronic pressure controllers (Parker Hanifin, Cleveland OH) in order to load sample/reagent into the chip. Typically pressures ranging from 0.2 to 5 psi were used during device operation. Higher pressures, up to 15 psi, were used if necessary to remove bubbles and during cleaning cycles. Each quartz chip could be used repeatedly with an appropriate cleaning protocol. Extreme care was taken during chip design and plumbing to minimize dead volume. All hydrophobic components of the plumbing interface i.e., PEEK tubing, valves, manifold etc. were primed with methanol and DI water to wet the surface and removes any air bubbles trapped inside. Finally, the microfluidic channels as well as the inlet holes were completely filled with DI water before the fluidic connections were made.

Microscopy and image analysis: Bright field, epifluorescent and phase contrast images were captured at 10X and 40X magnification on an Olympus IX71 inverted microscope equipped with a CoolSNAP HQ CCD camera (Photometrics) and Image-Pro software. In order to measure the aggregation index for onchip and offchip cells, images were further analyzed on ImageJ. A typical image processing algorithm would involve – background subtraction (rolling ball radius = 50, with white background unchecked), setting lower and upper levels on the threshold to convert to a binary image, and finally analyzing the particles based on size and circularity to show outlines for single cells and for aggregates. The analyze particles plugin in ImageJ was used to measure the number of single cells and aggregates.

SUPPLEMENTAL METHODS

Cell culture, passaging and phosphorylation assay: RAW 264.7 murine macrophage cell line was bought from ATCC (Manassas, VA) and was used for all studies. Macrophages were cultured in growth medium consisting of 450 mL DMEM, 50 mL FBS (gemcell), 5 mL HEPES, 5 mL glutamine (200 mM) and 1:100 Penicillin /Strap. 5*106 cells/mL stock concentration was used to load cells on the chip. All on-chip assays were validated with conventional benchtop setups such as the BD FACScan. For these benchtop assays, macrophages were challenged with smooth E. coli LPS (Sigma-Aldrich, # L4524) inside an incubator (37 oC, 5% CO2). At various pre-determined incubation time points (i.e., 5 s, 15 min, 30 min, 60 min), the LPS challenged macrophage cells were fixed (temporally and spatially) using 2% Paraformaldehyde (Electron Microscopy Sciences, Hatfield PA) at RT for 10 min, washed, permeabilized with 100% Methanol (Electron Microscopy Sciences, Hatfield PA) at RT for 20 min, washed and labeled with fluorescently tagged phospho-specific monoclonal antibodies (Cell Signaling Technology, Inc #4374) for 20 min at RT. After two more washes, the labeled cells were analyzed on a FACScan (BD Biosciences) equipped with a 488nm Argon ion laser & three detection channels (FL1-green, FL2-yellow & FL3-red). Washing is performed by forming a pellet using centrifugation at 400g for 5min & then re-suspending the pellet in phosphate-buffered saline (pH 7.4) solution.

Temperature Control on the pFC platform: The pFC platform is mounted on a thermal control setup to achieve the desired temperature regulation during cell culture and stimulation. The thermal control setup consisted of a thermoelectric hot plate (CP-036, TE Technology Inc) and a proportional integral controller (TC¬24-12, TE Technology Inc). A temperature sensing thermistor is directly attached to the quartz chip to provide

temperature feedback to the controller. The setup is capable of maintaining temperatures from 0 oC to 100 oC within an accuracy of + 0.1 oC.

Step-by-step operation of the device for phosphorylation assay: A typical protein phosphorylation assay consists of the following steps (see supplemental Fig. 2). Each of the eight ports on the pFC device (Fig 1b) are connected to external electronic valves to selectively turn them on or off on demand. First, macrophage cells are delivered to the device with only ports 1 and 8 open while the valves to all the ports (2 -7) are shut off. Once the two spiral chambers (1 and 2) are populated with cells in growth media, the flow is stopped. Another 5 min is allowed to allow the cells to settle, spread and adhere to the surface. Precise timed exposure of the macrophages to the stimulus is achieved by controlled, stopped flow conditions. The stimulant flows such that only the cells in spiral 1 are exposed to the stimulus. After pre-determined timed incubation, the remaining reagents (2 % paraformaldehyde, methanol, PBS buffer, antibody staining solution) are serially injected from port 2 to port 8, thus treating macrophage cells in both the spiral incubation chambers. Once the cells have been labeled, a second fixation with 3% paraformaldehyde was necessary before trypsin treatment to prevent damage to the intracellular target proteins. Finally, a combination of high shear rates (3,000 s-1) and purified trypsin (0.5 mg/mL) is used to detach cells – first in the second incubation chamber and then in the first incucbation chamber. As the cells detach and flow towards the waste port, they are pinched by sheath fluid (1X PBS buffer) to hydrodynamically focus them for fluorescent detection. The cells may also be collected from the waster reservoir in port 8 and analyzed on the BD FACScan.

Fluorescent detection for on-chip flow cytometry: The in-house microfluidic detection platform for on-chip flow cytometry was developed to emulate the performance, accuracy & capabilities of a conventional BD flow cytometer. The fluorescence illumination was derived from an air-cooled 15 mW argon ion laser (Melles Griot) with a single wavelength emission at 488 nm. The optical train consisted of a series of adjustable mirrors and a 60X air objective for epifluorescence illumination through which the laser beam was introduced to the on-chip detection window. The microfluidic device was placed on a mechanical stage with precise horizontal (x & y) and vertical (z) control. The emitted light from the hydrodynamically focused stream of cells was collected through two fluorescence filter cubes with a dichroic mirror (505 DRLP (green) & 650 DRLP (red) by Omega Optical, Inc) and associated emission filters (535 AF45 (green), 695 AF55 (red)). The collected light from each filter cube was relayed to two Hamamatsu Photomultiplier tubes and the PMT gain was tuned using a Hamamatsu H5784 PMT Interface/Controller. In addition, the scatter signal from an optical fiber positioned on top surface of the quartz device was relayed to a third Hamamatsu Photomultiplier tube. The real-time signal from the PMT was collected using a computer equipped with National Instruments CompactRIO programmable automation controller (PAC). The data was further analyzed using Peak Finder in LabVIEW (National Instruments) to construct population histograms of time resolved phosphorylation assays. The Peak Finder program uses the LabVIEW Peak Fit routine to fit the peak of the raw signal traces from the PMT (green, red and scatter) with a polynomial fit returning the peak amplitude and width. A model Gaussian peak is then computed and overlaid for each peak in the raw trace for visual validation to make sure that the polynomial fit was accurate. Once the parameters

that accurately fit the raw PMT traces have been optimized, the amplitudes of the peak is then used to build histograms in Matlab.

Adhesion assay: Since special coatings were not necessary to promote cell-substrate adhesion, bare quartz was used in all assays. Owing to the accessible operating range of the pFC flow controllers, 1.7 nN was the highest force measurable. Flow rate (Q) on the device is measured using a flow sensor (Nano Flow Sensor, Upchurch) from which the mean velocity ($v = Q/(w*d)$) is calculated. We then calculate the corresponding shear rates ($\gamma = 6v/d$) and shear stress ($\tau = \mu\gamma$). The average force ($F = \tau A$) on an individual cell was determined by approximating the surface area (A) of the cell that was exposed to the shear stress (τ).

Cleaning protocol: After each assay, the quartz based pFC device was cleaned with 10 % bleach (20 min) at 95 oC (to completely eliminate LPS) and DI water (10 min) and reused with no loss in efficiency or reproducibility.

ACKNOWLEDGMENTS

We acknowledge Dr. C. Branda, Mr. D. Throckmorton, Dr. K. Patel, Mr. H. Tran and Dr. T. Perroud of Sandia National Laboratories for helpful discussions and for providing materials. Funding was provided by the Sandia National Laboratories internal Laboratory Directed Reseach and Development Office, through the Microscale Immune Studies Laboratory “Grand Challenge” project.

FIGURE CAPTIONS

Figure 1 | Microfluidic pFC technique enables streamlined, automated phosphoprofiling of macrophage response to LPS on a monolithic platform. A schematic of the pFC protocol (left) and analogous benchtop paradigm (right) are shown for comparison. Device operation and benchtop protocol proceed from top to bottom of the schematic. Smooth spiral geometries in the pFC allow ready integration of the pressure-driven and stopped flow conditions to automate single-cell preparation and analysis via imaging and flow cytometry. Cells are added into the top left pFC well and the automated pFC intracellular phosphorylation assay proceeds as: i) cell culture and infection, ii) phosphostaining (2% paraformaldehyde fixation, cold methanol permeabilization, washing, and staining with phospho-specific antibodies) iii) flow cytometry (bottom channel). Microscopy images (middle panel) from the spiral incubation chambers show macrophages that were intracellularly labeled with phospho-specific ERK antibodies. Fluorescence images show the time-resolved recruitment of phosphorylated ERK (pERK) to the nucleus. The two wide spirals (1 and 2 on pFC image, left) enable simultaneous infection and control (i.e., no drugs) experiments. Cells are collected for further analysis from bottom right well. For detailed operation of the device, see supplementary Fig S2. Scale bards indicate: 1 mm, 200 µm, 10 µm, 100 µm(clockwise).

Figure 2 | Firm Adhesion and Rapid reagent Exchange on the pFC tool (a) Shear flow assays in spiral chambers (labeled 1 and 2 in Fig. 1) indicate macrophage cell adhesion to quartz exceeds 1.7 pN, the maximum force available in the device (flow rate of 50 µL/min). Stars indicate > 99% of cells attached to channel wall as the shear rate was increased by two orders of magnitude. (b) Flow cytometric analysis reveals that levels of phosphorylated ERK in macrophage cells that handled high shear rates on the pFC was

comparable to that from unstimulated (no LPS infection) cells (c) Rapid reagent exchange within the spiral chambers requires less than 5 s to replace reagent A (fluorescent antibody solution) with reagent B (a non-fluorescent buffer solution) at 5 µL/min flow rate. The arrow indicates the start of the reagent flushing assay. Error bars represent single standard deviation from three different experimental runs. For some data points, the error bars are smaller than the symbols used.

Figure 3 | pFC enables high-quality cell preparation via well-controlled cell handling.(a) Bright field (BF) and fluorescence images of macrophage cells in spiral incubation chamber after stimulation (10 min with 10 µM E.coli LPS), after the phosphostaining process, and after trypsin release. Cells are well-spread and confined to the incubation chamber with minimal cell release until addressed with trypsin. Scale bar, 20µm. (b) FACscan side & forward scatter density plot reveal that 70+9 % of cells prepared using the pFC tool were present as single cells (R1) compared to 45+6 % from conventional preparation (n = 8). Error denotes a 96 % confidence interval. Histogram plots of the fluorescence intensity from the cells in region R1 has a higher coefficient of variation for benchtop prepared cells (46 %), as compared to cells prepared using the pFC tool (29 %). The tighter spread of fluorescence intensity from pFC cells is attributed to uniform antibody staining among the cell population. Even with the same antibody titration, the fluorescence intensity (AF488) levels in the histogram for pFC preparation is higher – we attribute this to the fact that the cells are adherent on the pFC tool (c) Bright field images of prepared cells confirm lower aggregation index (0.17 vs. 0.91) for pFC prepared cells. Bar, 100 µm.

Figure 4 | pFC phosphorylation assay of ERK1/2 shows time-dependent response to E. coli LPS stimulation.(a) Flow cytometry detects the phosphorylation states of ERK after challenge with E. coli LPS (1 µM) at 15 min and 30 min by both conventional and pFC preparation. Western blot analysis shows ERK1 and ERK2 phosphorylation as a function of time. (b) Phosphorylation of ERK1/2 occurs by 5 min post-challenge under high E. coli LPS (10 µM) challenge. Significant ERK1/2 phosphorylation is not detected at ultra short challenges of 5 s.

REFERENCES

1. Weijer, C.J. Visualizing signals moving in cells. Science 300, 96-100 (2003).

2. Zorov, D.B., Kobrinsky, E., Juhaszova, M. & Sollott, S.J. Examining intracellular organelle function using fluorescent probes -From animalcules to quantum dots. Circulation Research 95, 239-252 (2004).

3. Perez, O.D. & Nolan, G.P. Simultaneous measurement of multiple active kinase states using polychromatic flow cytometry. Nature Biotechnology 20, 155-162 (2002).

4. Sachs, K., Perez, O., Pe'er, D., Lauffenburger, D.A. & Nolan, G.P. Causal protein-signaling networks derived from multiparameter single-cell data. Science 308, 523-529 (2005).

5. www.bdbiosciences.com, www.amnis.com, www.beckmancoulter.com.

6. Carty, D.J., Spielberg, F. & Gear, A.R.L. Thrombin Causes Subsecond Changes in Protein-Phosphorylation of Platelets. Blood 67, 1738-1743 (1986).

7. Raha, S., Jones, G.D. & Gear, A.R.L. Sub-Second Oscillations of Inositol 1,4,5-Trisphosphate and Inositol 1,3,4,5-Tetrakisphosphate During Platelet Activation by Adp

and Thrombin -Lack of Correlation with Calcium Kinetics. Biochemical Journal 292, 643-646 (1993).

8. Nolan, G.P. & Sklar, L.A. The emergence of flow cytometry for sensitive, real-time measurements of molecular interactions. Nature Biotechnology 16, 633-638 (1998).

9. Sklar, L.A., Edwards, B.S., Graves, S.W., Nolan, J.P. & Prossnitz, E.R. Flow cytometric analysis of ligand-receptor interactions and molecular assemblies. Annual Review of Biophysics and Biomolecular Structure 31, 97-119 (2002).

10. Huh, D., Gu, W., Kamotani, Y., Grotberg, J.B. & Takayama, S. Microfluidics for flow cytometric analysis of cells and particles. Physiological Measurement 26, R73-R98 (2005).

11. Simonnet, C. & Groisman, A. High-throughput and high-resolution flow cytometry in molded microfluidic devices. Analytical Chemistry 78, 5653-5663 (2006).

12. Palkova, Z., Vachova, L., Valer, M. & Preckel, T. Single-cell analysis of yeast, mammalian cells, and fungal spores with a microfluidic pressure-driven chip-based system. Cytometry Part A 59A, 246-253 (2004).

13. Chan, S.D.H., Luedke, G., Valer, M., Buhlmann, C. & Preckel, T. Cytometric analysis of protein expression and apoptosis in human primary cells with a novel microfluidic chip-based system. Cytometry Part A 55A, 119-125 (2003).

14. Fu, A.Y., Spence, C., Scherer, A., Arnold, F.H. & Quake, S.R. A microfabricated fluorescence-activated cell sorter. Nature Biotechnology 17, 1109-1111 (1999).

15. Wang, M.M. et al. Microfluidic sorting of mammalian cells by optical force switching. Nature Biotechnology 23, 83-87 (2005).

16. Gomez-Sjoberg, R., Leyrat, A.A., Pirone, D.M., Chen, C.S. & Quake, S.R. Versatile, fully automated, microfluidic cell culture system. Analytical Chemistry 79, 8557-8563 (2007).

17. Petronis, S., Stangegaard, M., Christensen, C.B.V. & Dufva, M. Transparent polymeric cell culture chip with integrated temperature control and uniform media perfusion. Biotechniques 40, 368-376 (2006).

18. Zhu, X.Y. et al. Arrays of horizontally-oriented mini-reservoirs generate steady microfluidic flows for continuous perfusion cell culture and gradient generation. Analyst 129, 1026-1031 (2004).

19. Gu, W., Zhu, X., Futai, N., Cho, B.S. & Takayama, S. From the Cover: Computerized microfluidic cell culture using elastomeric channels and Braille displays. Proceedings of the National Academy of Sciences 101, 15861-15866 (2004).

20. Abhyankar, V.V. & Beebe, D.J. Spatiotemporal micropatterning of cells on arbitrary substrates. Analytical Chemistry 79, 4066-4073 (2007).

21. El-Ali, J., Gaudet, S., Gunther, A., Sorger, P.K. & Jensen, K.F. Cell stimulus and lysis in a microfluidic device with segmented gas-liquid flow. Analytical Chemistry 77, 3629-3636 (2005).

22. Wang, Z.H., Kim, M.C., Marquez, M. & Thorsen, T. High-density microfluidic arrays for cell cytotoxicity analysis. Lab on a Chip 7, 740-745 (2007).

23. King, K.R. et al. A high-throughput microfluidic real-time gene expression living cell array. Lab on a Chip 7, 77-85 (2007).

24. El-Ali, J., Sorger, P.K. & Jensen, K.F. Cells on chips. Nature 442, 403-411 (2006).

25. Sims, C.E. & Allbritton, N.L. Analysis of single mammalian cells on-chip. Lab on a Chip 7, 423-440 (2007).

26. Lipniacki, T., Paszek, P., Brasier, A.R., Luxon, B.A. & Kimmel, M. Stochastic regulation in early immune response. Biophysical Journal 90, 725-742 (2006).

27. Takeda, K., Kaisho, T. & Akira, S. Toll-like receptors. Annual Review of Immunology 21, 335-376 (2003).

28. Akira, S. & Takeda, K. Toll-like receptor signalling. Nature Reviews Immunology 4, 499-511 (2004).

29. Banerjee, A. & Gerondakis, S. Coordinating TLR-activated signaling pathways in cells of the immune system. Immunology and Cell Biology 85, 420-424 (2007).

30. Schooley, K., Zhu, P., Dower, S.K. & Qwarnstrom, E.E. Regulation of nuclear translocation of nuclear factor-kappa B relA: evidence for complex dynamics at the single-cell level. Biochemical Journal 369, 331-339 (2003).

31. Krutzik, P.O. & Nolan, G.P. Intracellular phospho-protein staining techniques for flow cytometry: Monitoring single cell signaling events. Cytometry Part A 55A, 61-70 (2003).

32. Gerondakis, S., Grumont, R.J. & Banerjee, A. Regulating B-cell activation and survival in response to TLR signals. Immunology and Cell Biology 85, 471-475 (2007).

33. Blake, W.J., Kaern, M., Cantor, C.R. & Collins, J.J. Noise in eukaryotic gene expression. Nature 422, 633-637 (2003).

34. McAdams, H.H. & Arkin, A. Stochastic mechanisms in gene expression. Proceedings of the National Academy of Sciences 94, 814-819 (1997).

35. Swain, P.S., Elowitz, M.B. & Siggia, E.D. Intrinsic and extrinsic contributions to stochasticity in gene expression. Proceedings of the National Academy of Sciences 99, 12795-12800 (2002).

36. Shinohara, H. et al. Dok-1 and Dok-2 are negative regulators of lipopolysaccharide-induced signaling.

J. Exp. Med. 201, 333-339 (2005).

37. Beinke, S., Robinson, M.J., Hugunin, M. & Ley, S.C. Lipopolysaccharide activation of the TPL-2/MEK/extracellular signal-regulated kinase mitogen-activated protein kinase cascade is regulated by I kappa B kinase-induced proteolysis of NF-kappa B1 p105. Molecular and Cellular Biology 24, 9658¬9667 (2004).

38. Shediac, R. et al. Reversed-phase electrochromatography of amino acids and peptides using porous polymer monoliths. J. Chromatogr. A 925, 251-263 (2001).

39. Hamawy, M.M., Oliver, C., Mergenhagen, S.E. & Siraganian, R.P. Adherence of Rat Basophilic Leukemia (Rbl-2h3) Cells to Fibronectin-Coated Surfaces Enhances Secretion. J. Immunol. 149, 615¬621 (1992).

40. Biegala, I.C., Not, F., Vaulot, D. & Simon, N. Quantitative assessment of picoeukaryotes in the natural environment by using taxon-specific oligonucleotide probes in association with tyramide signal amplification-fluorescence in situ hybridization and flow cytometry. Applied and Environmental Microbiology 69, 5519-5529 (2003).

FIGURE 1:

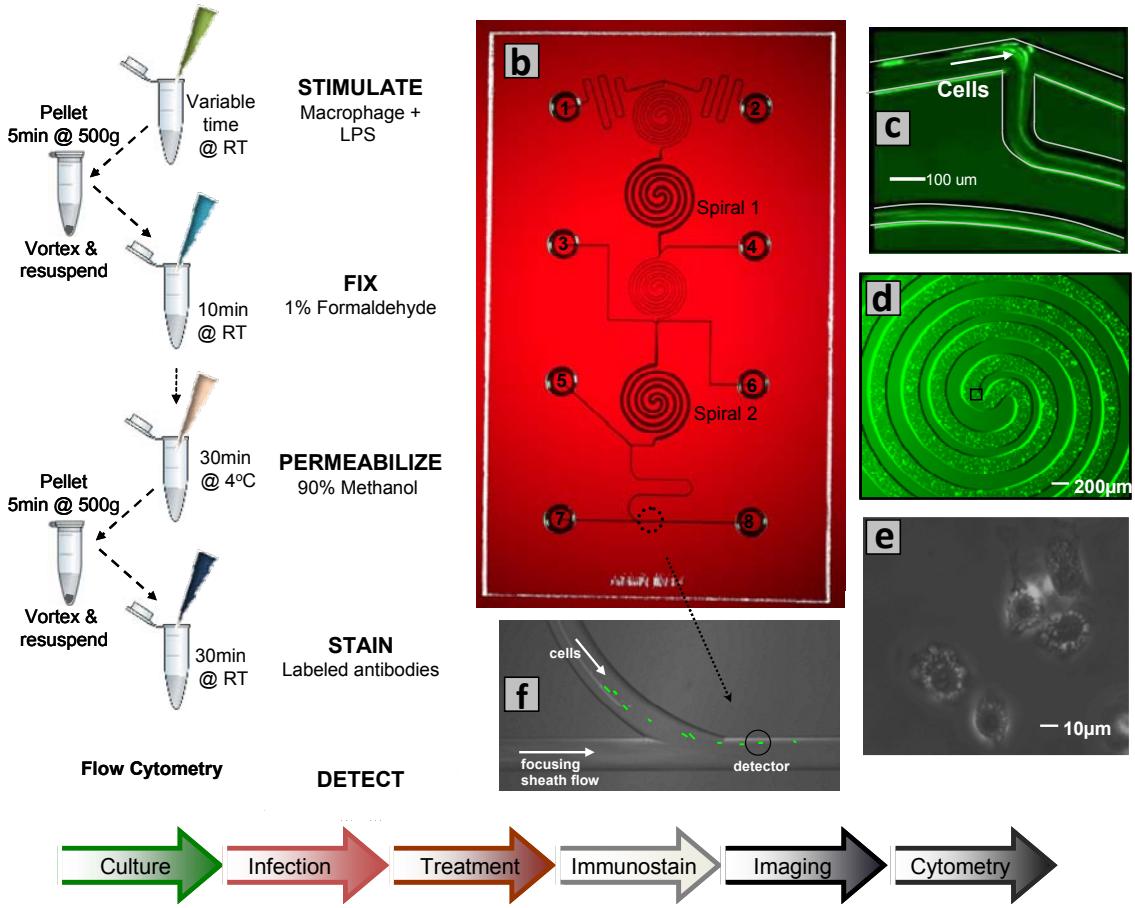
Pellet
5min @ 500g
Variable
time
@ RT
STIMULATE
Macrophage +
LPS
Vortex &
resuspend
10min
@ RT
FIX
1% Formaldehyde
30min
@ 4ºC
PERMEABILIZE
90% Methanol
Pellet
5min @ 500g
Vortex &
resuspend
30min
@ RT
STAIN
Labeled antibodies
Flow Cytometry
DETECT
b
Spiral 1
Spiral 2
c
Cells
100 um
d
200µm
e
10µm
f
cells
focusing
sheath flow
detector
Culture
Infection
Treatment
Immunostain
Imaging
Cytometry

Figure 2:

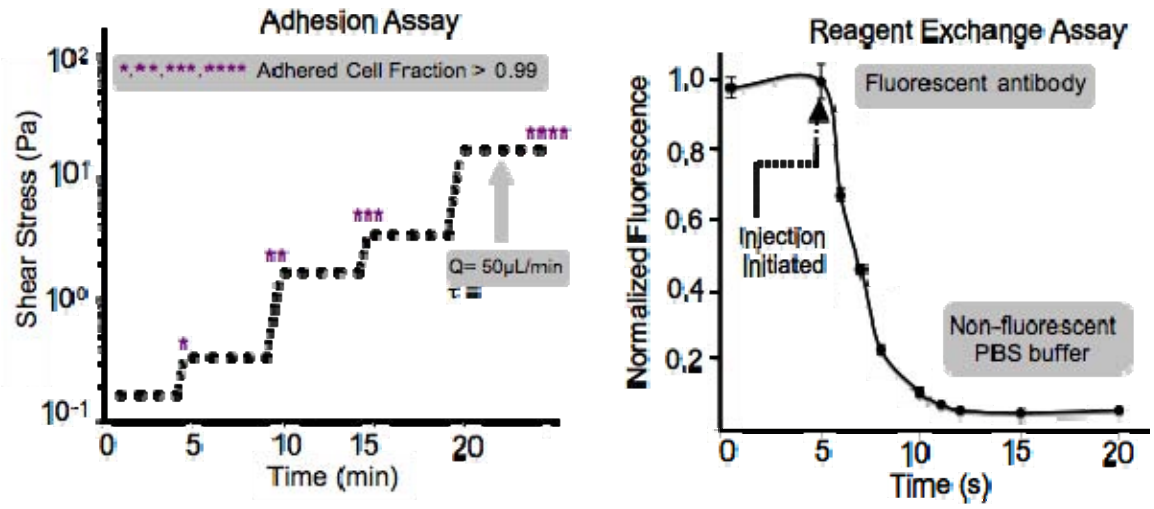
Adhesion Assay
*,**,***,**** Adhered Cell Fraction > 0.99
Shear Stress (Pa)
Q= 50μL/min
Time (min)
Reagent Exchange Assay
Fluorescent antibody
Normalized Fluorescence
Injection Initiated
Non-fluorescent PBS buffer
Time (s)

Figure 3:

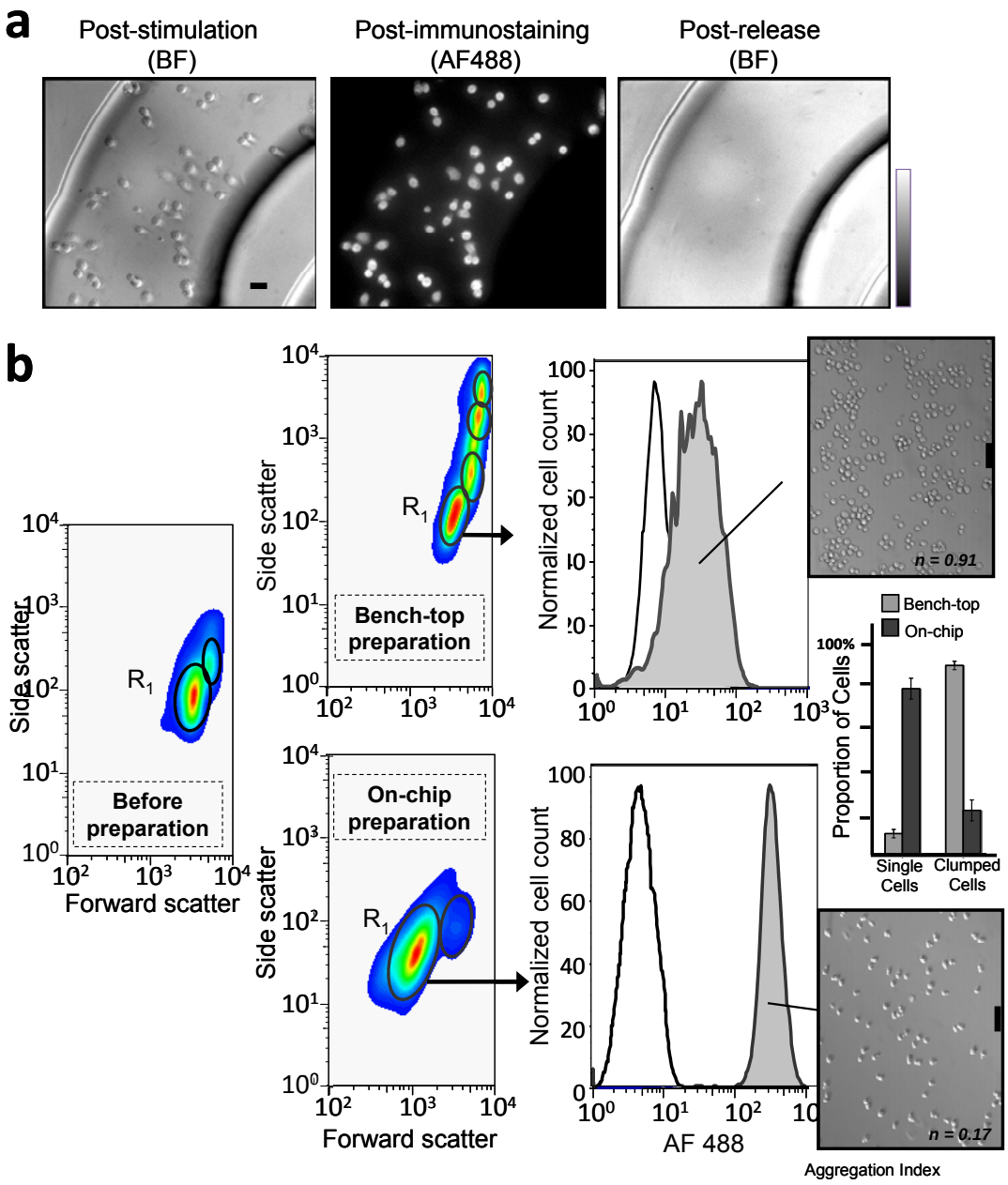
a
Post-stimulation (BF)
Post-immunostaining (AF488)
Post-release (BF)
b
Before preparation
Bench-top preparation
On-chip preparation
Side scatter
Forward scatter
Normalized cell count
AF 488
n = 0.91
n = 0.17
Bench-top
On-chip
Proportion of Cells
100%
Single Cells
Clumped Cells
Aggregation Index

Figure 4

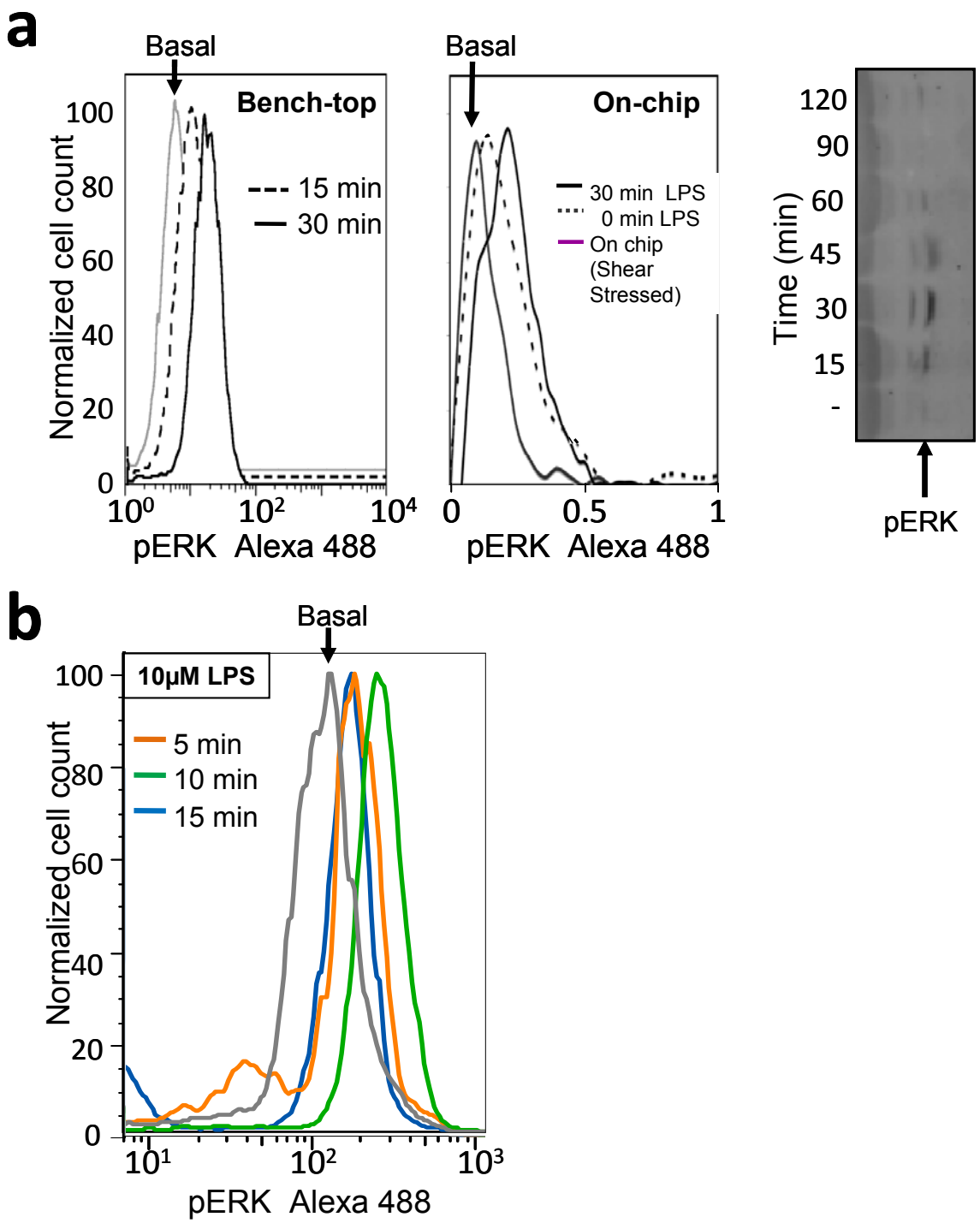
a
Basal
Bench-top
15 min
30 min
Normalized cell count
100
80
60
40
20
0
10^0
10^2
10^4
pERK Alexa 488
Basal
On-chip
30 min LPS
0 min LPS
On chip (Shear Stressed)
0
0.5
1
pERK Alexa 488
Time (min)
120
90
60
45
30
15
-
pERK
b
Basal
10μM LPS
5 min
10 min
15 min
Normalized cell count
100
80
60
40
20
0
10^1
10^2
10^3
pERK Alexa 488

Figure 5:

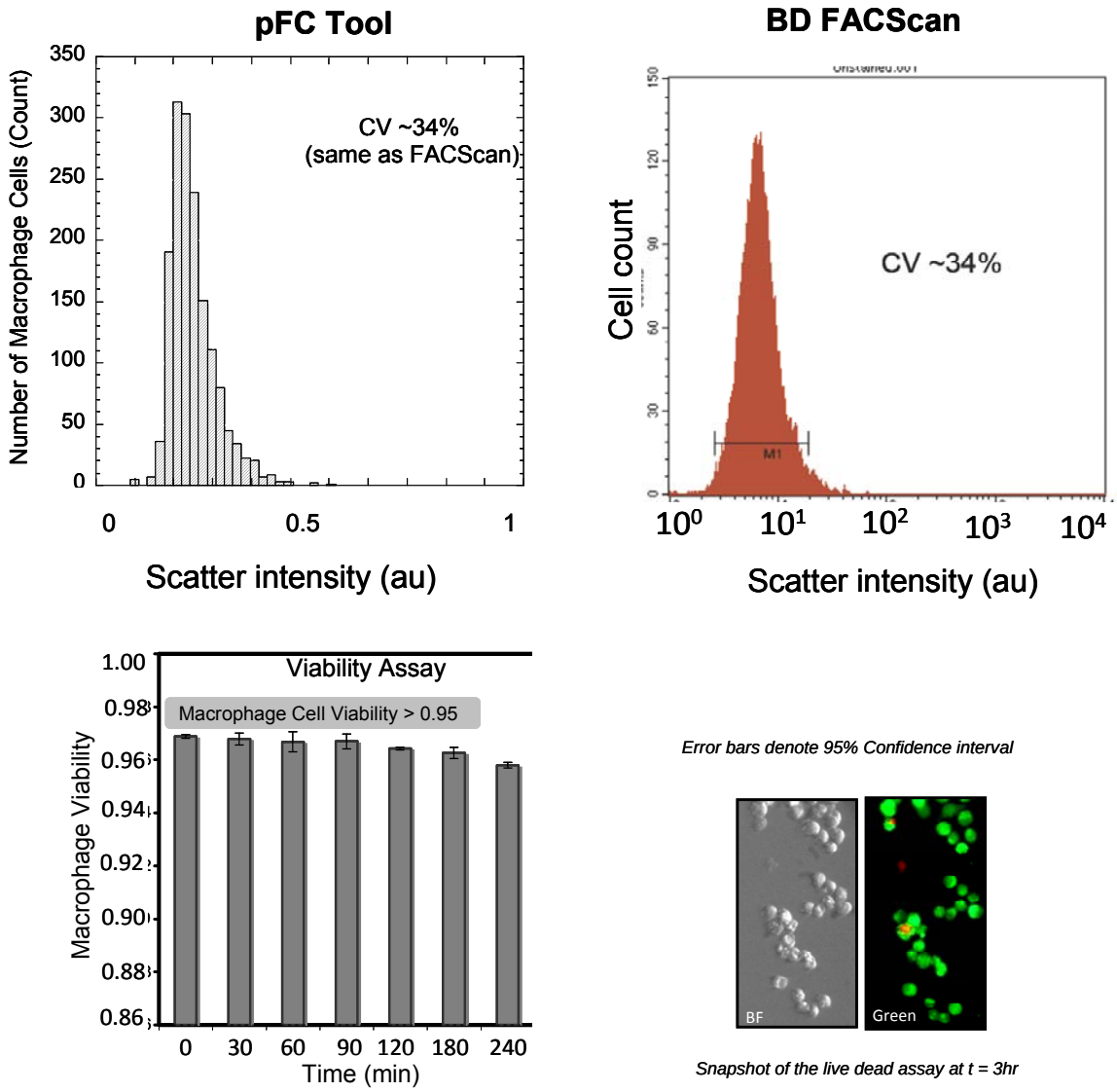
pFC Tool
Number of Macrophage Cells (Count)
CV ~34%
(same as FACScan)
Scatter intensity (au)
BD FACScan
Cell count
CV ~34%
M1
Scatter intensity (au)
Viability Assay
Macrophage Cell Viability > 0.95
Macrophage Viability
Time (min)
Error bars denote 95% Confidence interval
BF
Green
Snapshot of the live dead assay at t = 3hr

4. Microfluidic-Based Cell Sorting of *Francisella tularensis* Infected Macrophages using Optical Forces

Thomas D. Perroud, Julie N. Kaiser, Jay C. Sy, Todd W. Lane, Catherine S. Branda, Anup K. Singh, and Kamlesh D. Patel

Abstract:

We have extended the principle of optical tweezers as a noninvasive technique to actively sort hydrodynamically focused cells based on their fluorescence signal in a microfluidic device. This micro fluorescence-activated cell sorter (μFACS) uses a near-IR laser to laterally deflect cells into a collection channel. Green-labeled macrophages were sorted from a mixture at a throughput of 14-22 cells/s for 30 min and achieved a sorting purity as high as 97% with recovery yields between 55% and 63%. To rule out potential photo-induced cell damage during optical deflection, we investigated the response of mouse macrophage to brief exposures (< 4 ms) of focused 1064-nm laser light (9.6 W at the sample). We found no significant difference in viability, cell proliferation, activation state, and functionality between IR-exposed and unexposed cells. Activation state was measured by the phosphorylation of ERK and nuclear translocation of NF-κB while functionality was assessed in a similar manner, but after a lipopolysaccharide challenge. To demonstrate the selective nature of optical sorting, we isolated a subpopulation of

highly infected macrophages with the fluorescently labeled pathogen *Francisella tularensis* subsp. *novicida*. A total of 10,738 infected cells were sorted at a throughput of 11 cells/s with 93% purity and 39% recovery.

Introduction

Since the development of fluorescence-activated cell sorting (FACS),[1] scientists have been able to perform multi-parametric cell separations at sorting speeds of 10,000 cells/s. Such rapid and efficient analysis of heterogeneous cell suspensions has positioned benchtop FACS systems as an important diagnostic tool for hematology and oncology. However, benchtop FACS systems are used cautiously when working with infectious agents or with live human cells. These droplet-based sorters become a serious biohazard because of the aerosols generated.[2, 3] Moreover, their large footprint and required maintenance make these instruments impractical for routine use in BSL3 and BSL4 facilities. Given the recent advent of microfluidic-based system biology,[4] a compact discovery platform with multiple integrated functionalities that guarantees a sterile environment and improved biosafety is highly desired for studying host-pathogen interactions. In particular, the integration of FACS functionality into microfluidic chips (μFACS) provides a critical link between upstream cell preparation and downstream single-cell analysis of specific subpopulations.

Numerous proof-of-concept sorting strategies for microfluidic-based cell sorters have been reported in the literature. Key examples include electrokinetic flow switching;[5, 6] hydrodynamic flow switching using on-chip valves,[7] off-chip valves,[8, 9] MEMS-based micro-T switches,[10] and a thermoreversible gelation polymer;[11]

dielectrophoretic forces on tagged[12] or untagged cells,[13, 14] and on droplets;[15] lastly, optical forces using a passive holographic lattice,[16] active trapping and binning into a single channel[17, 18] or multiple channels,[19] and placing/removing individual cells within an array of microwells.[20, 21]

The use of photonic forces to deflect living cells in a fluidic channel is based on the early work of optical trapping of cells.[22] To prevent damage to the cell by light absorption, most trapping lasers operate in the near infrared (780-1330 nm), where biological material is quasi-transparent.[23] A tightly focused laser beam creates strong gradient forces that trap a cell at its center, hence the term optical tweezers. The strength of the trap depends on the laser power, the refractive index of the cell relative to the surrounding media, and the numerical aperture of the focusing lens. For cell sorting, trapping is not required since only lateral deflection matters, allowing the use of lower numerical aperture lenses (< 0.6).[17] Moreover, the longer depth of focus increases the likelihood of deflecting a cell regardless of its vertical position within the microfluidic channel.

The noninvasive nature of cell sorting based on optical forces makes it an attractive approach when handling pathogens. Additionally, this sorting mechanism is disconnected from the chip fabrication simplifying its integration with other on-chip functionalities and making it more affordable for single use. Optical sorting can be based either on the intrinsic properties of the cells (passive) or on fluorescent markers (active) similar to conventional FACS.[24] Notably, Wang et al.[18] have shown that a microfluidic-based optical cell sorter could actively sort GFP-expressing HeLa cells at a high-throughput rate relative to other μFACS (20-100 cells/s).

Given the above-mentioned advantages of cell sorters based on optical forces for host-pathogen studies, we have adapted this technique to isolate a subpopulation of macrophages infected by the pathogen *Francisella tularensis*, a Gram-negative coccobacillus. *Francisella tularensis* subspecies *tularensis* is considered to be a potential bioweapon because of its high virulence, low infectious dose, and ease of aerosol dissemination.[25] It has the ability to survive phagocytosis by macrophages, key sentry cells of the innate immune system, and can multiply in and escape from the phagososome. Since *Francisella tularensis* subsp. *novicida* displays little or no ability to infect humans but is fully virulent in mouse macrophages, it represents a safe surrogate to validate our microfluidic-based cell sorter for host-pathogen studies.

In the present article, we describe our microfluidic-based optical sorter for cellular analysis. A gage of the overall performance of our μFACS is presented by sorting dye-labeled macrophages from a mixture. In addition, we investigate the effects of brief exposure to high-level of near-infrared laser light on the viability, proliferation, activation state, and functionality of mouse macrophages. Finally, we apply our technology to isolate a subpopulation of mouse macrophages infected by a fluorescently labeled pathogen, *Francisella tularensis* subsp. *novicida*.

EXPERIMENTAL SECTION

Chip fabrication and packaging. Microfluidic chips are custom-fabricated by Caliper Life Sciences (Mountain View, CA) using conventional wet-etching and photolithographic processes. Specific to their process, microchannels (30-μm deep and

70-μm wide) are isotropically etched in 0.75-mm-thick fused-silica base wafers (Figure 1B). Fluid access holes (2-mm diameter) are drilled into a cover wafer before being visually aligned and thermally bonded to the base wafer with the combined wafers diced into individual 22.6 × 37.2 mm chips. To prevent cell adhesion, the channels were coated with a thin PEG-silane film. This protocol is described in detail elsewhere,[26] with the exception of 3% polyethylene glycol acrylate (469823; Sigma) as a monomer and 0.5% (w/v) 2,2'-azobis[2-methylpropionamidine] dihydrochloride (992-11062; Wako Chemicals, Richmond, CA) as a photoinitiator. A Delrin polymeric microfluidic manifold with integrated O-ring seals provides the interface between the chip and fluid reservoirs.[27] Fluid is delivered to each port of the manifold through 1/32" O.D. 0.005" I.D. PEEK tubing (Upchurch Scientific, Oak Harbor, WA) and swaged in place with 1/32" TubeTite fittings (Labsmith, Livermore, CA). 2.0 mL screw-cap microcentrifuge tubes (89004-302; VWR, West Chester, PA) fitted with custom-machined caps serve as fluid reservoirs. The caps have two ports to allow the delivery of N_2 gas to pressurize the headspace in the vial and push the fluid through a PEEK tube placed below the liquid level into the chip. All four fluid reservoirs are pressurized by individual electronic pressure control units (VSO-EP; Parker, Cleveland OH) to ensure precise control of hydrodynamic focusing, cell velocity, and cell positioning.

Optical cell sorter. The cell sorter is based on a modified two-stage inverted microscope (TE-2000U; Nikon Instruments, Melville, NY) with an automated micropositioning stage (MS-2000; ASI, Eugene, OR), a monochrome fast CCD camera on the front port (1000 fps UF-1000CL; Uniq Vision, Santa Clara, CA), and a blue and

infrared CW lasers coupled to the back of the microscope (Figure 1A). The 20 mW 488-nm solid-state laser (Cyan; Newport, Irvine, CA) is split into two beams, which are then focused by a cylindrical lens at the back-aperture of a 20X 0.45 N.A. microscope objective (Plan Fluor ELWD; Nikon Instruments). The two beams not only detect and interrogate cells, but also measure their velocities. The 20 W 1064-nm Ytterbium fiber laser (YLM-20; IPG Photonics, Oxford, MA) is coupled to an acousto-optical modulator (AOM ATD-274HD6; IntraAction, Bellwood IL) before being focused by the same 20X objective. Transmission losses along the optical path of the near-IR laser reduce the total power to 9.6 W at the sample (75% transmission for AOM, 64% for 20X objective[23]). Forward scattering of the blue laser is detected through an optical fiber (JTFSH 600-μm core; Polymicro Technologies, Phoenix, AZ) and a bandpass filter with blocker (488NB2.6; Omega, Brattleboro, VT) connected to a photomultiplier (H5784-20; Hamamatsu, Bridgewater, NJ). Laser-induced fluorescence emission is split (600DCXR longpass filter; Chroma, Rockingham, VT) into a green channel (D527/30m bandpass filter) and a red channel (HQ610/30m bandpass filter) before being detected by two photomultipliers. All three photomultipliers voltages (scatter, green, and red) are recorded by a data acquisition module (NI 9401; National Instruments, Austin, TX). In addition, these voltages are processed by a custom-made digital counter to register each event and select the sorting decision signal. This signal initiates a precise time-delayed TTL pulse (DG535; Stanford Research System, Palo Alto, CA), provided that the voltage peak exceeds a preset minimum threshold. The time delay (2.4 ms) corresponds to the time defined by the distance between the two blue laser spots (approximately 50 μm) and by the velocity of the cells (approximately 21 mm/s). This TTL pulse is sent to a

function generator with a pre-loaded 250 Hz negative ramp function (HP33120A; Agilent, Santa Clara, CA) connected to the AOM (DE-272), which turns on the infrared laser and rasters it across the microfluidic channel at a 13 deg angle.

Cell culture and reagents. Mouse macrophage cell line RAW 264.7, kindly provided by the Seaman lab (UCSF, San Francisco, CA), was grown on non-treated sterile flasks and maintained in growth media: DMEM (0.87X) supplemented with 1:100 Penicillin / Streptomycin, L-glutamine (2 mM), 10% FBS, and HEPES (20 mM). To prevent cells from settling to the bottom of the reservoir during a sorting experiment, the growth media was supplemented with 14% Optiprep. The $p_{\beta Actin}$-EGFP-RelA construct was derived from pECFP-F-RelA, a kind gift from Dr. Allan R. Brasier (University of Texas Medical Branch, Galveston, TX). ECFP was replaced with EGFP between the Age1 and BsrG1 sites, and the cytomegalovirus promoter was replaced with a minimal 106bp human βActin promoter[28] cloned between the Ase1 and Nhe1 sites. Macrophages were challenged with smooth *E. coli* LPS (L4524; Sigma-Aldrich, St Louis, MO) for 45 min inside an incubator (37°C, 5% CO_2). Macrophages were labeled with either 5 μM Calcein-AM (3100MP, green), or 5 μM SNARF-1 AM ester (C1272, red) and mixed at appropriate ratios. For live cells, all washing steps were performed at 400 g for 5 min. Unless specified, all dyes were purchased from Invitrogen and other reagents from Fisher Scientific.

Cell viability and proliferation studies. Cell viability was assessed using a live-dead assay containing both 1 μM calcein AM and 2 μM ethidium homodimer dyes (L3324).

Cell growth was assessed by the 3-(4,5-dimethylthiazol-2-yl)-2,-5-diphenyltetrazolium bromide assay (MTT; Sigma) according to the manufacturer's instructions after a 48 h incubation period in growth media at 37°C and 5% CO_2.

Immunostaining assays and flow cytometry. The intracellular phospho-protein staining methodology is described elsewhere.[29] Briefly, cells were fixed for 10 min at room temperature with 1.5% paraformaldehyde (Electron Microscopy Sciences, Fort Washington, PA). Cells were then washed and permeabilized by resuspending them vigorously in 100% ice-cold methanol. To determine ERK activation, cells were washed twice at 3000 g for 10 min with staining buffer and resuspended in a solution of Phospho-p44/42 MAPK (Thr202/Tyr204) (E10) mouse monoclonal antibody conjugated to Alexa-488 at a 1:50 dilution (Cell Signaling Technology, Danvers, MA). After a 1 h incubation period at 4°C in the dark, cells were washed at 3000 g for 10 min and resuspended in PBS. All flow cytometry measurements were performed on a BD FACScan (BD Biosciences, San Jose, CA) equipped with a 488-nm argon ion laser and three detection channels (FL1-H green, FL2-H yellow, and FL3-H red). Data was analyzed using FlowJo software (Tree Star, Ashland, OR).

Pathogen growth and labeling with Alexa Fluor 488. *Francisella tularensis* subsp. *novicida* strain Utah 112 (NR-13; BEI Resources, Manassas, VA) is grown in tryptic soy broth (BBL 211768) supplemented with 0.1% L-cysteine (TSBC). An overnight culture is diluted 1:50 into 25 mL TSBC and grown at 37°C with shaking (200 rpm) for 4 h. Ten milliliters of the culture is pelleted at 4300 rpm for 10 min and resuspended in 0.6 mL

sterile DPBS (14190-144; Invitrogen) containing 0.1 M sodium bicarbonate. Alexa-488 dye (A20000) was resuspended in DMSO to 20 mg/mL, and was added to the cell suspension (0.4 mg dye per 10 mL of a mid-log culture), which was then rotated in the dark for 1 h at room temperature. The labeled cells were washed three times with 1 mL DPBS, resuspended in 2.5 mL TSBC containing 20% glycerol, and aliquoted into 250 μL freezer stocks. Bacterial titers were determined by plate counts on TSBC agar.

Macrophage infection. The infection method for RAW264.7 mouse macrophages with *F. tularensis* subsp. *novicida* U112 is adapted from Lauriano et al.[30] Briefly, macrophages were seeded onto 2-wells chambered coverglasses (155379; Nunc, Rochester, NY) in antibiotic-free growth media one day prior to infection at 3.5×10^5 cells/well. An aliquot of Alexa-488 labeled bacteria was thawed and opsonized in 50% mouse complement serum (IMS-COMPL; Innovative Research, Novi, MI) for 30 min at 37°C and was resuspended in antibiotic-free growth media immediately prior to use. Macrophages were infected with subsp. *novicida* U112 at an input ratio of 200 bacteria per macrophage in 1 mL per well of antibiotic-free growth media. The coverglasses were centrifuged at 300 g for 10 min to increase the contact between bacteria and macrophages. After a 3 h incubation at 37°C in 5% CO_2, adherent cells were gently washed 4 times with DPBS and dissociated following a 5 min incubation with 0.5 mL cell dissociation solution (S-014-B; Millipore, Billerica, MA). DPBS was added up to 10 mL, and the suspension was centrifuged at 300 g for 5 min; cells were resuspended in phenol red free antibiotic-free growth media with 14% Optiprep for cell sorting.

Confocal microscopy. Macrophages were imaged by laser-scanning confocal microscopy (MRC1024ES; Biorad, Hercules, CA). For imaging, adherent macrophages were infected on 4-wells chambered coverglasses (154526; Nunc), and stained with 5 µg/mL CellMask Deep Red plasma membrane dye (C10046) for 5 min at 37°C. After one wash with PBS, cells were fixed with 2% paraformaldehyde for 30 min, followed by three PBS washes. Coverslips were mounted with ProLong Gold Antifade Reagent (P36934; Invitrogen) and allowed to dry overnight before imaging. The cell membrane stained with Deep Red plasma membrane dye was excited by the 635 nm laser line, while the pathogen labeled with Alexa-488 was excited at 488 nm. Three-dimensional reconstruction consisted of the acquisition of sequential 0.5-µm confocal images from an individual macrophage of 10-µm-thick section using 3D Doctor software (Able, Lexington, MA).

Safety considerations. Class IV lasers are dangerous and standard personal protective equipment should be used, including protective eyewear. BSL2 practices were followed in handling the pathogenic sample.

RESULTS AND DISCUSSION

Principle and performance of µFACS

As shown in Figure 1C, the center channel of our µFACS design is divided into two distinct regions: an upstream flow cytometry and a downstream cell-sorting region.

The sample stream entrained with cells is focused by two neighboring sheath flows into a 10- to 15-μm-wide vertical plane. This planar focusing aligns the cells in a single-file manner. As a result, each cell is detected and analyzed sequentially by an interrogation laser and then sorted by a near-IR laser.

To illustrate the sorting principle and the decision-making process outlined in Figure 2, a sequence of four bright-field images are extracted from a high-speed movie (Supplemental Figure 1). A hydrodynamically focused macrophage traversing the spot of the interrogation laser generates a forward-scattering signal detected by a photomultiplier tube (Figure 2A). This signal is compared to a threshold voltage, which serves as the decision-making criteria for sorting. Crossing this threshold, the signal generates a TTL pulse after a predetermined delay (8 ms), corresponding to a 6 mm/s cell velocity to travel from the 488-nm laser spot to the near-IR laser spot. This TTL pulse triggers a function generator sending a negative ramp function to the AOM, which rasters the near-IR laser. The shape of the function is important to maximize the interaction time between the laser and the cell. The function consists of four events (Supplemental Figure 2): an immediate rise to turn on the near-IR laser at the center of the focused-sample stream; a plateau to hold the beam in place until the cell arrives; a negative slope to translate the beam at a defined angle (22 deg) for a distance of 54 μm; and a rapid fall to turn off the laser resetting it for the next sorting event. When the cell enters the near-IR laser spot (Figure 2B), the laser starts translating at the same speed, but with a different trajectory, than that of the cell. This difference results in gradient forces that deflect the cell laterally (Figure 2C). The overall effect is a displacement of a macrophage from the center of the channel to a neighboring flow stream (Figure 2D). The laminar nature of

fluid flows in microfluidics ensures that the cell will stay on this path for downstream binning.

The 150-μm-wide central channel is bifurcated into 80-μm-wide waste and 70-μm-wide collection channels (Figure 1C). The channel lengths and widths have been optimized in COMSOL finite elemental analysis software such that the hydrodynamically focused flow is directed into the waste channel allowing only deflected cells to enter the collection channel. Although the exact split geometry is not critical for sorting, the configuration shown in Figure 1C is preferred to a symmetrical T- or Y-type geometry. The side-split geometry is more tolerant for sorting partially deflected cells and prevents aggregates from entering the collection channel. In addition, this design is less likely to have cells lodged irreversibly at the sorting interface, which ultimately increases chip lifetime. Further improvements to the sorting efficiency can be gained by adjusting the pressure balance at the outlet ports in real-time, thereby refining the exact location of the focused sample stream with respect to the split geometry.

Cell sorters are commonly characterized by three metrics: (1) *throughput* represents the average number of cells analyzed and sorted during a defined period of time; (2) *recovery* is the ratio between the number of cells that were sorted and the total number of cells that should have been sorted; and (3) *purity* is the fraction of positive cells in the collected sample. To measure all three metrics for our system, a predetermined ratio of green-labeled to red-labeled cells is sorted into a collection channel. All inputs and outputs (sample, waste, and collection) are analyzed off-chip by fluorescence microscopy and by a benchtop FACScan flow cytometer, which requires sorting tens of thousands of cells with our device. To achieve sufficient throughput, we

favored high initial cell densities (4 x 10^6 cell/mL), fast cell velocities (21 mm/s), and a small angular deflection (13 deg). The first two factors result in small distances between successive cells and in large drag forces, increasing the probability of a miss and thus decreasing recovery. A small angular deflection results in a small cell displacement, thus increasing chances that unwanted cells accidentally enter the collection channel (false positive) and decreasing overall purity.

Three different ratios of green-labeled to red-labeled macrophages (10/90, 40/60, and 90/10) were tested on our optical cell sorter (Table 1). We sorted green-labeled macrophages from a 40/60 ratio and all inputs and outputs were analyzed off-chip by microscopy imaging (Figure 3A). A total of 38,877 cells were sorted at a throughput of 22 cells/s with 93% purity and 60% recovery. The high purity achieved is further confirmed by FACScan flow cytometry, where only the green cells subpopulation is detected in the collection channel (Figure 3B). Overall, cell throughput ranges from 14 to 22 cells/s. Variation in throughput between experiments is likely caused by macrophage aggregation and settling in the fluid reservoir. This effect limited each sorting experiment to a period of 30 min. As expected, purity increases with an increasing fraction of green cells in the initial mixture since the probability of a false positive is weighted by the fraction of green cells in the initial sample. For all three sorting experiments, the key feature of our optical cell sorter is the high purity achieved; a characteristic of a sorting mechanism based on optical tweezers.

Effect of IR laser on viability, activation, and functionality of mouse macrophages

To efficiently overcome the drag forces associated with a macrophage

cell (diameter 10-15 μm) and achieve rapid cell sorting (~20 cells/s), high near-IR laser power is required at the sample (9.6 watts). We believe that macrophages should not be damaged by this intense laser light for three reasons: (1) at 1064 nm, most of the light is refracted into the cell and its surrounding avoiding heat-related damages through absorbance;[23] (2) each cell is briefly exposed to the laser (< 4 ms) minimizing the amount of energy delivered (< 37 mJ/cell); (3) similar optical manipulation of HeLa[18] and BaF3 cells[21] have resulted in no obvious cell damage. Nevertheless, macrophages are the primary sentry cells for the immune system; and in their role, macrophages are highly sensitive cells that can respond directly and indirectly to a number of stimuli, including cytokines,[31] virus,[31] peptides,[32] and ionizing radiation.[33] It is therefore essential to ensure that exposure of macrophages to this intense laser light does not affect the signaling mechanism of the cell. To answer this question, we compared the viability, proliferation, activation state, and functionality of IR-exposed and unexposed mouse macrophages.

The viability of macrophages sorted through our device was assessed by a conventional live-dead assay, where calcein AM detects intracellular esterase activity and ethidium homodimer checks for membrane integrity. The difference in viability between IR-exposed (91%) and unexposed cells (95%) was found not to be significant ($p < 0.05$). Cell proliferation was assessed in triplicates 48 h after laser light exposure by an MTT colorimetric assay, which measures mitochondrial activity. Cell proliferation was found to be similar in both samples (> 85% viable cells).

MAP kinases ERK, a specialized intracellular signal relay protein, and NF-κB, a multi-subunit transcription factor, are considered important activation nodes of the Toll-like receptor 4 pathway, relevant to hematopoietic immune cells activation such as

macrophages and dendritic cells.[34] We investigated activation of IR-exposed and unexposed macrophages by the phosphorylation of ERK and the nuclear translocation of NF-κB. The phosphorylation of ERK was measured by staining macrophages with fluorescently labeled phosphospecific antibody followed by off-chip flow cytometry analysis.[29] Lipopolysaccharide (LPS), a component of Gram-negative bacterial cell walls and a potent stimulator of macrophages, was used as a positive (+ LPS) and negative control (- LPS) to show relative shifts in fluorescence distribution. Flow cytometry showed no difference in the degree of ERK phosphorylation between IR-exposed and unexposed cells (Figure 4A). Additionally, IR-exposed cells showed a similar fluorescent distribution as the negative control suggesting that the ERK pathway stays inactive. To monitor nuclear translocation of NF-κB, RelA, one of the subunits of NF-κB, was tagged with GFP in a stably transfected macrophage cell line. RelA-GFP expressing cells were sorted and imaged off-chip using conventional fluorescence microscopy. The presence of RelA in the cytosolic part of sorted cells showed that NF-κB was not translocated into the nucleus following optical deflection (Figure 4B). This result indicates that macrophages were not activated and is consistent with the absence of ERK phosphorylation after IR exposure.

Finally, we verified that the functionality of signaling pathways is conserved in IR-exposed macrophages by subjecting them to a 45-min LPS challenge. The phosphorylation of ERK was confirmed by conventional flow cytometry (Figure 4C). The fluorescence distribution of LPS challenged IR-exposed macrophages shows good overlap with the positive control (+ LPS, unexposed). Furthermore, GFP-RelA translocated into the nucleus thus ruling out any passivation of the signaling pathway

(Figure 4D).

Overall, we are confident that brief exposure (< 4 ms) of powerful near-IR laser light (9.6 watts) does not affect the viability, proliferation, activation state, and functionality of mouse macrophages thus validating optical deflection as a sorting mechanism for macrophages.

Infection of mouse macrophages by *Francisella Tularensis* subsp. *novicida*

To isolate a subpopulation of highly infected mouse macrophages, *Francisella tularensis* subsp. *novicida* was labeled with the amine-reactive Alexa-488 succinimidyl ester. This labeling strategy is derived from fluorescein isothiocyanate labeled bacteria used for phagocytosis studies.[35] Alexa-488 labeling does not affect the pathogen viability as assessed by dilution plating (data not shown). RAW 264.7 mouse macrophages were infected at 37°C for 3 h at a 200:1 multiplicity of infection (MOI), the ratio of bacterial cells to macrophages. Such high MOI might be surprising given the fact that as few as 10 organisms of the subspecies *tularensis* can cause severe diseases.[25] It is however consistent with previous results showing that a 500:1 MOI is required to achieve an averaged uptake of 2 attenuated live vaccinate strain bacteria derived from *F. tularensis* subsp. *holarctica* per J774 mouse macrophage.[36] Similarly, Bolger et al.[37] have shown that a 400:1 MOI is needed for this bacteria to infect 50% of the murine bone marrow-derived macrophages.

The phagocytic capacity of RAW 264.7 macrophages for *F. tularensis* subsp. *novicida* labeled externally with Alexa-488 was characterized by laser-scanning confocal microscopy and flow cytometry. The macrophage membrane was stained with a red

amphipathic dye prior to the infection with the green-labeled pathogen. The 3D reconstruction of the infected pathogen shows both an internalized as well as a surface-adherent bacteria (Figure 5A). To assess the extent of bacteria internalization, we performed a flow cytometry assay with Trypan blue, a vital stain that quenches Alexa-488 fluorescence of surface-adherent bacteria.[35] The addition of Trypan blue (0.12%) did not significantly shift the fluorescence histogram, suggesting that the majority of the bacteria are located inside the macrophages (data not shown).

Flow cytometry on infected macrophages results in a broad fluorescence histogram indicating a wide variation in the number of labeled pathogens per macrophage (Figure 5B). This variability is illustrated in Figure 5C, where fluorescence microscopy shows three, one, or no labeled pathogen per cell.

As an application of our microfluidic-based optical cell sorter for host-pathogen studies, we isolated a subpopulation of highly infected mouse macrophages from an initial mixture of uninfected and infected macrophages (Figure 6). This mixture as well as the samples recovered from the waste and collection channels were analyzed off-chip by a FACScan flow cytometer. A total of 10,738 cells were sorted at a throughput of 11 cells/s with 93% purity and 39% recovery. The throughput and recovery were lower than that of the green and red mixture of macrophages (see Table 1) due to the increased tendency of infected macrophages to form aggregates. Nevertheless, the 93% purity achieved in the collected sample confirms the high selectivity of the method.

CONCLUSIONS

Microfluidic-based cell sorter using optical deflection as a sorting mechanism is a proven approach for selecting a subpopulation of live, unstressed, and functional macrophages. We have shown that macrophages infected with *Francisella tularensis* subsp. *novicida* can be safely sorted in a sterile environment, illustrating the potential of this sorting technique for more pathogenic samples. The high purity achieved becomes important when integrating cell sorting functionality with downstream single-cell imaging, a technique with limited throughput. These unique advantages makes optical cell sorting an enabling technology towards multiplexed measurements on an integrated platform for studying host-pathogen interaction in a BSL3/BSL4 facility.

ACKNOWLEDGMENTS

The authors would like to thank M. Wu, N. Srivastava, D. D. Yee, R. F. Renzi, and J. S. Brennan for their assistance. We also appreciate inspiring discussions with B. D. Carson, S. S. Branda, and A. E. Herr. This research was fully supported by Laboratory Directed Research and Development program at Sandia National Laboratories. Sandia is a multiprogram laboratory operated by Sandia Corporation, a Lockheed Martin Company, for the United States Department of Energy's National Nuclear Security Administration under contract DE-AC04-94AL85000.

REFERENCES

(1) Herzenberg, L. A.; Sweet, R. G.; Herzenberg, L. A. *Scientific American* **1976**, *234*, 108-116.

(2) Schmid, I.; Nicholson, J. K. A.; Giorgi, J. V.; Janossy, G.; Kunkl, A.; Lopez, P. A.; Perfetto, S.; Seamer, L. C.; Dean, P. N. *Cytometry* **1997**, *28*, 99-117.

(3) Schmid, I.; Lambert, C.; Ambrozak, D.; Marti, G. E.; Moss, D. M.; Perfetto, S. P. *Cytometry Part A* **2007**, *71A*, 414-437.

(4) Breslauer, D. N.; Lee, P. J.; Lee, L. P. *Molecular Biosystems* **2006**, *2*, 97-112.

(5) Fu, A. Y.; Spence, C.; Scherer, A.; Arnold, F. H.; Quake, S. R. *Nature Biotechnology* **1999**, *17*, 1109-1111.

(6) Dittrich, P. S.; Schwille, P. *Analytical chemistry* **2003**, *75*, 5767-5774.

(7) Fu, A. Y.; Chou, H. P.; Spence, C.; Arnold, F. H.; Quake, S. R. *Analytical Chemistry* **2002**, *74*, 2451-2457.

(8) Kruger, J.; Singh, K.; O'Neill, A.; Jackson, C.; Morrison, A.; O'Brien, P. *Journal of Micromechanics and Microengineering* **2002**, *12*, 486-494.

(9) Wolff, A.; Perch-Nielsen, I. R.; Larsen, U. D.; Friis, P.; Goranovic, G.; Poulsen, C. R.; Kuttera, J. P.; Telleman, P. *Lab on a Chip* **2003**, *3*, 22-27.

(10) Ho, C. T.; Lin, R. Z.; Chang, H. Y.; Liu, C. H. *Lab On A Chip* **2005**, *5*, 1248-1258.

(11) Shirasaki, Y.; Tanaka, J.; Makazu, H.; Tashiro, K.; Shoji, S.; Tsukita, S.; Funatsu, T. *Analytical Chemistry* **2006**, *78*, 695-701.

(12) Hu, X. Y.; Bessette, P. H.; Qian, J. R.; Meinhart, C. D.; Daugherty, P. S.; Soh, H. T. *Proceedings of the National Academy of Sciences of the United States of America* **2005**, *102*, 15757-15761.

(13) Lapizco-Encinas, B. H.; Simmons, B. A.; Cummings, E. B.; Fintschenko, Y. *Analytical Chemistry* **2004**, *76*, 1571-1579.

(14) Kim, U.; Shu, C. W.; Dane, K. Y.; Daugherty, P. S.; Wang, J. Y. J.; Soh, H. T. *Proceedings of the National Academy of Sciences of the United States of America* **2007**, *104*, 20708-20712.

(15) Ahn, K.; Kerbage, C.; Hunt, T. P.; Westervelt, R. M.; Link, D. R.; Weitz, D. A. *Applied Physics Letters* **2006**, *88*, 24104-24101.

(16) MacDonald, M. P.; Spalding, G. C.; Dholakia, K. *Nature* **2003**, *426*, 421-424.

(17) Tu, E.; Zhang, H. C.; Wang, M. M.; Raymond, D. E.; Yang, J. M.; Hagen, N.; Dees, B.; Mercer, E. M.; Forster, A. H.; Attari, S.; Richardson, C.; Kariv, I. B.;

Chachisvillis, M.; Hara, M.; Marchand, P. J.; Butler, W. F. In *Optical Trapping and Optical Micromanipulation*; Dholakia, K., Spalding, G. C., Eds., 2004; Vol. 5514, pp 774-785.

(18) Wang, M. M.; Tu, E.; Raymond, D. E.; Yang, J. M.; Zhang, H. C.; Hagen, N.; Dees, B.; Mercer, E. M.; Forster, A. H.; Kariv, I.; Marchand, P. J.; Butler, W. F. *Nature Biotechnology* **2005**, *23*, 83-87.

(19) Applegate, R. W.; Squier, J.; Vestad, T.; Oakey, J.; Marr, D. W. M.; Bado, P.; Dugan, M. A.; Said, A. A. *Lab on a Chip* **2006**, *6*, 422-426.

(20) Luo, C. X.; Li, H.; Xiong, C. Y.; Peng, X. L.; Kou, Q. L.; Chen, Y.; Ji, H.; Ouyang, Q. *Biomedical Microdevices* **2007**, *9*, 573-578.

(21) Kovac, J. R.; Voldman, J. *Analytical Chemistry* **2007**, *79*, 9321-9330.

(22) Ashkin, A.; Dziedzic, J. M.; Yamane, T. *Nature* **1987**, *330*, 769-771.

(23) Svoboda, K.; Block, S. M.; Stroud, R. M. In *Annual Review of Biophysics and Biomolecular Structure*; P.O. Box 10139, 4139 El Camino Way, Palo Alto, California 94306, USA : Annual Reviews Inc., 1994, 1994, pp 247-285.

(24) Dholakia, K.; MacDonald, M. P.; Zemanek, P.; Cizmar, T. *Laser Manipulation of Cells and Tissues* **2007**, *82*, 467-495.

(25) McLendon, M. K.; Apicella, M. A.; Allen, L. A. H. *Annual Review of Microbiology* **2006**, *60*, 167-185.

(26) Hatch, A. V.; Herr, A. E.; Throckmorton, D. J.; Brennan, J. S.; Singh, A. K. *Analytical Chemistry* **2006**, *78*, 4976-4984.

(27) Renzi, R. F.; Stamps, J.; Horn, B. A.; Ferko, S.; VanderNoot, V. A.; West, J. A. A.; Crocker, R.; Wiedenman, B.; Yee, D.; Fruetel, J. A. *Analytical Chemistry* **2005**, *77*, 435-441.

(28) Quitschke, W. W.; Lin, Z. Y.; Depontizilli, L.; Paterson, B. M. *Journal of Biological Chemistry* **1989**, *264*, 9539-9546.

(29) Krutzik, P. O.; Nolan, G. P. *Cytometry* **2003**, *55A*, 61-70.

(30) Lauriano, C. M.; Barker, J. R.; Nano, F. E.; Arulanandarn, B. P.; Klose, K. E. *Fems Microbiology Letters* **2003**, *229*, 195-202.

(31) Mosser, D. M. *Journal of Leukocyte Biology* **2003**, *73*, 209-212.

(32) Tuckova, L.; Novotna, J.; Novak, P.; Flegelova, Z.; Kveton, T.; Jelinkova, L.;

Zidek, Z.; Man, P.; Tlaskalova-Hogenova, H. *Journal of Leukocyte Biology* **2002**, *71*, 625-631.

(33) Shan, Y. X.; Jin, S. Z.; Liu, X. D.; Liu, Y.; Liu, S. Z. *Radiation and Environmental Biophysics* **2007**, *46*, 21-29.

(34) An, H. Z.; Yu, Y. H.; Zhang, M. H.; Xu, H. M.; Qi, R. Z.; Yan, X. Y.; Liu, S. X.; Wang, W. Y.; Guo, Z. H.; Guo, J.; Qin, Z. H.; Cao, X. T. *Immunology* **2002**, *106*, 38-45.

(35) Nuutila, J.; Lilius, E. M. *Cytometry Part A* **2005**, *65A*, 93-102.

(36) Telepnev, M.; Golovliov, I.; Grundstrom, T.; Tarnvik, A.; Sjostedt, A. *Cellular Microbiology* **2003**, *5*, 41-51.

(37) Bolger, C. E.; Forestal, C. A.; Italo, J. K.; Benach, J. L.; Furie, M. B. *Journal of Leukocyte Biology* **2005**, *77*, 893-897.

FIGURE LEGENDS

Figure 1. Schematic of μFACS based on optical forces. A) Instrument layout with laser-induced fluorescence (LIF) excitation and emission paths, forward scattering detection, optical tweezers, and world-to-chip interface; B) Microfluidic chip of two independent sorting modules with inlets on the left and outlets on the right; C) Close-up on flow cytometry and sorting regions of chip where sample (blue dye) is hydrodynamically focused by two neighboring sheath flow (yellow) and split between a waste (left) and collection channel (right). The two hairpin turns reorient both channels into to the field of view to visually confirm sorted cells.

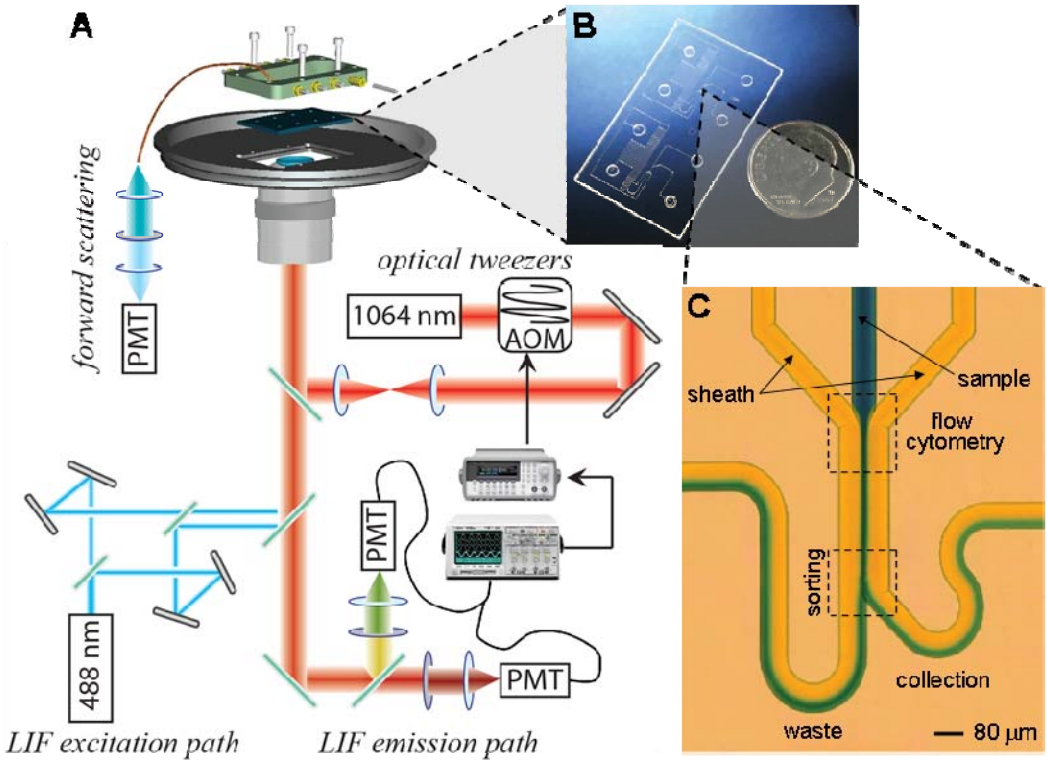

Figure 2. Principle and illustration of μFACS based on optical forces. A hydrodynamically focused macrophage is: A) detected by forward scattering; B) enters the near-IR laser spot; C) is deflected by optical gradient forces; D) and finally released in a different laminar flow stream. The corresponding high-speed movie can be found in the Supplemental Information.

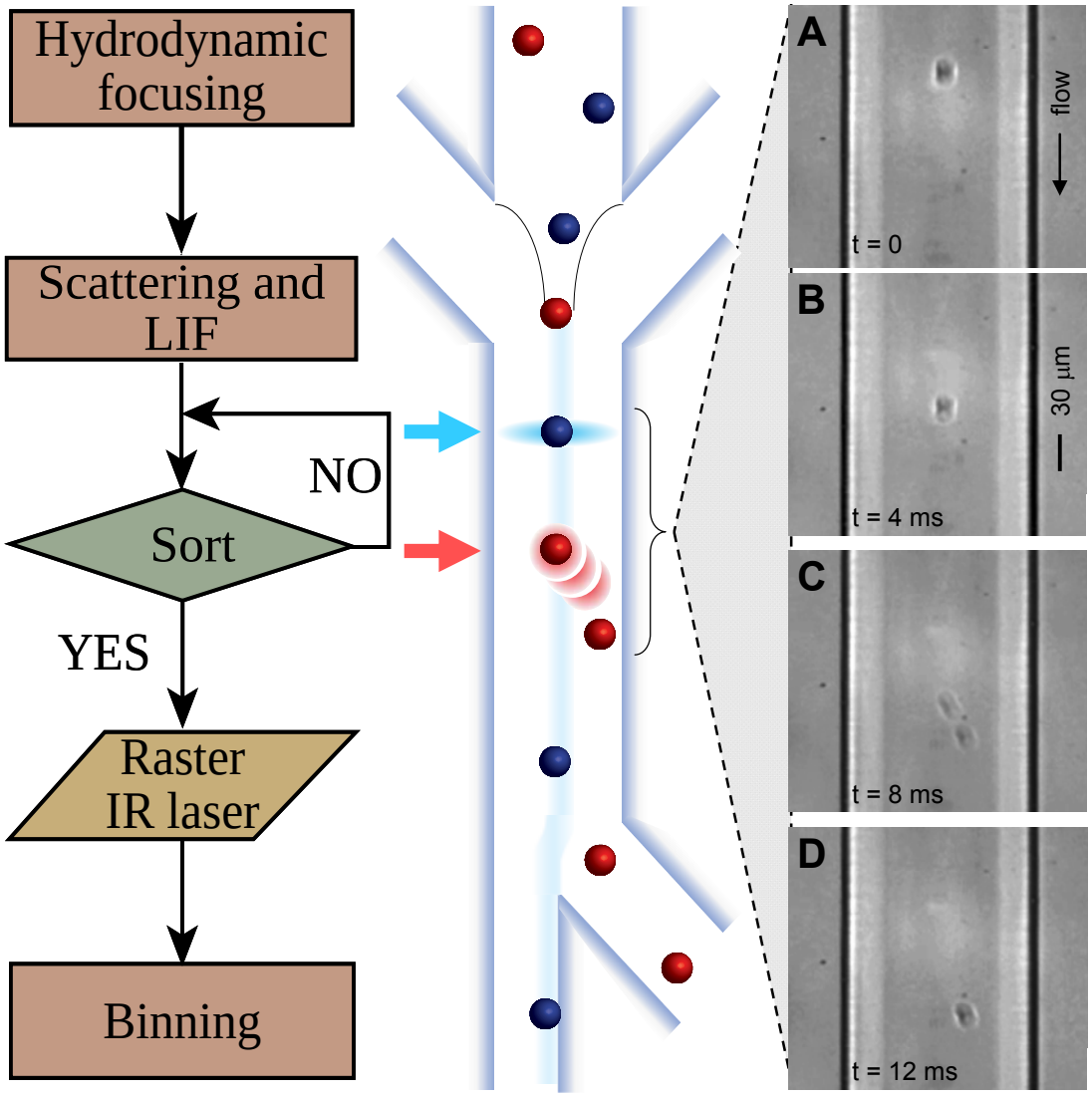

Figure 3. Characterization of μFACS performances by fluorescence microscopy (A) and flow cytometry (B). A mixture of 40% green-labeled and 60% red-labeled macrophages (A1), is sorted into a collection channel with 93% purity (A2), and into a waste channel with 60% recovery (A3). Benchtop FACScan flow cytometry confirms high purity in the collection channel (solid line).

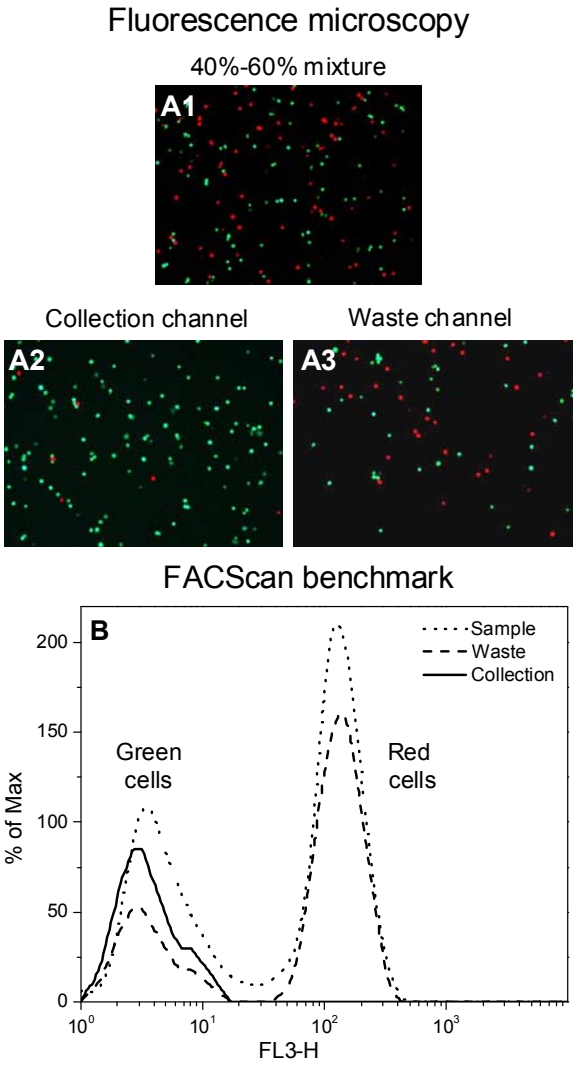

Figure 4. Activation state and functionality of mouse macrophages briefly (< 4 ms) exposed to 1064-nm laser light (9.6 W at the sample). Phosphospecific immunostaining followed by flow cytometry analysis shows that ERK remains unphosphorylated (A). Fluorescence microscopy confirms that GFP-RelA is located in the cytosol (B). After an LPS challenge, ERK is phosphorylated (C) and nuclear translocation of GFP-RelA occurs (D).

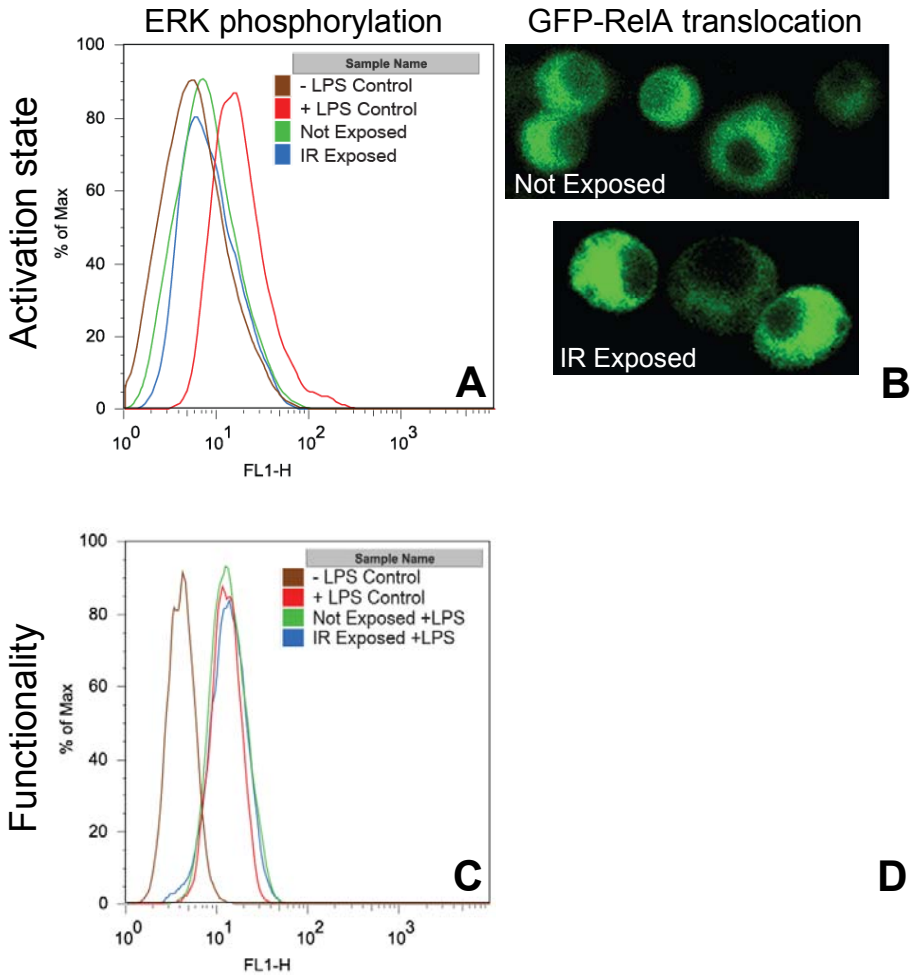

Figure 5. Infection of mouse macrophages by Alexa-488 labeled *Francisella tularensis* subsp. *novicida*. A) 3D reconstruction of stacked confocal images showing internalized as well as surface-adherent bacteria. B) Broad fluorescence histogram taken by FACScan flow cytometer indicating variability in the number of pathogens per macrophage. C) Variability in the number of pathogens (green) per macrophage shown by fluorescence microscopy.

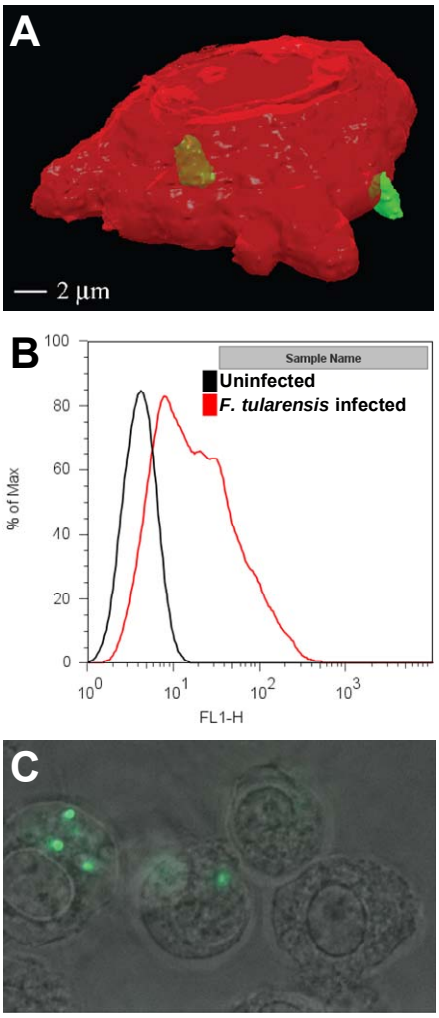

Figure 6. Isolation of a subpopulation of macrophages highly infected by Alexa-488 labeled *Francisella tularensis* subsp. *novicida*. Off-chip FACScan flow cytometry data for: initial mixture of infected and uninfected macrophages (red); waste channel (green); and collection channel (blue). A total of 10,738 cells were sorted at a throughput of 11 cells/s with 93% purity and 39% recovery.

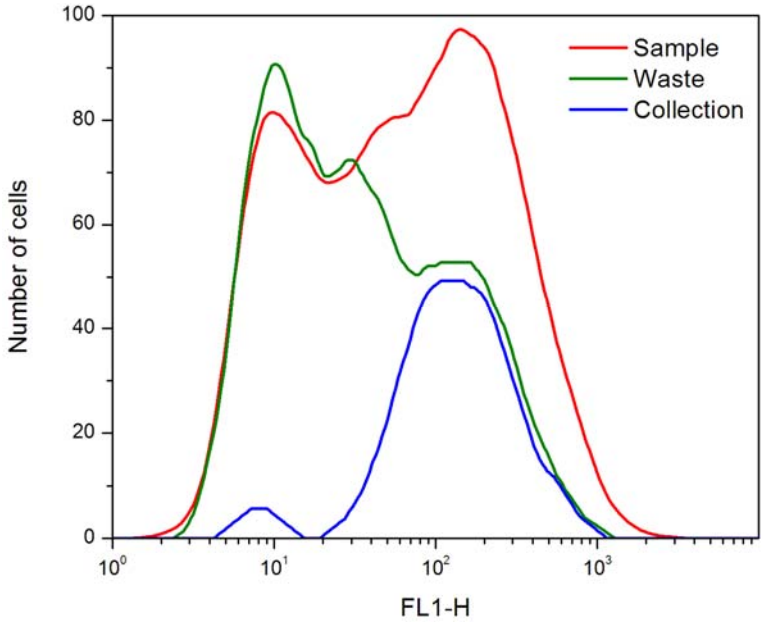

Table 1. μFACS performances at different ratios of green- to red-labeled macrophages. The initial cell density was set at $4x10^6$ cells/mL before loading the cells into the chip. Recovery and purity were determined by fluorescence microscopy (errors set as the standard deviation of 5 fields of view); throughput and cell number were measured in real time.

Green cells / red cells	Throughput [cells/s]	Recovery [%]	Purity [%]	Cell number
90/10	16	55 ± 5	97 ± 3	21,698
40/60	22	60 ± 10	93 ± 3	38,877
10/90	14	63 ± 9	75 ± 10	24,847

5. Dosage-dependent heterogeneous NF-kB response to LPS stimulation: computational model and single cell experiment

Jaewook Joo, Jens Poschet, Cathy Branda, Bryan Carson, and Anup Singh

Abstract:

Introduction: In biology the understanding has been prevalent, that a biological response to a known stimulus should be absolutely predictable, robustly uniform and homogeneous. However, due to very recent technical advances in single cell level studies, we begin to understand the probabilistic nature of the biological response. In fact, we see that these responses are rather uncertain, heterogeneous, and individualistic at the level of single cells, when confronted with a specific challenge. We study NF-κB translocation dynamics as a response to different stimulatory dosages of E. Coli LPS in single macrophages (RAW264.7 cells). Here, we present the dosage-dependent characteristics of NF-κB translocation patterns, predicted and explained by a computational model and corroborated and verified by a single cell fluorescence imaging technique.

Methods: To make the model specific to LPS stimulation, we incorporate into the computational model the following signaling pathways: TLR4-MyD88-NF-κB, TNF-R and TNFα autocrine positive feedback loop. In addition, our computational model is designed to simulate heterogeneous NF-κB response in single cells, by taking into account the cell-to-cell variability in key protein copy numbers and kinetic rate constants.

Results: First, the NF-κB translocation dynamic pattern in single cells is found to be quite heterogeneous; some cells show damped oscillations, some single-peaked patterns, and others rising patterns. These translocation dynamic patterns are much more mixed, thus more heterogeneous, with low dosage (1 nM) stimulation than with high dosage stimulation (100 nM). Second, for high dosage stimulation, a majority of the translocation patterns are highly oscillatory, which is in contrast to the previously published work by Covert et al. Third, for low dosage stimulation, most of the cells take a

rising pattern. Using the model only, we demonstrate that this rising pattern is due to the TNFα autocrine signaling effect.

Conclusion: This work will contribute to a novel and profound understanding on how single cells respond to different stimulatory dosage, using the computational modeling and bench-top experimental techniques.

Key Words: single cell behavior; protein dynamics; NF-kappaB translocation; extrinsic noise; cell-to-cell variability; TNF alpha autocrine signaling; computational model; fluorescence imaging

Target Journal: Molecular Systems Biology

I. Introduction

Integration of computation and single cell fluorescence imaging technique to unravel single-cell behavior: A computational model, if corroborated with experimental data, can be transformed into a powerful analytic and predictive tool and can be used to decipher "counter intuitive" signaling and/or gene-regulatory phenomena and to redirect the biological research by predicting new biological phenomena with novel insights. Advancement in single cell fluorescence imaging technique makes possible to monitor the protein dynamics within single cells (Nelson et al 2004; Lahav et al 2004). This new technique enables us to revisit, reinterpret, and even challenge previously well-accepted deterministic viewpoint prevalent in biology: a biological response to a known stimulus should be absolutely predictable, robustly uniform and homogeneous. In this paper we investigate dosage-dependent NF-κB response to *E. Coli* Lipopolyssachride (LPS) stimulation and re-examine the findings reported in the previous studies (Werner et al 2005; Covert et al 2005), employing both computational model and single cell fluorescence imaging technique.

Importance of NF-κB nucleo-cytoplasmic translocation dynamics: NF-κB is a stimulus-responsive pleiotropic regulator of gene control and plays significant roles on various parts of the immune system such as differentiation of immune system such as differentiation of immune cells, development of lymphoid organs, and immune activation

(Hoffmann et al., 2006; Verma and Stevenson, 2006). NF-κB shuttling between nucleus and cytoplasm is directly related to the control of the expression of NF-κB target genes and thus bears physiological importance. This shuttling is auto-regulated by IKK- NF-κB-IκB-A20 signaling module, which consists of four proteins, inhibitor κB (IκB; there are at least three isoforms of it), IκB kinase (IKK), A20, and NF-κB. In the absence of external stimulus, IκB forms a heterodimeric complex with NF-κB, preventing NF-κB from entering into the nucleus. Stimulation induces the nucleo-localization of NF-κB: IKK is phosphoryled, phosphorylated IKK catalyses the ubiquitin-assisted degradation of IκB from IκB: NF-κB complex, and as a result, NF-κB is freed up to shuttle into the nucleus, initiating transcription of NF-κB target genes such as inflammatory cytokines (TNFα , IL-1, IL-6), chemotactic cytokines (MIP-1α), anti-apoptic (IAPs), and lastly but most importantly NF-κB signal termination (IκB isoforms and A20) (reference). NF-κB signal terminating proteins (IκB isoforms and A20) form time-delayed negative feedback loops and NF-κB can readily oscillate between nucleus and cytoplasm in its own right (Novak and Tyson 2008).

NF-κB translocation dynamics at a population of cells and at single cells when stimulated by TNFα: TNFα stimulation induces a damped oscillatory NF-κB translocation pattern in a population of the wild type (embryonic mouse fibroblast) cells (Hoffmann et al 2002). When the mutant cells with IκBβ and IκBε double genes knocked-out are stimulated by TNFα, NF-κB dynamics averaged over the millions of cells is highly oscillatory whereas in a population of the mutant cells with either other IκB double genes knocked-out or A20 gene knocked-out, NF-κB dynamics is non-oscillatory (or single-peaked). On the contrary, Nelson et al reported that, when fluorescence reporters of RelA and IκBα proteins are constructed into the wild type human AS-SK cells, NF-κB translocation dynamics at those single cells take a quasi-sustained oscillatory pattern, which lasts about 12 hours after TNFα stimulation.

NF-κB response at a population of cells when stimulated by LPS: Covert et al in ref. (Covert et al. 2005) showed that when stimulated by LPS the NF-κB dynamics averaged

over a population of the murine macrophages takes a non-oscillatory pattern (or a monotone increasing pattern). They conjectured that the source of this stable NF-κB response is a time difference (anti-phase) between two signals reaching IKK: one signal comes directly from TLR4-MyD88 dependent signaling pathway and another comes indirectly after time-delay from TNF-R signaling pathway activated by TNFα synthesized by the activated pathway of TLR4-TRIF-IRF3. Werner et al in ref. (Werner et al 2005) presented the comparative study between the TNFα-stimulated NF-κB dynamics and the LPS-stimulated NF-κB dynamics: For TNFα stimulation, both IKK and NF-κB profiles quickly die out after their single strong peak. For LPS stimulation, however, the level of IKK and NF-κB profiles increase over two hours. They also conjectured that LPS-induced NF-κB dynamics is due to the TNFα autocrine signaling (or the effect of (+) feedback loop). Bosisio et al in ref. (Bosisio et al 2006) monitored NF-κB-bound IκBα promoter activity. The promoter activity upon TNFα stimulation shows a strong first pulse followed by very weak subsequent pulses: TNF-R pathway is quickly inactivated right after TNFα stimulation. However, the promoter activity upon LPS stimulation demonstrates the first pulse followed by the stronger second pulse: TLR4 pathway activation is maintained for a prolonged duration for the case of LPS stimulation. All the previous studies agree that LPS stimulation may maintain prolonged pathway activation and induce a rising NF-κB profile, conjecturing that TNFα autocrine signaling may contribute to this characteristic of LPS stimulation.

Computational studies of NF-κB signaling: None of previous computational work modeled TNFα autocrine signaling. Based upon accumulated knowledge of NF-κB signaling, Hoffmann *et al* built up a complex biochemical network model of IKK-NF-κB-IκB signaling (Hoffmann et al., 2002). This model was particularly corroborated with their experimental data to prove the functional roles of three isoforms of IκB: IκBα is responsible for sustained oscillatory translocation of NF-κB between cytoplasm and nucleus while IκBβ and IκBε make the NF-κB dynamics more damped (Hoffmann et al., 2002). Lipniacki et al adds a negative regulator of A20 to the previous model of Hoffmann et al with an assumption that A20 inactivates NF-κB signaling by inhibiting

IKK phosphorylation (Lee et al 2000; Lipniacki et al., 2004). They reaffirmed the experimental findings of Lee et al that the A20 knocked-out mutant shows the hyper-activity of NF-κB. Hoffmann's group later on modified their model in various minor manners, but all of their variants share the same core components with their original model (Werner et al 2005; Cheong et al; other references). While the previous modeling efforts have been mainly focused on the deterministic methods (neglecting noise), Hayot and Jayaprakash used a stochastic model of NF-κB signaling network to investigate the effect of both intrinsic and extrinsic noise on NF-κB translocation dynamics (Hayot and Jayaprakash 2006). They showed that averaging over many realizations of the stochastic NF-κB signaling system could unravel the discrepancy between oscillatory behaviors at single cells and damped-oscillation at a population of the cells. They also partially studied the effect of extrinsic noise (kinetic parameter variations) on protein dynamics. In addition, we investigated the intrinsic noise-induced oscillation of NF-κB and demonstrated its robustness against fluctuations in kinetic parameters (interpreted as extrinsic noise) (Joo et al 2008a).

Our intention to study the effect of TNFa autocrine signaling to NFKB response: As shown in Fig. 1 and discussed in details in methods section, we make a novel comprehensive NF-κB signaling network model consisting of the negative regulators of A20 and three isoforms of IκB. Moreover, we add TNFα autocrine signaling components to the comprehensive NF-κB network and investigate the effect of (+) feedback loop on NF-κB dynamics. (+) feedback loops are prevalent in biology: for example, cell-cycle, p53, and developmental mechanisms (reference). (+) feedback loop in EGFR pathway induces bistability (or hysteresis) and a combination of (+) and (-) feedback loops brings about relaxation oscillation (Kholodenko Nature Mol. Cell. Biol. 2006). In a system equipped with both (+) and (-) feedback loops, (+) feedback provides the (-) feedback loop-generated oscillation with tunable period and robustness (Tsai et al Science 2008).

LPS-stimulated NF-κB response at single cells: As TNFα-stimulated NF-κB response differ between at a population of the cells (Hoffmann et al Science 2002) and at the single

cells (Nelson et al Science 2005), LPS-stimulated NF-κB response at single cells is expected to be quite different from the previously reported data at a population of the cells (covert el al science 2005; Werner et al Science 2005; Bosisio et al EMBO 2006). The previous conjecture about the effect of (+) feedback loop on the NF-κB dynamics needs to be validated both experimentally and theoretically at the level of single cells. In addition, this effect on NF-κB dynamics is expected to depend on the dosage of stimulant.

Summary of our results: In this paper, we study NF-κB translocation dynamics in single macrophages (RAW264.7 cells) as a response to two different dosages (1 nM and 100 nM) of E. Coli Lipopolyssachride (LPS), especially the effect of TNFα autocrine signaling on NF-κB response. To make the computational model specific to LPS stimulation and inclusive of TNFα autocrine signaling, we incorporate into the computational model the signaling pathways of TLR4-MyD88-NF-κB, TNF-R, and TNFα autocrine signaling (a positive feedback loop). In addition, our computational model is designed to simulate heterogeneous NF-κB response in single cells, by taking into account the extrinsic noise-driven cell-to-cell variability. We predict and explain the dosage-dependent characteristics of NF-κB translocation dynamics at single cells by using the computational model, and corroborate and verify them by single cell fluorescence imaging experiments. First, using the computational model alone, we present that the TNFα autocrine signaling induces the bistability, resulting in two equilibrium levels of nuclear NF-κB and extracellular TNFα in a broad range of the parameter values in the TNF-R signaling pathway. The low equilibrium level of nuclear NF-κB is four orders of magnitude times smaller than the high level. Assuming that the signaling system can have either one of two equilibrium levels of nuclear NF-κB before LPS stimulation, we demonstrate that only the system with the low level of nuclear NF-κB exhibits noticeable NF-κB response to the low (1 nM) dosage stimulation and the system with the high level is not responsive at all. For the high (100 nM) dosage stimulation, however, the system with either high or low level of nuclear NF-κB induces a similar dynamical response. Second, both the experiments and the computations show

that the LPS stimulation induces three heterogeneous dynamic patterns of NF-κB translocation (single-peaked, damped oscillatory, and rising patterns) and their distribution is dosage-dependent. The high dosage (100 nM) stimulation induces more homogeneous dynamic patterns than the low dosage (1 nM). Third, both experiments and computations reveal that, for the high (100 nM) dosage stimulation, both the majority and their population average of the nuclear NF-κB profiles at the level of single cells are highly (under-damped) oscillatory, which is in contrast to the previous findings of Covert et al. On the contrary, the low (1 nM) dosage stimulation induces non-oscillatory dynamics (a rising pattern) of NF-κB in the population average and almost a half of the cells. Fourth, by using only the computational model, we validate the conjecture: the TNFα autocrine signaling is responsible for a rising pattern of NF-κB. When stimulated by the low dosage (1nM), the TNFα knocked-out computational model doesn't give rise to the rising pattern. Lastly, we use the real time quantitative PCR of A20 mRNA and IκBα mRNA to demonstrate the correlation between the dosage-dependent NF-κB translocation dynamics and the expression profiles of NF-κB target genes.

II. Results

A. Short summary: To unravel the underlying mechanisms of how the low and the high LPS dosages induce different dynamic response of NF-κB at the level of single cells, we employ the computer model to generate testable predictions of the characteristics of NF-κB dynamic response and verify them by single cell fluorescence imaging.

B. Construction of a computational model to include TNF autocrine signaling: One of the NF-κB target genes is TNFα. A newly synthesized TNFα followed by NF-κB nuclear localization is released extracellularly and activates TNFα pathway. This results in the activation of canonical NF-κB signaling pathway and thus forms (+) feedback loop. A minimally required set of the activated pathways to model LPS-stimulated NF-κB dynamics should include TLR4-MyD88 dependent pathway, canonical NF-κB pathway, TNFα autocrine pathway, and TNF-R pathway. The computational model

network (detailed in method section) consists of TNFα autocrine signaling (positive feedback loop) as well as (-) feedback loops by A20 and IκB isoforms. The NF-κB dynamics on this network is determined by the interplay between (+) and (-) feedback loops. The NF-κB in the delayed (-) feedback loop oscillates in a restricted parameter space (Sneppen 2007; Joo et al 2008a) and It is expected that TNFα (+) feedback loop can make this oscillation amplified and robust (Novak and Tyson 2008).

C. Computational model predicts that TNFα autocrine signaling induces the bistability and two equilibrium levels of nuclear NF-κB before LPS stimulation: TNFα autocrine signaling, (+) feedback loop, gives rise to the bistability of NFKB response. For the analysis of the bistability, we consider only the TNF-R, canonical NF-κB, and TNFα autocrine signaling pathways as shown in Fig. 1A. For the simplicity of our analysis, we suppose that NF-κB nuclear localization leads to the mRNA and protein synthesis of TNFα followed by the export of intracellular TNFα proteins without any additional regulatory mechanisms (reference from Bryan Carson). In the absence of external stimulus, nuclear NF-κB level will ever increase if there exists only a (+) feedback loop. But, because our model system composes of both (+) and (-) feedback loops, their interplay stabilizes the system. Moreover, (+) feedback loop introduces its well-known characteristics into the (-) feedback loop controlled system: bistability and amplification of the (-) feedback-driven behavior such as oscillation. To demonstrate the existence of the bistability in our model system, we choose one of the kinetic reactions in TNF-R pathway, the activation of IKK by IKKKa as shown in Fig. 1A, and vary its rate to simulate the varying strength of (+) feedback loop. Both steady state levels of extracellular TNFα and nuclear NF-κB depend on the strength of (+) feedback loop. In fact, the extracellular level of TNFα is inter-related with the nuclear level of NF-κB because the nuclear NF-κB regulates the synthesis of TNFα. As presented in Supporting Fig. 1, as the strength of (+) feedback increases, both stationary levels of extracellular TNFα and nuclear NF-κB discontinuously jump from a low to a high value sharply at a strength of (+) feedback. Likewise, as this strength decreases, both steady state responses discontinuously drop down from a high to a low value at the lower strength of (+)

feedback. This discontinuity is a signature of the bistability, but the bistable range of (+) feedback strength is too small to be recognizable in Supporting Fig. 1. Moreover, the levels of nuclear NF-κB and TNFα remains almost invariant across the four orders of magnitude of the change in (+) feedback loop strength except at the discontinuity: For a weak (+) feedback, the equilibrium level of nuclear NF-κB is in order of 0.001 nM while it is in order of 10 nM for a strong (+) feedback. This leads us to conjecture that the canonical NF-κB signaling system supplemented/amplified by TNFα autocrine signaling can have either low or high equilibrium level of nuclear NF-κB and its response to external stimulus can be dramatically different, depending on which strength of (+) feedback the signaling system possesses, or in the other words, which equilibrium level of nuclear NF-κB the system has before the stimulation. This possibility is computationally explored and presented at a later section, but remains subject to future experimental validation.

D. Computational model simulates extrinsic noise-driven cell-to-cell variability and heterogeneous NF-κB response in single cells: We use a statistical ensemble analysis to simulate the extrinsic noise and its effect on NF-κB dynamics in the single cells (reference: Joo et al 2008b). To say about the analysis briefly, extrinsic noise is modeled as fluctuations in the network parameters such as the copy number of key proteins and kinetic rate constants. A population of the single cells is represented by an ensemble of 1000 replicates of the signaling system and the network parameters of individual replicate are sampled from the uniform distribution defined uniquely by both the reference values of the kinetic rate constants and the universal interval size χ. For this paper, the heterogeneity measure is set to χ=30%. This statistical ensemble analysis generates heterogeneous NF-κB dynamics collected from the ensemble of 1000 replicate systems as shown in Fig. 2.

E. Computational model predicts dosage-dependent distribution of dynamic patterns and the lower dosage induces the more heterogeneous dynamic patterns: Each NF-κB temporal profile is different from one replicate to anther. Individual NF-κB

profiles, however, can be simply classified into one of four dynamic patterns: under-damped oscillation, sustained oscillation, single-peaked pattern, or hyperbolic pattern. We stimulate the ensemble of the signaling system with two different stimulant strengths, classify the resulting profiles of NF-κB dynamics, and measure the percent of the profiles belonging to the class of a dynamic pattern for each dosage. High dosage stimulation (LPS=100 nM) leads to a skew distribution of the dynamic patterns: a majority of the nuclear NF-κB profiles are oscillatory patterns. But, low dosage stimulation (LPS=1 nM) induces the evenly distributed dynamic patterns and the more heterogeneous distribution of the dynamic patterns. Thus, extrinsic noise drives cell-to-cell variability in NF-κB response and high dosage stimulation suppresses this variability.

F. Single cell fluorescence imaging enables us to monitor NF-κB **translocation patterns in single cells in real time:** As discussed in method section, we tag the RelA protein with green fluorescent protein (GFP) and monitor the RelA translocation patterns in the single cells in real time for four hours after LPS stimulation. The time-varying nuclear GFP intensity per cell is quantified and normalized by the maximum nuclear GFP intensity from a single movie shot. (We present only nuclear GFP intensity because the cytoplasmic GFP intensity remains non-dynamical and invariant.) We take at least two to three movie replicates for each dosage and confirm that for the same dosage stimulation, the GFP-RelA dynamics is consistent between replicates. In Fig. 3A and 3B, about 40 individual time-series are presented for each of two different E. Coli LPS dosage stimulations, 1 nM and 100 nM. Each curve represents the normalized nuclear GFP-RelA intensity in an individual cell. We take the average nuclear GFP-RelA intensity over those 40 cells captured in the field of microscopic observation. This average corresponds to a population level behavior, though the number of the cells is quite small compared to the millions of the cells in typical experimental measurements.

G. Single cell fluorescence imaging data verify dosage-dependent cell-to-cell variability in GFP-RelA dynamic response: Low dosage induces more heterogeneous response than high dosage. We calculate the standard deviation of nuclear GFP-RelA temporal profiles away from their average for low and high LPS dosage stimulations. The standard deviation decreases in time *(until 160 minutes and then*

begins to increase at later times) for low LPS dosage stimulation while it increases for high LPS dosage stimulation as shown in the top panels in Fig. 3A and 3B. In addition, each individual curve is classified into one of three dynamic patterns: under-damped oscillation, rising pattern, and single-peaked pattern. This classification shows that the distribution of the dynamic patterns of GFP-RelA protein is dependent on the LPS dosage.

Low dosage induces evenly distributed dynamic patterns while when stimulated by high LPS dosage, about 75% of cells exhibit a single dynamic pattern, damped-oscillatory response. So we experimentally verify the model prediction that low dosage induces more heterogeneous response in single cells than high dosage does. The above observation can be quantified by entropy measure, defined as $H = -\sum_i P_i \log P_i$ where P_i is a fraction of *i*th dynamic pattern, which is a good indicator of heterogeneity of the dynamic patterns. The entropy amounts to $H=0.33$ for high dosage and $H=0.46$ for low dosage. The higher entropy for lower dosage indicates that the dynamic patterns are more disordered and heterogeneous for lower dosage stimulation.

H. Computational model predicts that high dosage induces highly oscillatory response: The computational model assumes that the LPS stimulation activates first TLR4-MyD88 dependent pathway and subsequently the (+) feedback loop consisting of canonical NF-κB signaling, TNFα autocrine signaling, and TNF-R signaling pathway. Before the LPS stimulation, the signaling system can reach either one of two equilibrium levels of nuclear NF-κB, a low level for a weak (+) feedback and a high level for a strong (+) feedback. We find that, upon high dosage stimulation (LPS=100 nM) to TLR4-MyD88 dependent pathway, both weak and strong (+) feedback strengths induce the similar NF-κB response. As shown in Fig. 3A, high dosage stimulation (LPS=100 nM) induces a highly (under-damped) oscillatory pattern in both a majority of the ensemble and their ensemble average regardless of the strength of (+) feedback. In other words, the ensemble consisting of the copy systems with different (+) feedback strengths and the resulting equilibrium levels of nuclear NF-κB exhibits the fairly homogenous distribution of the NF-κB dynamic response, which shoots up in less than one hour, followed by the

subsequent pulses with decreasing peak amplitudes. The underlying mechanism of the high dosage-stimulated NF-κB behavior indifferent of (+) feedback strength is rather simple. The high dosage stimulation (LPS=100 nM) is strong enough to override whatever may be the pre-existing condition of the ensemble. The system with the high equilibrium level of nuclear NF-κB, i.e., the one with strong (+) feedback, also have the high level of negative regulators of A20 and IκB isoforms, which readily suppresses the nuclear translocation of NF-κB. On the one hand, if we were to observe the noticeable dynamic response of NF-κB, the signal strength should be high enough to override the pre-existing strong negative regulation. On the other hand, we can expect that the sufficiently low dosage stimulation can induce quite a different NF-κB response in the ensemble of the systems with weak (+) feedback strength than that with strong (+) feedback strength.

I. Computational model predicts that low LPS dosage induces a rising pattern of nuclear NF-κB: Upon low dosage stimulation (LPS=1 nM), the ensemble with strong (+) feedback strength exhibits totally different NF-κB dynamic response from the ensemble with weak (+) feedback strength. As shown in Fig. 2, the former ensemble barely exhibits any noticeable change in nuclear NF-κB level while the latter ensemble shows the substantial increase of nuclear NF-κB level. In contrast to the oscillatory NF-κB response from high dosage stimulation, the low dosage induces a non-oscillatory rising pattern of nuclear NF-κB but only in the ensemble with weak (+) feedback strength. Both the majority of the individual profiles and their average show this rising pattern: The second peak of nuclear NF-κB profile is as high as the first peak and the subsequent peaks increase in time until the nuclear NF-κB level reaches its equilibrium level determined by the interplay of (-) and (+) feedbacks. The rising pattern of nuclear NF-κB follows the rising profile of extracellular TNFα in Fig. 2B.

J. Computational model validates the conjecture that the TNFα autocrine signaling is responsible for low dosage-induced rising pattern: We demonstrate that the underlying mechanism of this low dosage-induced rising pattern originates from TNFα

autocrine signaling. To prove our assertion, we employ a standard biology technique of knocking out TNFα and comparing two NF-κB profiles, one from the wild type and another from the mutant. When TNFα is knocked out, the rising trend of nuclear NF-κB evidently present in the wild type disappears at once as shown in Fig. 2B. This *in silico* knocked-out experiment partially confirms the undeniable effect of TNFα (+) feedback loop on the rising pattern of nuclear NF-κB upon low dosage stimulation.

K. Single cell imaging data verify that high LPS dosage induces highly oscillatory NF-κB response while low dosage induces a rising pattern: As shown in Fig. 3A, upon high (100 nM) E. Coli LPS dosage stimulation, the majority of GFP-RelA profiles and their average take an under-damped oscillatory pattern. The most common characteristic of the individual GFP-RelA responses is the strong first peak followed by the weak second peak. As expected, the individual profiles of nuclear GFP-RelA in the single cells are not at all similar to the monotone-increasing nuclear NF-κB profile at the population level reported in ref. (Covert et al 2005). On the contrary, the low (1 nM) E. Coli LPS dosage stimulation induces a rising response of nuclear NF-κB in both a majority of GFP-RelA profiles and their average as shown in Fig. 3B. A characteristic of this rising pattern is the increasing peak amplitude of GFP-RelA: the large second peak follows the small first peak.

L. Biological relevance of NF-κB dynamic response is partially established by correlation between nuclear NF-κB profile and mRNA profiles of IκBα and A20: We investigate the relationship between the NF-κB dynamic response and the expression of NF-κB target genes. For this purpose, we use the quantitative RT-PCR to measure the induction level of IκBα mRNA, A20 mRNA, and RelA mRNA at multiple time points with and without stimulation with two different LPS dosages. The mRNA profiles are presented in Fig. 3C for 100 nM E. Coli LPS and in Fig. 3D for 1 nM E.Coli LPS. Without stimulation, the induction levels of all three mRNAs remain close to the level of house keeping genes with small fluctuations. In regard to the dynamic pattern, mRNA profiles show LPS-dosage independent behavior. For both 1 nM and 100 nM LPS

stimulations, two distinctive peaks are observed at the time points of 45 and 120 minutes, for both A20 mRNA and IκBα mRNA and the second peak is substantially smaller than the first peak. Upon high LPS dosage stimulation, the mRNA profile in Fig. 3C is nicely correlated with the NF-κB response in Fig. 2A. The timing of the first and the second peaks of the mRNA profiles of A20 and IκBα correspond to the peaks of the nuclear NF-κB, taking into consideration of about half an hour delay for mRNA synthesis. But, for low LPS dosage stimulation, the rising pattern of nuclear NF-κB in Fig. 2B is not correlated with the mRNA profile in Fig. 3D: the source of the second peak of mRNA profile cannot be identified from the rising pattern of nuclear NF-κB profile whose second peak occurs one hour after the occurrence of the second peak of mRNA. *(This paradox seems to stem from our problematic comparison of the single cell level NF-κB data with the population level mRNA data as well as their quite different temporal resolution (two minutes for NF-κB and half an hour for mRNA)* But, the maximum induction level of A20 and IκBα depends on the LPS dosage. As shown in Fig. 3C and 3D, the first peaks of A20 and IκBα mRNA profiles are substantially higher for the larger LPS dosage. In addition, RelA mRNA induction level is hardly changed throughout the course of stimulation except some fluctuations. This invariant RelA level confirms our assumption of a conservation of total NF-κB copy number.

III. Discussion

A. **Significance of heterogeneous protein dynamics at the single cells:** We demonstrate that the NF-κB protein dynamics in the identical cells under the same environmental conditions take not a uniform dynamic pattern, but a few well-defined heterogeneous dynamic patterns. This non-uniform cellular behavior among the individual cells cannot be easily derived from the population level measurements, and dramatically different from the previous assumptions about the biological dynamics, i.e., its robustness and uniformity. Two points that are worth to mention are the source of this cell-to-cell variability in protein dynamics and its physiological consequence. Regarding the source, it remains still open what can derive this large cell-to-cell variability. Intrinsic

noise, defined as randomness of the collisions between biochemical species, alone cannot explain this heterogeneity because the observed dynamic patterns are much more heterogeneous than what intrinsic noise can generate (Hayot and Jayaprakash 2004; Joo et al 2008b). The other source is termed as extrinsic noise that originates from the outside of the signaling system through the coupling of the system with the fluctuating environmental conditions and other noisy signaling and/or regulatory modules. Extrinsic noise affects all genes simultaneously and can be modeled as fluctuations in kinetic rate constants that influence fluctuations in the copy number of key proteins. Assuming that this extrinsic noise can certainly generate heterogeneous protein dynamics (Paulsson 2004; Joo et al 2008a and 2008b), we proposed a novel statistical ensemble analysis to deal with the extrinsic noise-driven heterogeneity in ref. (Joo et al 2008b). In this paper, we validate our proposal by demonstrating that computationally simulated extrinsic noise can reproduce the experimentally observed heterogeneous dynamics of NF-κB. Concerning physiological effect of extrinsic noise, this cell-to-cell variability in protein dynamics significantly affects the cell-fate decision and can be a prominent source of drug resistance (reference). For example, Alon's group exhibited the heterogeneous dynamics of a few proteins that are related to drug resistance (Uri Alon Science 2008). Because NF-κB plays an important role in not only so many biological functions such as apoptosis, inflammation, immune cell differentiation but also cancer angiogenesis and chemotherapy, the observed large cell-to-cell variability in NF-κB translocation dynamics should significantly affect the normal and the abnormal cellular functions. This connection needs to be investigated in the future.

B. LPS induced NF-κB **response at a population level vs. at the level of single cells:** Some of our results at the single cell level are in contrast to the previous observations at the population level (Covert et al 2005; Werner et al 2005). The difference between ours and the previous studies arises from two sources: (1) the noise-driven dynamics in the single cells and (2) the LPS dosage. Both Covert et al and Werner et al reported that, when the single murine macrophages are stimulated by LPS, the nuclear NF-κB profile averaged over a population of the cells takes a monotone increasing pattern. They used two low LPS dosages, 0.1 μg/ml (0.2 nM) and with 0.5 μg/ml (1 nM). Consequently,

their nuclear NF-κB profile resembles the rising pattern of nuclear NF-κB profile, a characteristic dynamic profile of LPS 1 nM stimulation, as shown in Fig. 3B. Based on the high LPS dosage stimulation data from the single cells, homogeneous and oscillatory NF-κB dynamics, we speculate that the nuclear NF-κB profiles averaged over a population of the cells will show oscillatory behavior when stimulated by high enough LPS dosage.

C. Significance of dosage-dependent protein dynamics: Our studies indicate that the dosage of stimulant plays a significant role in the activation of inflammatory response and/or cell apoptosis. We show that stimulant dosage is correlated with the nucleo-cytoplasmic shuttling dynamics of a transcriptional protein NF-κB, which is in turn related with its target gene expression profile. It has been taken granted that dosage has a threshold behavior, i.e., response can occur only if the dosage is above the threshold value. But, in our paper, we relate low/high LPS dosage not with on/off response, but with different protein dynamics. We emphasize that each pattern of protein dynamics must have message/information.

D. Analysis of network motif consisting of both (+) and (-) feedback loops: We admit that our computational analysis is impartial and incomplete. The network is complex, large, and consists of many unknown parameters. Most of our conclusions are drawn from numerical simulations of the network only in a very restricted parameter space. It also lacks the understanding of the potential dynamics that this network can give rise to. One possible solution to overcome this shortcoming is to reduce the complexity of the model and analyze the dynamics in the reduced network. The network shown in Fig. 1A can be reduced to a simple network motif consisting of both (+) and (-) feedback loops: IκBα inhibits nuclear NF-κB, nuclear NFKB inhibits IκBα through TNFα autocrine signaling, NF-κB activates mRNA IκBα which in turn activates protein IκBα. This regulatory motif is equivalent to the “incoherently amplified negative feedback loop” (Novak and Tyson 2008). This delayed (-) feedback loop is known to oscillate in its own right and (+) feedback loop makes the oscillation amplified, robust, and tunable. (Novak and Tyson 2008; Tsai et al 2008). In addition to those already known mechanisms, it is

desirable to investigate (1) how its dynamics (or oscillatory behavior) depends on the LPS dosage at the different strength of (+) and (-) feedback loops, (2) how its dynamics depends on the time-delay imposed on (+) and (-) feedback loops, (3) the effect of both intrinsic and extrinsic noise on the NF-κB dynamics in this reduced network, and (4) how extracellular TNFα contributes to homogenization and/or synchronization of the NF-κB dynamics at a population of the single cells.

IV. Methods

1. Computational network model: A computational model consists of three modules, one for the canonical NF-κB signaling pathway shown in Fig. 2B, one for the TNF-R signaling pathway as shown in Fig. 2A, and one for the Toll like receptor 4 (TLR4-MyD88-dependent) signaling pathway as shown in Fig. 2A. The TNF-R and TLR4 signaling pathways converge to IKK, placed on the entrance of the canonical NF-κB signaling pathway. *E. Coli* LPS stimulates TLR4-MyD88-dependent signaling pathway. The signal propagates through this pathway and activates the canonical NF-κB pathway. Then the activated NF-κB translocates into the nucleus and initiates the transcription of NF-κB target genes. The newly synthesized TNFα stimulates TNF-R signaling pathway and the NF-κB signaling pathway, forming a positive feedback loop. Both A20 and IκB isoforms are negative regulators and form multiple negative feedback loops.

1a. TNF receptor signaling pathway: As shown in Fig. 2A, TNF receptors (TNFR) become activated to be TNFR*, when bound by extracellular TNFα proteins. TNFR* can be reversed to TNFR when unbound. Activated TNF receptors (TNFR*) transform inactive IKK kinase into activated IKK kinase (IKKKa), which in turn activates neutral IκB kinase (IKKn) into activated IKK (IKKa). This initiates the canonical NF-κB signaling. The above simplified description of TNF receptor signaling pathway was first adopted by Cho et al (reference), mimicking the MAPK signal cascade. This model is used by Lipniacki *et al* in their stochastic model (reference).

1b. TLR4-MyD88-dependent pathway: As shown in Fig. 2A, activation and inactivation of TLR4 occurs when LPS is bound or unbound to the receptors, respectively. Once LPS is bound to TLR4, the signal passes through a linear chain of the MyD88-dependent pathway and TAK can induce the activation of IKK (IKKa), activating the canonical NF-κB signaling pathway. The linear chain model of TLR4 signaling pathway was first used by Salvarjoo (FEBS Lett). This linear chain of multiple proteins is greatly simplified to a single super node by Covert et al. The only difference here is that we impose the conservation of the TLR4 mass in time: the sum of TLR4 and TLR4* should equal to a constant.

1c. Canonical NF-κB signaling pathway (IKK-NF-κB-IκB-A20 signaling pathway): The NF-κB signaling pathway shown in Fig. 2B represents a new comprehensive model, i.e., the up-to-dated network comprising IκB kinase (IKK), NF-κB, both negative regulators of A20 and IκB isoforms (IκBα, IκBβ, IκBε), and the protein complexes formed by two or three of the constituents (Hoffmann et al., 2002; Lipniacki et al., 2004; Lipniacki et al., 2006; Cheong et al., 2006; Covert et al., 2005; Barken et al., 2005; Kearns et al., 2006; Nelson et al., 2005; Werner et al., 2005). This signaling pathway model also includes mRNA and protein syntheses of A20 and IκB isoforms. The network consists of 70 kinetic rate constants and one initial concentration of NF-κB, whose values are taken from the literature (Lipniaki et al 2004; Werner et al., 2005).

1d. TNFα autocrine signaling: As shown in Fig. 2A, TNFα-mediated autocrine signaling is modeled as follows: the synthesis rate of mRNA TNFα (TNFt) depends on a saturating function of [NF-κBn] just as A20 mRNA and IKB mRNA do. TNFt is then translated to intracellular TNFα protein (TNFi). TNFi diffuses to extracellular space, becoming extracellular TNFα (TNFe), which is bound to TNF-R, making it activated TNF-R*.

2. Parameterization of the computational model with experimental data: The nominal values of most of the kinetic rate constants of the canonical NF-κB signaling pathway are taken from the literature (Lipniaki et al 2004; Werner et al., 2005). The synthesis rates and the degradation rates of A20 mRNA and IκBα mRNA are calibrated to reproduce the induction levels of the Q-PCR generated A20 mRNA and IκBα mRNA. The most significantly correlated parameter with NF-κB translocation dynamics is total NF-κB concentration and its value is taken from the literature (reference). The volume ratio of cytoplasm to nucleus is the second most significantly correlated parameter with NF-κB response and its average and variation are measured from ten RAW 264.7 murine macrophage-like cells by Hyper-spectral imaging technique (reference). Other available experimental data, e.g., both the IKK temporal profiles and the IκBα promoter-bound NF-κB profiles resulting from stimulation by either TNFα or LPS, are used as the qualitative patterns that our computational model results should reproduce (Werner et al; Covert et al; (Bosisio et al).

3. Numerical simulation of the computational network model: The network in Fig. 2A is translated to a system of ordinary differential equations (ODE). These equations are simulated with the initial values of total NF-κB concentration and zero concentrations of all the other biochemical species. We simulate the ODE system until it reaches its equilibrium (33 hours) and then constantly stimulate the system and measure/record the temporal profiles of various biochemical species.

5. EGFP-RelA reporter construct: The $p_{\beta Actin}$-EGFP-RelA construct was derived from pECFP-F-RelA, a kind gift from Dr. Allan Brasier (University of Texas Medical Branch). ECFP was replaced with EGFP between the Age1 and BsrG1 sites, and the cytomegalovirus (CMV) promoter was replaced with a minimal 106bp human βActin promoter (1) cloned between the Ase1 and Nhe1 sites to reduce average expression levels. The plasmid pBA-GFP-RelA was linearized and used to transfect RAW264.7 murine macrophage-like cells (ATCC) by Nucleofection (Amaxa Biosystems).

Transfected cells were grown for 12 days in the presence of G418, and a clone stably expressing GFP-RelA was isolated and named RG16.

6. RNA isolation and Quantitative RT-PCR: Total RNA is isolated from either RAW264.7 or RG16 murine macrophages stimulated with 0nM, 1nM or 100nM *E.coli* LPS at the following timepoints: 0, 30, 45, 60, 90, 120, 180, and 240min. The total RNA isolation is repeated on subsequent days to obtain two biological replicas for each experimental condition. Total RNA extraction is performed using Qiashredder, RNAeasy, and DNase on-column kits from Qiagen. RNA integrity is tested using a Bioanalyzer. Relative abundances of A20 and IκBα mRNA are measured using TaqMan® qRT-PCR with 50ng RNA per reaction. Probes, primers, and one step reagents are purchased from ABI and reactions are run in triplicate using an ABI 7500 instrument. Abundances are calculated relative to eukaryotic 18S rRNA using SDS v1.3 software (ABI).

7. Cell Culture, Transfection, and Imaging: RAW 264.7 cells are grown in DMEM supplemented with 10% fetal bovine serum, 2mM L-glutamine, 1mM sodium pyruvate, 1x MEM nonessential amino acids, 20mM HEPES, 100 I.U./ml penicillin, and 100µg/ml streptomycin. For microscopy, $3x10^5$ cells are plated in 35mm glass coverslip bottom dishes 18-24 hours prior to stimulation and imaging. Dishes are placed in a microscope stage-top humidified microincubator at 37°C with continuous flow 5% CO_2 in air. Stimulation is initiated by addition of growth medium containing lipopolysaccharide. Images are collected every 2-10 minutes for 4-6 hours.

V. Reference

[1] Elowitz MB, Levine AJ, Siggia ED, Swain PS (2002) Stochastic gene expression in a single cell. Science 297: 1183-1186.
[2] Swain PS, Elowitz MB, Siggia, ED (2002) Intrinsic and extrinsic contributions to stochasticity in gene expression. Proc Natl Acad Sci 99: 12795-12800.
[3] Blake WJ, Karn M, Cantor CR, Collins JJ (2003) Noise in eukaryotic gene expression. Science 422: 633-637.

[4] Raser JM, O'Shea EK (2005) Noise in gene expression: origins, consequences, and control. Science 309: 2010-2013.
[5] Raser JM, O'Shea EK (2004) Control of stochasticity in eukaryotic gene expression. Science 304: 1811-1814.
[6] Rosenfeld N, Young JW, Alon U, Swain SS, Elowitz MB (2005) Gene regulation at the single-cell level. Science 307: 1962-1965.
[7] Raj A, Perskin CS, Tranchina D, Vargas DY, Tyagi S (2006) Stochastic mRNA synthesis in mammalian cells. PLoS Biology 4: e309.
[8] McAdams HH, Shapiro L (1995) Circuit simulation of genetic networks. Science 269: 650-656.
[9] Arkin A, Ross J, McAdams, HH (1998) Stochastic kinetic analysis of developmental pathways bifurcation in phage λ-infected E. Coli cells. Genetics 149; 1633-1648.
[10] Thattai M, van Oudenaarden A (2001) Intrinsic noise in gene regulatory networks. Proc Natl Acad Sci 98: 8614-8619.
[11] Ozbudak EM, Thattai M, Kurtser I, Grossman AD, van Ouderaarden A (2002) Regulation of noise in the expression of a single gene. Nat Genetics 31: 69-73.
[12] Pedraza JM, van Oudenaarden A (2005) Noise propagation in gene networks. Science 307: 1965-1969.
[13] Shen-Orr SS, Milo R, Mangan S, Alon U (2002) Network motifs in the transcriptional regulation network of Escherichia coli. Nat Genet 31: 64-68.
[14] Yeger-Lotem E, Sattath S, Kashtan N, Itzkovitz S, Milo R, Pinter RY, Alon U, Margalit H (2004) Network motifs in integrated cellular networks of transcription regulation and protein-protein interaction. Proc Natl Acad Sci U S A 101: 5934–5939.
[15] Tyson JJ, Chen KC, Novak B (2003) Sniffers, buzzers, toggles ad blinkers: dynamics of regulatory and signaling pathways in the cell. Curr Opinion 15: 221-231.
[16] Lahav G, Rosenfeld N, Sigal A, Geva-Zatorsky N, Levine AJ, Elowitz MB, Alon U (2004) Dynamics of the p53-Mdm2 feedback loop in individual cells. Nat. Genet. 36: 147-150.
[17] Hirata H, Yoshiura S, Ohtsuka T, Bessho Y, Harada T, Yoshikawa K, Kageyama R (2000) Oscillatory expression of the bHLH factor Hes1 regulated by a negative feedback loop. Science 298: 840-843.

[18] Yoshiura S, Ohtsuka T, Takenaka Y, Nagahara H, Yoshikawa K, Kageyama R (2007) Ultradian oscillations of Stat, Smad, and Hes1 expression in response to serum. Proc Natl Acad Sci U S A. 104:11292-11297.
[19] Hoffmann A, Levchenko A, Scott ML, Baltimore D (2002) The IκB-NF-κB signaling module: temporal control and selective gene activation. Science 298: 1241-1245.
[20] Nelson DE, Ihekwaba AEC, Elliott M, Johnson JR, Gibney CA, Foreman BE, Nelson G, See V, Horton CA, Spiller DG, Edwards SW, McDowell HP, Unitt JF, Sullivan E, Grimley R, Benson N, Broomhead D, Kell DB, White MRH (2004) Oscillations in NF-κB signaling control the dynamics of gene expression. Science 306: 704-708.
[21] Geva-Zatorsky N, Rosenfeld N, Itzkovitz S, Milo R, Sigal A. Dekel E, Yarnitzky T, Liron Y, Polak P, Lahav G, Alon U (2006) Oscillations and variability in the p53 system. Molecular Systems Biology.
[22] Lahav G (2004) The strength of indecisiveness: oscillatory behavior for better cell fate determination. Science STKE 264: pe55-pe58.
[23] Barken D, Wang CJ, Kearns J, Cheong R, Hoffmann A, Levchenko A (2005) Comment on ``oscillations in NF-κB signaling control the dynamics of gene expression". Science 308: 52a.
[24] Nelson DE, Horton CA, See V, Johnson JR, Nelson G, Spiller DG (2005) Response to comments on ``oscillations in NF-κB signaling control the dynamics of gene expression". Science 308: 52b.
[25] Tian B, Nowak DE, Brasier AR (2005) A TNF-induced gene expression program under oscillatory NF-κB control. BMC Genomics 6: 137-155.
[26] Li Q, Verma, IM (2002) NF-κB regulation in the immune system. Nat. Rev. Immunol. 2: 725.
[27] Hoffmann A, Baltimore D (2006) Circuitry of nuclear factor κB signaling. Immunological Reviews 210: 171-186.
[28] Verma IM, Stevenson J (1997) IκB kinase: beginning, not the end. Proc Natl Acad Sci U S A 94: 11758-11760.

[29] Lee EG, Boone DL, Chai S, Libby SL, Chien M, Lodolce JP, Ma A. (2000) Failure to regulate TNF-induced NF-κB and cell death responses in A20-deficient mice. Science 289: 2350-2354.
[30] Lipniacki T, Paszek P, Brasier AR, Luxon BA, Kimmel M (2004) Mathematical model of NF-κB regulatory module. J Theor Biol 228: 195-215.
[31] Saccani S, Pantano S, Natoli G (2001) Two waves of nuclear factor κB recruitment to target promoters. J Exp Med 193: 1351-1359.
[32] Saccani S, Pantano S, Natoli G (2002) p38-Dependent marking of inflammatory genes for increased NF-kappa B recruitment. Nat Immunol 3: 69-75.
[33] Natoli G, Saccani S, Bosisio D, Marazzi I (2005) Interactions of NF-κB with chromatin: the art of being at the right place at the right time. Nat Immunol 6: 439-445.
[34] Vanden Berghe W, Ndlovu MN, Hoya-Arias R, Dijsselbloem N, Gerlo S, Haegeman G (2006) Keeping up NF-κB appearances: epigenetic control of immunity or inflammation-triggered epigenetics. Biochem Pharmacol 72: 1114-1131.
[35] Werner SL, Barken D, Hoffmann A (2005) Stimulus specificity of gene expression programs determined by temporal control of IKK activity. Science 309: 1857-1861.
[36] Kearns JD, Basak S, Werner SL, Huang CS, Hoffmann A (2006) IκBε provides negative feedback to control NF-κB oscillations, signaling dynamics, and inflammatory gene expression. J. Chem. Biol. 173: 659-664.
[37] Krishna S, Jensen MH, Sneppen K (2006) Minimal model of spiky oscillations in NF-κB signaling. Proc. Natl. Acad. Sci. U S A 103: 10840-10845.
[38] Lipniacki T, Paszek P, Brasier AR, Luxon BA, Kimmel M (2006) Stochastic regulation in early immune response. Biophys J 90: 725-742.
[39] Hayot F, Jayaprakash C (2006) NF-κB oscillations and cell-to-cell variability. J. Theor. Biol. 240: 583-591.
[40] Joo J, Plimpton S, Faulon, JL (2008a). Noise-induced oscillatory shuttling of NF-κB in a two compartment IKK-NF-κB-IκB-A20 signaling model. To be published.
[40] Joo J, Plimpton S, Faulon, JL (2008b). Novel statistical ensemble analysis for simulating heterogeneous response in NF-kB signaling network. To be published.
[41] Covert MW, Leung TH, Gaston JE, Baltimore D (2005) Achieving stability of lipopolysaccharide-induced NF-κB activation. Science 309: 1854-1857.

[42] Carlotti F, Chapman R, Dower SW, and Qwarnstorm EE (1999) Activation of nuclear factor *κB* in single living cells. J. Biolol. Chem. 274: 37941-37949.
[43] Liew FY, Xu D, Brint EK, O'Neil AJ (2005) Negative regulation of toll-like receptor-mediated immune responses. Nat. Rev. Immunol. 5: 446-458.
[44] Cheong R, Bergmann A, Werner S, Regal J, Hoffmann A, Levchenko A (2006) Transient IκB kinase activity mediates temporal NF-κB dynamics in response to a wide range of tumor necrosis factor-α doses. J. Biol. Chem. 281: 2945-2950.
[45] Balaban NQ, Merrin J, Chait R, Kowalik L, Leibler S (2004) Bacterial persistence as a phenotypic switch. Science 305: 1622-1625.
[46] Avery SV (2006) Microbial cell individuality and the underlying sources of heterogeneity. Nat. Rev. Microbiol. 4: 577-587.
[47] Dudnau D, Losick R (2006) Bistability in bacteria. Mol. Microbiol. 61: 564-572.
[48] Kussell E, Kishony R, Balaban NQ, Leibler S (2005) Bacterial persistence: a model of survival in changing environments. Genetics 169: 1807-1814.
[49] Monk NAM (2003) Oscillatory expression of Hes1, P53, and NF-κB driven by transcriptional time delays. Curr Biol 13: 1409-1413.
[50] Swiler LP, Wyss GD (2004) A user's guide to Sandia's Latin Hypercube smapling software: LHS UNIX library/standalone version. SAND Report: 2004-2439.
[51] Quitschke, W. W., Z. Y. Lin, et al. (1989). "The beta actin promoter. High levels of transcription depend upon a CCAAT binding factor." J Biol Chem **264**(16): 9539-46.
[52] Tsai TY, Choi YS, Ma W, Pomerening JR, Tang C, Ferrell JE Jr. (2008) "Robust, tunable biological oscillations from interlinked positive and negative feedback loops" Science 321: 126-9.

Figure Caption:

Figure 1: Extended network model of TNF-R, canonical NF-kappaB, and TLR4-MyD88 dependent signaling pathway. In (A) the activation of TLR4-MyD88-dependent pathway by LPS leads to the activation of a canonical NF-kappaB signaling pathway, which in turn activates the TNF-R pathway through TNF autocrine signaling. (B) shows IKK-IkappaB-NF-kappaB-A20 signaling pathway model.

Figure 2: Computational model prediction of the distribution of individual temporal profiles of the key biochemical species and their averages (thick solid lines) upon large dosage stimulation (LPS=100 nM) for (A) and small stimulation (LPS=1 nM) for (B). Top panel: nuclear NF-kappaB concentration. Bottom panel: extracellular TNFalpha concentration.

Figure 3: Single cell fluorescence imaging data for the profiles of nuclear GFP-RelA protein and mRNA A20 and mRNA IkappaB alpha. (A) and (C) are for 100 nM dosage of LPS stimulation while (B) and (D) are for 1 nM LPS dosage. In (A) and (B), top panels present both the distribution of individual temporal profiles of nuclear GFP-RelA, their averages (red thick lines), and their standard deviations (black thick dashed lines); three panels show damped-oscillatory patterns, rising patterns, and single-peaked patterns, from the second top to the bottom. In (C) and (D) we present the induction levels of IkappaBalpha mRNA and A20 mRNA obtained from Q-RT-PCR before stimulation (black lines) and after stimulation (red lines).

Supporting Figure 1: TNF alphas (+) feedback loops induces bistability and two equilibrium levels of nuclear NF-kappaB.

Table I. Biochemical reactions & associated reaction rates in our computational model of the NF-κB signaling network. Column *I* is the kinetic parameter, *II* is its units, *III* is its nominal value from the reference, *IV* is the reference, and V is our nominal value. The reaction rates labeled with [1] are from Ref. [39], those labeled [2] are from Ref. [45], those labeled [3] use an average value between those in Ref. [39] & Ref. [45], those labeled [4] are from Ref. [Salvarjoo FEBS Lett], and those labeled from [5] are from Ref. [Cho et al]. The units for [a] are $\mu M^{-1}s^{-1}$, for [b] are s^{-1}, for [c] are $\mu M\ s^{-1}$, and for [d] are μM.

Reactions	I	II	III	IV	V
IκBβ + NF-κB → IκBβ-NF-κB	Hβ	[a]	0.5	[2]	0.7753
IκBε + NF-κB → IκBε-NF-κB	Hε	[a]	0.5	[2]	0.2895
IKKa + IκBα → IKKa-IκBα	Aα	[a]	0.2	[1]	0.1813
IκBαn + NF-κBn → IκBαn-NF-κBn	Hα	[a]	0.5	[2]	0.4593
IKKa + IκBb → IKKa-IκBβ	Aβ	[a]	0.05	[3]	0.02997
IκBβn + NF-κBn → IκBβn-NF-κBn	Hβ	[a]	0.5	[2]	0.7753
IKKa + IκBe → IKKa-IκBε	Aε	[a]	0.05	[3]	0.04244
IκBεn + NF-κBn → IκBεn-NF-κBn	Hε	[a]	0.5	[2]	0.2895
IKKa+IκBα-NF-κB → IKKa-IκBα-NF-κB	Bα	[a]	1	[1]	1.024
NF-κB → NF-κBn	I1	[b]	0.0025	[1]	0.003037
IKKa+IκBβ-NF-κB → IKKa-IκBβ-NF-κB	Bβ	[a]	0.25	[3]	0.3683
NF-κBn → NF-κB	K01	[b]	0.00005	[3]	0.00005537
IKKa+IκBε-NF-κB → IKKa-IκBε_NFkB	Bε	[a]	0.25	[3]	0.42
IKKn → IKKa	K1	[b]	0.0025	[1]	0.003273
NF-κBn → NF-κBn + A20t	C1	[b]	0.0000005	[1]	0.000000506
A20 + IKKa → A20 + IKKi	K2	[a]	0.1	[1]	0.07075
0 → A20t	C2	[c]	0	[1]	0
IKKa → IKKi	K3	[b]	0.0015	[1]	0.00202
A20t → 0	C3	[b]	0.0004	[1]	0.0002438
0 → IKKn	Kprod	[c]	0.000025	[1]	0.000009752
A20t → A20t + A20	C4	[b]	0.5	[1]	0.5807
IKKn, IKKa, or IKKi → 0	Kdeg	[b]	0.000125	[1]	0.0001561
A20 → 0	C5	[b]	0.0003	[1]	0.0003769
Volume ratio of cytoplasm to nucleus	Kv	1	3	[1]	Variable
IKKa-IκBα → IKKa + IκBα	Dα	[b]	0.00125	[2]	0.002046
IκBαn-NF-κBn → IκBα-NF-κB	Lα	[b]	0.01	[1]	0.013979
IKKa-IκBβ → IKKa + IκBβ	Dβ	[b]	0.00175	[2]	0.0005609
IκBβn-NF-κBn → IκBβ-NF-κB	Lβ	[b]	0.005	[3]	0.001567
IKKa-IκBε → IKKa + IκBε	Dε	[b]	0.00175	[2]	0.002142
IκBεn-NF-κBn → IκBε-NF-κB	Lε	[b]	0.005	[3]	0.006583
IKKa-IκBα-NF-κB → IKKa + IκBα-NF-κB	Dα	[b]	0.00125	[2]	0.002046
IκBα-NF-κB → NF-κB	Mα	[b]	0.000025	[1]	0.00002837
IKKa-IκBβ-NF-κB → IKKa + IκBβ-NF-κB	Dβ	[b]	0.00175	[2]	0.000561
IκBβ-NF-κB → NF-κB	Mβ	[b]	0.000025	[3]	0.00003609
IKKa-IκBε-NF-κB → IKKa + IκBε-NF-κB	Dε	[b]	0.00175	[2]	0.002142
IκBε-NF-κB → NF-κB	Mε	[b]	0.000025	[3]	0.00000866
IKKa-IκBα-NF-κB → IKKa-IκBα + NF-κB	Eα	[b]	0.000001	[2]	0.00000144
IKKa-IκBα-NF-κB → IKKa + NF-κB	Pα	[b]	0.1	[1]	0.12928
IKKa-IκBβ-NF-κB → IKKa-IκBβ + NF-κB	Eβ	[b]	0.000001	[2]	0.00000124
IKKa-IκBβ-NF-κB → IKKa + NF-κB	Pβ	[b]	0.05	[3]	0.06454
IKKa-IκBε-NF-κB → IKKa-IκBε + NF-κB	Eε	[b]	0.000001	[2]	0.00000064
IKKa-IκBε-NF-κB → IKKa + NF-κB	Pε	[b]	0.05	[3]	0.08434
IKKa-IκBα + NF-κB → IKKa-IκBα-NF-κB	Fα	[a]	0.5	[2]	0.3789
IκBαn → IκBα	Qα	[b]	0.0005	[1]	0.0005123
IKKa-IκBβ + NF-κB → IKKa-IκBβ-NF-κB	Fβ	[a]	0.5	[2]	0.2135
IκBβn → IκBβ	Qβ	[b]	0.0005	[3]	0.0007398
IKKa-IκBε + NF-κB → IKKa-IκBε-NF-κB	Fε	[a]	0.5	[2]	0.3528
IκBεn → IκBε	Qε	[b]	0.0005	[3]	0.0002184
IκBα-NF-κB → NF-κB + IκBα	Gα	[b]	0.000001	[2]	0.00000064
IKKa-IκBα → IKKa	Rα	[b]	0.1	[1]	0.123
IκBβ-NF-κB → NF-κB + IκBβ	Gβ	[b]	0.000001	[2]	0.00000044
IKKa-IκBβ → IKKa	Rβ	[b]	0.1	[3]	0.03837
IκBε-NF-κB → NF-κB + IκBε	Gε	[b]	0.000001	[2]	0.00000069
IKKa-IκBε → IKKa	Rε	[b]	0.1	[3]	0.1571
IκBαn-NF-κBn → NF-κBn + IκBαn	Gα	[b]	0.000001	[2]	0.00000064
IκBαn-NF-κBn → NF-κBn	Sα	[b]	0.000001	[2]	0.00000037
IκBβn-NF-κBn → NF-κBn + IκBβn	Gβ	[b]	0.000001	[2]	0.00000044
IκBβn-NF-κBn → NF-κBn	Sβ	[b]	0.000001	[2]	0.000001131
IκBεn-NF-κBn → NF-κBn + IκBεn	Gε	[b]	0.000001	[2]	0.00000069
IκBεn-NF-κBn → NF-κBn	Sε	[b]	0.000001	[2]	0.000001037
IκBα + NF-κB → IκBα-NF-κB	Hα	[a]	0.5	[2]	0.4593
NF-κBn → NF-κBn + IκBαt	Uα	[b]	0.0000005	[1]	0.000000279

NF-κBn → NF-κBn + IκBβt	Uβ	[b]	0	[2]	0
NF-κBn → NF-κBn + IκBεt	Uε	[b]	0.00000005	[3]	0.000000059
IκBα → IκBαn	Vα	[b]	0.001	[1]	0.0009786
IκBβ → IκBβn	Vβ	[b]	0.001	[3]	0.0004871
IkBε → IkBεn	Vε	[b]	0.001	[3]	0.00147
IκBα, IκBαn → 0	Wα	[b]	0.0001	[1]	0.000132
IκBβ, IκBβn → 0	Wβ	[b]	0.0001	[3]	0.000133
IκBε, IκBεn → 0	Wε	[b]	0.0001	[3]	0.000042
IκBαt → IkBαt + IkBα	Xα	[b]	0.5	[1]	0.4552
IκBβt → IκBαt + IκBβ	Xβ	[b]	0.5	[3]	0.3828
IκBεt → IκBαt + IκBε	Xε	[b]	0.5	[3]	0.3304
0 → IκBαt	Yα	[c]	0.00000005	[3]	0.000000084
0 → IκBβt	Yβ	[c]	0.000000005	[3]	0.00000000414
0 → IκBεt	Yε	[c]	0.000000005	[3]	0.00000000508
IκBαt → 0	Zα	[b]	0.0004	[1]	0.0003375
IκBβt → 0	Zβ	[b]	0.0004	[3]	0.0002031
IκBεt → 0	Zε	[b]	0.0004	[3]	0.0004742
Total NF-κB amount	$NF\kappa B_o$	[d]	0.06	[1]	Variable
LPS + TLR4 → TLR4*	Q1	[a]	0.1	[4]	
TLR4* → TLR4	*Q2*	[b]	0.1	[4]	
TLR4* → MyD88	*Q3*	[b]	0.1	[4]	
MyD88 → IRAK	*Q4*	[b]	0.1	[4]	
IRAK → TRAF	*Q5*	[b]	0.1	[4]	
TRAF → TAK	*Q6*	[b]	0.1	[4]	
TAK + IKKn → IKKa	*Q7*	[a]	0.1	[4]	
TNFe + TNFR → TNFR*	*K1*	[a]	0.025	[5]	
TNFR* → TNFR	*K2*	[b]	0.025	[5]	
TNFR* + IKKKn → IKKKa	*K3*	[a]	0.025	[5]	
IKKKa → IKKKn	*K4*	[b]	0.025	[5]	
IKKKa + IKKn → IKKa	*K5*	[a]	0.025	[5]	
NF-κBn → NF-κBn + TNFt	*K6*	[b]	0.025	[5]	
TNFt → TNFi	*K7*	[b]	0.025	[5]	
TNFi→ TNFe	*K8*	[b]	0.025	[5]	

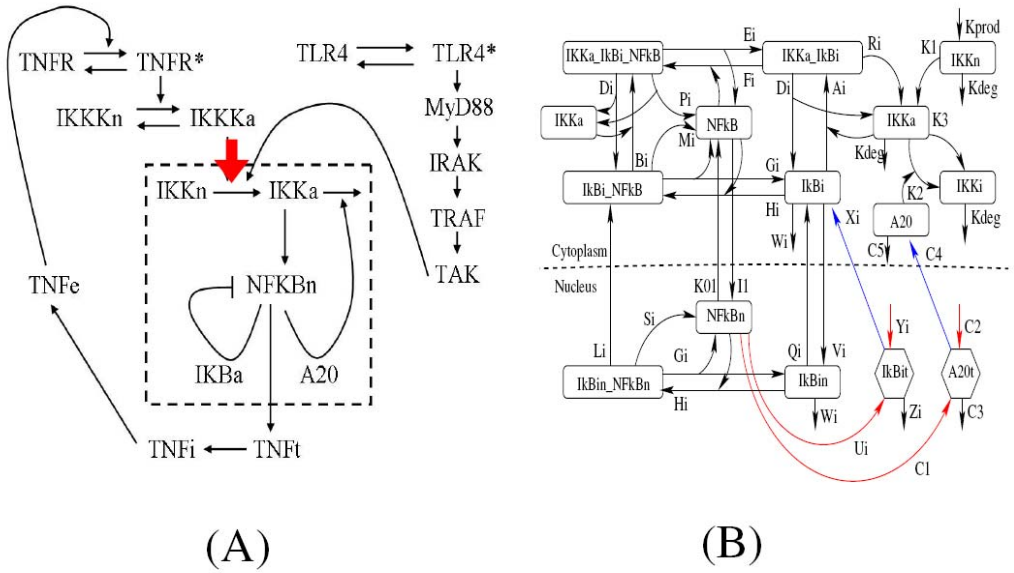

Figure 1

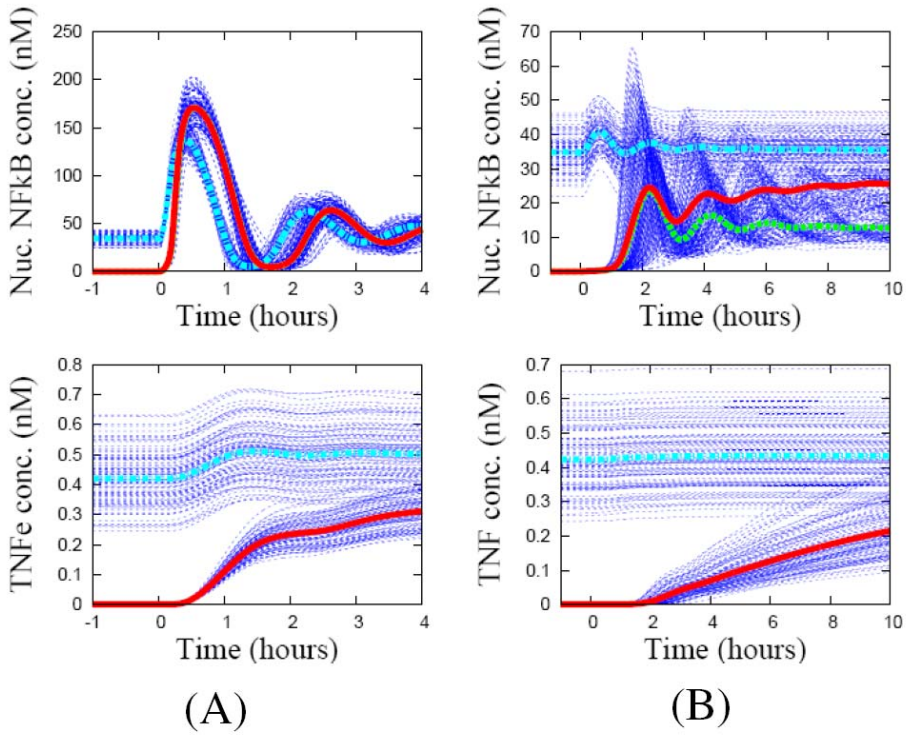

Figure 2

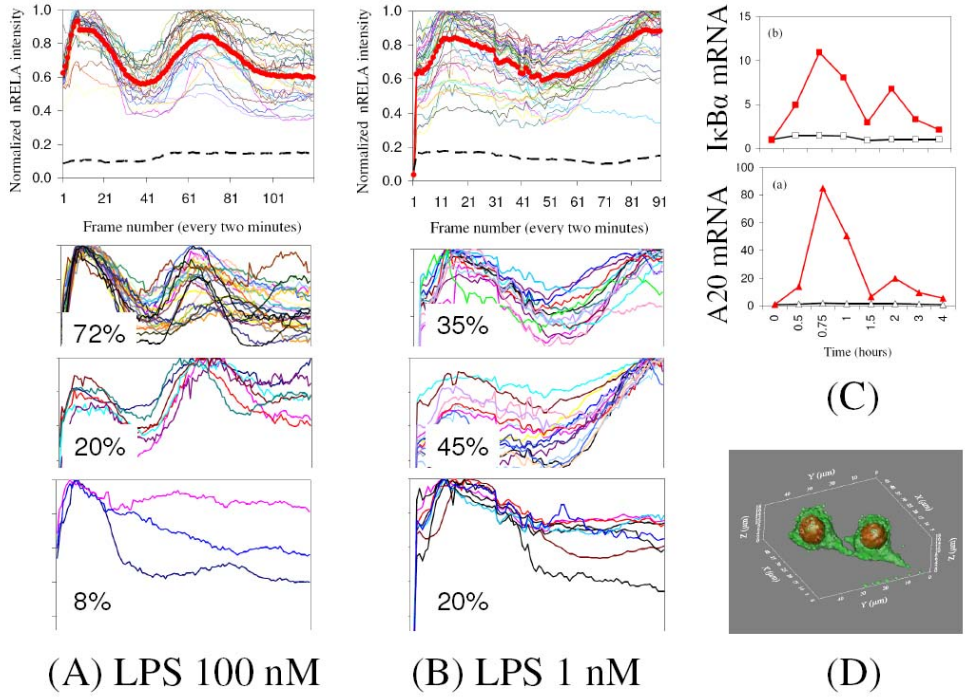
Normalized nRELA intensity
Frame number (every two minutes)
72%
20%
8%
35%
45%
20%
IκBα mRNA
A20 mRNA
Time (hours)
(C)
(A) LPS 100 nM
(B) LPS 1 nM
(D)

Figure 3

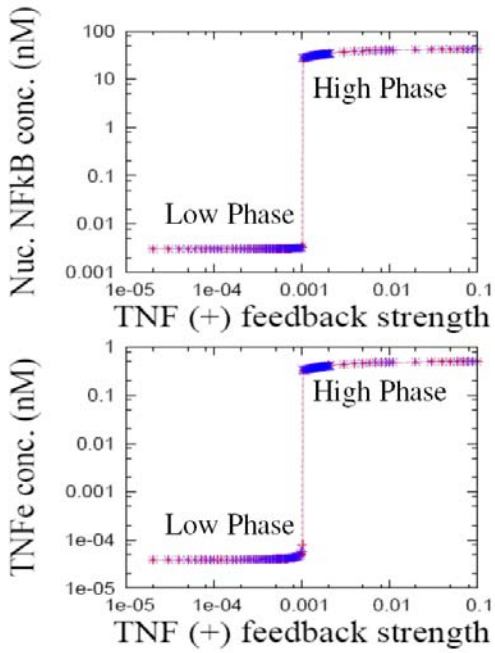
Nuc. NFkB conc. (nM)
High Phase
Low Phase
TNF (+) feedback strength
TNFe conc. (nM)
High Phase
Low Phase
TNF (+) feedback strength

6. Novel statistical ensemble analysis for simulating heterogeneous response in NF-κB signaling network

Jaewook Joo, Steven Plimpton, Jean-Loup Faulon

Abstract:

Introduction: A protein dynamics in a cell signaling system is usually modeled by a dynamical system, either a system of ordinary different equations or a stochastic simulator. These dynamic models require the precise knowledge of the associated kinetic data, e.g., both the copy numbers of the key proteins and the kinetic rate constants. But, this information, though critical, oftentimes is unattainable. Moreover the cellular response at the single cells is known to be highly heterogeneous and individualistic due to the strong influence by extrinsic and intrinsic noise. Here, taking into account only the effect of extrinsic noise on the cellular response, we are concerned about how to model the extrinsic noise-induced heterogeneous response at the single cells under the constraints of experimentally obtained population-averaged response, but without much kinetic information.

Methods: We propose a novel statistical ensemble scheme: extrinsic noise is regarded as fluctuations in network parameters and such fluctuations are modeled by randomly sampling the kinetic rate constants from the uniform distribution. Then we consider a large number of signaling system replicates, each of which has an identical network topology, but a uniquely different set of kinetic parameters. A protein dynamic response from each replicate represents the dynamics in a single cell and the statistical ensemble average response is regarded as a population-level response averaged over a population of the single cells. We devise an optimization algorithm to find the uniform distribution of the network parameters, which produce the correct statistical distribution of the response whose ensemble average and distribution agree well with the population-level experimental data and the desired dynamic heterogeneity, respectively.

Results: We apply this statistical ensemble analysis to NF-κB signaling system and (1) validate our approach by showing a good agreement between the statistical ensemble averages of the NF-κB response and the population-level experimental data for both wild

type and mutant cases, (2) predict two distributions of the NF-κB dynamic response at the single cells: the distribution of the heterogeneous dynamic patterns (either oscillatory or non-oscillatory) and of the dynamic features (period or maximum amplitude), (3) predict that both the distribution and the statistical ensemble average of the NF-κB dynamic response depends sensitively on the dosage of stimulant, (4) lastly exhibit the sigmoidally shaped dose-response in both the statistical ensemble average and the individual replicates.

Key Words: Statistical ensemble; extrinsic noise; NF-κB signal transduction

Target Journals: PLoS Comp. Biol; Biophys. J; Physical Biology; BMC Systems Biology; IET Systems Biology

I. INTRODUCTION

Evidence of heterogeneous cellular response and its effect on cell fate decision: Technical advances in fluorescence imaging have sparkled and generated a surge of interest in cellular response at the single-cell level (Elowitz 2002; Blake 2003; Cohen et al 2008). This technique has already uncovered significant cell-to-cell variation in both gene expression (Elowiz 2002; Blake 2003; Raser and O'Shea 2005; Raj et al 2006) and protein dynamics (Cohen et al 2008; Lahav et al 2005). Recent theoretical and experimental work revealed that this cell-to-cell variability originates from both intrinsic (McAdams and Shapiro 1995; Arkin et al 1998; Thattai and van Oudenaarden 2001) and extrinsic noise (Swain 2002; Rosenfeld et al 2005). Noise critically affects cell-fate decision in developmental processes (Arkin et al 1998) and drug resistance (Cohen et al 2008). Moreover, response averaged over a population of the cells is oftentimes noticeably disparate from that in the single cells. The rational link between these two quantities needs to be established. Here, we propose a novel statistical method to unravel noise-induced discrepancy between single cell level and population level responses and to model the noise-driven heterogeneous cellular response at the single cells.

Criticism: The current modeling framework utilizes the dynamic, either deterministic or stochastic, models to unravel and predict the dynamic response of the biological networks. Most of the dynamic models contain many unknown kinetic rate constants,

which need to be parameterized. A conventional parameterization scheme primarily focuses on identification of a single set of network parameters, which optimize the distance between the experimental data and the model prediction. As a result, the cellular response of the model is typically represented by a single dynamic pattern. This parameterization approach is a consequence of a strong influence by a deterministic viewpoint prevalent in biology: a biological response to a known stimulus should be robustly homogeneous and uniform and absolutely predictable. “Sloppy Cell”, however, identifies a large number of the sets of the kinetic parameters of the biological network under the relaxed constraint that the model prediction is fitted to the experimental data within the experimental errors (Brown et al 2004). This is a clever fitting algorithm, but is still based on the same “homogeneous response” assumption and isn’t designed to model the single cell behaviors. But, with the advancement and the availability of the single-cell level imaging techniques, the assumptions behind the above modeling methods are proven to be incorrect; the cellular response at the single cell level is heterogeneous and must be represented by a distribution of those heterogeneous responses. Therefore, the current modeling method needs to be modified to incorporate this single cell level property.

Modeling of extrinsic noise and previous efforts: In general, both intrinsic and extrinsic noises are the source of the heterogeneous cellular responses. The intracellular signaling networks are stochastic generators because they typically consist of a small copy number of their constituents and are constantly under a large fluctuation in the copy number of their constituents. Moreover, the signaling networks are exposed to time-varying environmental conditions and/or coupled to other unknown stochastic signaling networks. The former is called intrinsic noise because it is related only to a randomness of the reaction events. The effect of intrinsic noise on the cellular response is widely studied (Arkin et al 1998). The latter is extrinsic noise and its origins are unknown, but the few known origins are cell cycle (Rosenfeld et al 2005) and fluctuations in the copy number of transcriptional regulators in the upstream (Volfson et al 2006). Extrinsic noise affects all the constituents of the signaling network simultaneously and in a correlated manner. Several attempts were made to model extrinsic noise: to name a few, extrinsic

noise is modeled as fluctuations in the network parameter values (Paulsson 2004) and the Gillespie's standard stochastic simulation algorithm (Gillespie 1997) is modified to take into account the time-varying kinetic rate constants (Swain's group 2008).

Uncertainty in network parameter values: Most of the biological dynamic models require the knowledge of a functional form and a kinetic rate constant of the associated reaction in a biological network. The lack of this critical kinetic information is one of the main drawbacks of the dynamic models and hampers their predictability. Thus, there is a great need to devise a modeling scheme, which doesn't require the precise kinetic information of a biological network. Extrinsic noise and the resulting heterogeneous response suggest that the kinetic rate constants should reflect uncertainty in their values, partly because of uncertainty in experimental measurements and partly because of their connection to the external fluctuations with unknown origins. Taking into account extrinsic noise, we can readily relax a strict constraint imposed to the parameterization of the kinetic parameters of the dynamic models.

Novel statistical ensemble analysis: We propose a statistical ensemble (SE) approach, which not only overcomes the lack of precise knowledge of network parameter values, but also provides a way to model extrinsic noise-driven heterogeneous cellular dynamic responses. We find a concept of the SE in the statistical physics useful in describing extrinsic noise and its effect on the resulting cellular responses. In our view, a biological system should be regarded as a complex system comprising a large number of components and elementary interactions among them and only the macroscopic state of such a complex bio-system is observable while its microscopic kinetic details are hidden and unknown to the observers. Taking extrinsic noise as fluctuations in kinetic parameter values (Paulsson Nature 2004), we propose a novel SE analysis. First, a population of the cells is modeled with a SE of a bio-system, i.e., a large number of the copies of identical system. Second, we assume that individual cells influenced by extrinsic noise operate and function in a biologically feasible range of kinetic parameter values. To simulate extrinsic noise, different values of kinetic parameters are sampled from a biologically feasible distribution and assigned to each system copy. Each copy corresponds to an individual single cell influenced by extrinsic noise. Each copy is unique in its kinetic parameter

values and thus responds to the same stimulus diversely. The resulting dynamic response is no longer a single output but is represented by a distribution of heterogeneous responses from a SE of the system. We assign the same weight to each copy to calculate a macroscopic state and obtain the SE average of the system's response, which should be regarded as experimental data averaged over a population of the cells. The macroscopically observable response, the SE average, may take a simply behaving dynamic pattern. But, individual cell behavior can be very irregular, dissimilar, and diverse. The sum function (the SE average) annihilates any individualistic, heterogeneous, and non-smooth behavior. Thus, this SE analysis not only unravel the extrinsic noise-driven disparate behaviors between single cells and a population of the cells, but also can predict individual cell behaviors constrained by the experimental population level data. An important technical question is how to identify the biologically feasible and true distribution of extrinsic noise, which the kinetic parameters should be sampled from. Here we simplify the distribution to be uniform and our task to find the location and the interval size of this uniform distribution. We apply this statistical ensemble analysis to NF-κB signaling system.

6. Application of statistical ensemble analysis to NF-κB signaling system: NF-κB is a pleiotropic regulator of gene control and plays significant roles on various cellular functions such as differentiation of immune cells, development of lymphoid organs, and immune activation (Hoffmann et al., 2006; Verma and Stevenson, 2006). NF-κB shuttling between nucleus and cytoplasm is auto-regulated by the NF-κB signaling module, which consists of IκB (inhibitor κB), IKK (IκB kinase), and NF-κB. In the absence of stimulus, IκB forms a hetero-dimeric complex with NF-κB, preventing NF-κB from entering into the nucleus. Upon stimulation, the phosphorylated IKK catalyses the degradation of IκB from the IκB-NF-κB complex and frees up NF-κB whose nuclear localization initiates transcription of NF-κB target genes such as inflammatory cytokines (TNFα, IL-1, IL-6), chemotactic cytokines (MIP-1a), Th1 and Th2 response activation (IFN and IL-10), and lastly but most importantly negative regulators (IκBα, IκBβ, IκBε, and A20) which terminates the NF-κB signaling. Based upon the up-to-dated knowledge

of NF-κB signaling, Hoffmann et al constructed a complex biochemical reaction network of NF-κB signaling consisting of IKK, NF-κB, and three IκB isoforms and transformed it into a set of ordinary differential equations with dozens of unknown kinetic parameters (Hoffmann et al., 2002). After identifying a single set of parameter values yielding the best fitting of the model to population level experimental data, they used their model to corroborate their argument about the role of each of three IκB isoforms: IκBα induces oscillatory shuttling of NF-κB while IκBβ and IκBε make the oscillation damped (Hoffmann et al., 2002). Lipniacki et al. computationally demonstrated that an additional negative regulator A20 has a definitive role as NF-κB signal terminator, assuming that A20 inactivates IKK phosphorylation (Lee et al., 2002; Lipniacki et al., 2004). Using the single cell fluorescence imaging, Nelson et al showed a remarkable phenomena at the level of single cells: some cells exhibits sustained oscillatory shuttling of NF-κB while others does non-oscillatory patterns, i.e., heterogeneous cellular response (Nelson et al. 2005; Lahav et al. 2004). Though NF-κB shuttling patterns are sustained-oscillatory at the single cells, their population level response is highly damped-oscillatory because averaging over a population of the cells masks oscillations at individual cells. However, Barken et al argued that, with the supportive experimental data, NF-κB dynamic responses at individual cells are highly synchronized and homogeneous (Barken et al., 2005). Hayot and Jayaprakash showed that intrinsic noise can unravel the mechanism behind the discrepancy between the oscillatory behaviors at single cells and the damped-oscillation at a population of the cells (Hayot and Japaprakash 2006).

7. Summary: We thoroughly investigate the effect of extrinsic noise on key protein dynamics in IKK-NF-κB-IκB-A20 signaling system. This signaling network is presented in Fig. 1 and consists of IKK, cytoplasmic and nuclear NF-κB, and two groups of negative regulators such as three isoforms of IκB and A20. Using the statistical ensemble analysis, we demonstrate that extrinsic noise, modeled as fluctuations in network kinetic parameters, derive the large deviation of the individual cell-level response away from their ensemble average. An ensemble of the NF-κB signaling system is generated by the Statistical Ensemble Generation method. This NF-κB network ensemble is stimulated by

either large or small signal strength. In section II.1 we demonstrate that the statistical ensemble average of the individual profiles of each key biochemical species of the NF-κB signaling network is well fitted to experimental population level data for wild type and various mutant cases. In section II.2, we present a statistical analysis of the individual nuclear NF-κB profiles from the ensemble of a wild type and the mutants: the distribution of the dynamic characteristics such as dynamic patterns and dynamic features. In section II.3, we make a prediction about the dosage-dependent NF-κB response at the single cell levels: dosage-dependent statistical ensemble average behavior, dosage-dependent distribution of dynamic patterns, and that of dynamic features. Lastly, in section II.4, we show that both statistical ensemble average of dose-response curve and each individual curve are sigmoidally shaped.

II. RESULTS

1. Fitting population level experimental data with their SE average of NF-κB signaling network

A. Wild type case: For the wild type case, we demonstrate that the SE scheme generates the significant cell-to-cell variability in protein dynamics, while successfully making the SE averages agree well with the population-level experimental data (EMSA or western blot or northern blot) of the key biochemical species as shown in Fig. 2. For the nuclear NF-κB profiles in Fig. 2 (a), the individual timings of the first peak are almost identical while the individual amplitudes of the first peak vary significantly with the deviation up to 100 % of its SE average. However, both the timings and amplitudes of the subsequent peaks exhibit a very significant cell-to-cell variability, consequently causing its SE average to take a damped oscillatory pattern with an outstanding peak followed by rapidly decaying amplitudes of subsequent peaks. Thus, the extrinsic noise produces “the masking effect of averaging over a population of asynchronous curves" just like the intrinsic noise does (Hayot et al JTB 2006).

B. Fluctuations in IKK and IκB concentration as source of cell-to-cell variability in wild type case: The large variation in the first peak amplitude of the nuclear NF-κB as shown in Fig. 2(a) originates from the IKK profile in Fig. 4 (b) where the individual curves of IKK concentration look a lot alike, yet with a great difference in their first peak amplitude which is laterally transferred to the large variation in the first valley of IκB isoforms as shown in Fig. 2 (b) and (c). Thus, the cell-to-cell variation in kinetic rate constants regulating the levels of both the pre-activated IKK (IKKn) and the activated of IKK (IKKa) is the source of the cell-to-cell variation in the first peak of nuclear NF-κB. Likewise, the asynchronous behavior of the individual nuclear NF-κB profiles after two hours as shown in Fig. 2(a) originates from the cell-to-cell variability in various kinetic reactions: for example, it is cause by the variation in the second peak of the IκB isoforms as shown in Fig. 2 (b)-(d), which is caused by the variations in both the pre-stimulated level of IκB isoforms, by the variation in the first valley of IκB isoforms due to the cell-to-cell variability in IKK, and by the variation in the kinetic rate constants regulating the formation of NF-κB-IκB complex. We demonstrate that the dynamic characteristics of heterogeneous individual profiles of nuclear NF-κB is due to the extrinsic fluctuations in kinetic rate constants regulating the levels of IKK, IκBα, IκBβ, IκBε, NF-κB-IκB complex.

C. IκB isoforms double knocked-out and A20 knocked-out mutants: For the case of IκB isoforms double knocked-out and A20 knocked-out mutants, we set the synthesis rate of the IκB isoforms and A20 mRNA to zero, respectively. For the IκBβ and IκBε knocked-out mutant as shown in Fig. 3(a), the individual profiles of nuclear NF-κB are much more oscillatory (about a half of the curves are sustained oscillatory in Fig. 8) than those of wild case (only less than 10 % are sustained-oscillatory in Fig. 8). But, the SE average takes a damped oscillatory pattern and is a little more dynamical than that of the wild type case. This is mainly due to" the masking effect of averaging over a population of asynchronous curves". The peaks of the SE average correspond to the peaks from population level experimental data by Electro Mobility Shift Assay (EMSA) at 15 min, 2.5 hours, and 4 hours. For the IκBα and IκBε knocked-out and the IκBα and IκBβ

knocked-out mutants as shown in Fig. 3(b) and 3(c), both SE averages of nuclear NF-κB take the similar looking "single-peaked" patterns as the population level EMSA measurements. For these two mutants, all the individual curves look alike to each other and each curve differ from the others only in its nuclear NF-κB level while the deviation of the individual curves from the SE average is as large as the 100 % of the SE average. For the A20 knocked-out mutant as shown in Fig. 4, both the SE averages of all the biochemical species take a single-peaked pattern just like the population level experimental data do. Though individual profiles are very alike, the deviation of the individual curves from its SE average is as large as 100 % of its SE average. In summary, for all the knocked-out mutants, both the individual profiles and their SE average of nuclear NF-κB take a uniform single-peaked pattern, but the variation in the nuclear NF-κB is very large among the individual profiles due to extrinsic noise.

D. Dependence of the SE average of nuclear NF-κB on the heterogeneity measure: In Fig. 5 we show how the population level experimental measurements can place a strict restriction on the choice of the heterogeneity measure χ, defined as the interval size of the uniform distribution from which each kinetic parameter is sampled. While fixing the kinetic rate constants at their reference values, we increase the heterogeneity measure and observe how heterogeneous the individual profiles of nuclear NF-κB become. The SE average of nuclear NF-κB becomes much less oscillatory for the higher value of heterogeneity measure as shown in Fig. 5. For a small value of heterogeneity measure in Fig. 5 (a) (χ=10 %), we can clearly see that all individual curves are in phase with each other, making its SE average highly oscillatory too. For the higher values of heterogeneity measure in Fig. 5 (c) (χ=50 %) and 5 (d) (χ=70 %), a large fraction of individual curves are sustained oscillatory, but they are largely out of phase and asynchronous to each other and the resulting SE average is no longer oscillatory, but heavily under-damped oscillatory. Because the higher χ value assumes the larger sampling space, individual curves of nuclear NF-κB take the more heterogeneous dynamic patterns: some are sustained oscillatory while others are single-peaked. Thus, if

the population level experimental measurements exhibit the oscillatory response, this data can place a strict restriction on the choice of the heterogeneity measure.

2. Prediction of the SE distribution of the dynamic patterns and the dynamic features for both the wild type and the mutants

A. Distribution of the dynamic features: In Fig. 6 we demonstrate that the SE analysis can capture the distribution of the dynamic features (see methods) of the individual cellular responses and its variation upon the knocked-out of the genes. It is also shown that there is a significant amount of overlap between the distribution of the wild type and that of the other mutants. This implies that if we rely on the conventional parameterization scheme which identifies a single set of parameters and present a single representative response, we can easily fall into a deceptively incorrect conclusion about the effect of gene knocked-out on the cellular response. To avoid such a pitfall, we represent the single cell level dynamic response with the distribution of their dynamic features and observe any significant change in the distribution when genes are knocked out. For Fig. 6 (a), the distributions of the First Maximum are invariant between the mutants and the wild type. This dynamic feature shouldn't be chosen as an indicator of the physiological defects due to gene knocked-out. For Fig. 6 (b), the A20 knocked-out mutant increases the average value of the First Translocation Time while the IκBβ and IκBε knocked-out mutant decreases it. But, the wild type and two other mutants share the similar distribution. In Fig. 6 (c), only the wild type and the IκBβ and IκBε knocked-out mutant have their averages of the First Period at about 2.2 and 2 hours respectively, and the other mutants have too broadly distributed First Period to define their averages. In Fig 6 (d), the ratio of the First Minimum to the First Maximum indirectly measures the spikiness of the oscillations defined as the deep valley between two adjacent maxima: The smaller this ratio gets, the spikier the temporal profile becomes. Only the wild type and the IκBβ and IκBε knocked-out mutant exhibit the spiky responses. In Fig 7 (f), the ratio of the Steady State to the First Maximum provides useful information about the relative magnitude and strength of the negative regulators of IκB isoforms and A20. Remembering that the distributions of the First Maximum are invariant between the wild

type and the mutants, we conclude that the smaller steady state level of nuclear NF-κB means the stronger negative feedback. We list the mutants in order of the steady state level: A20 knocked-out mutant < IκBα and IκBε knocked-out mutant < IκBα and IκBβ knocked-out mutant < IκBβ and IκBε knocked-out mutant < wild type. Now the order of the strength of the negative regulators can be inferred from the above ordered list: A20 > IκBα > IκBε > IκBβ. This order is determined by our choice of the kinetic rate constants.

B. Distribution of the dynamic patterns: The individual time-series of the nuclear NF-κB concentration can be classified into one of four dynamic patterns as shown in Fig. 7: damped oscillation, sustained oscillation, single peaked pattern, and hyperbolic pattern. The underlying mechanism for each dynamic pattern is rather simple: The hyperbolic (or over-damped) pattern originates from the strong strength of the negative feedback loops. while the single-peaked pattern comes from the weak negative feedback loops. Oscillatory pattern arises from a moderate strength of negative feedback loops. But, it remains open to correlate each dynamic pattern with a cellular physiological condition. For the cases of the wild type and the mutants, we generate and stimulate the SE of the NF-κB network with the same signal strength (TR=1), respectively. Then we classify a thousand individual temporal profiles into one of four dynamic patterns. The distributions of the dynamic patterns are represented by the bar graphs in Fig. 7 and show that the SE of the wild type or the mutant takes at least two different dynamic patterns under the same stimulation. For wild type case, the distribution of the nuclear NF-κB profiles is very skewed to a single pattern, the damped-oscillatory pattern, while a less than 10 % of the profiles are sustained-oscillatory. This indicates that for the wild type case the damped oscillation is the most probable pattern and is robust against the perturbation of the network parameter values. For the A20 knocked-out mutant, both single-peaked and damped-oscillatory patterns are almost equally probable. But, those damped oscillatory profiles are very much like a single-peaked pattern. In other words, for this mutant, the damped-oscillation occurs at a particular region of the parameter space where the strength of the negative regulators is not strong enough to induce the oscillatory pattern. For IκBβ and IκBε knocked-out mutant, sustained-oscillatory and damped-oscillatory patterns are equally probable dynamic response. The damped-oscillatory patterns in this mutant are

very different from those in the A20 knocked-out mutant and are similar to a sustained-oscillation. The fraction of the sustained oscillation (about 50 %) dramatically increases in comparison to the wild type case (less than 10 %). For both IκBα and IκBβ knocked-out and IκBα and IκBε knocked-out mutants, their respective distributions are similar to that of A20 knocked-out mutant in Fig. 7. As evidently shown in Fig. 3 (b) and 3 (c) and Fig. 4 (c), both the individual profiles and the statistical ensemble average of the nuclear NF-κB concentration for the A20 knocked-out, the IκBα and IκBβ knocked-out, and the IκBα and IκBε knocked-out mutants share the similar single peaked pattern. In summary, there are two distinctive groups exhibiting two respective dynamic patterns of nuclear NF-κB profiles: the first group, the wild type and the IκBβ and IκBε knocked-out mutant, show the highly oscillatory pattern and the second group, the A20 knocked-out, the IκBα and IκBβ knocked-out and the IκBα and IκBε knocked-out mutants, shows the (non-oscillatory) single-peaked pattern.

3. SE analysis of dosage-dependent NF-κB behavior

A. Dosage-dependent SE average and individual profiles of nuclear NF-κB concentration: The SE of NF-κB network is stimulated with either the large (TR=1) or the small (TR=0.01) signal strength, respectively. The dosage-dependent behavior of both the SE average and the individual temporal profiles of the biochemical species are presented in Fig. 8. The small dosage induces either monotone-increasing (hyperbolic) or single peaked IKK individual profiles as shown in Fig. 8 (b) while the large dosage make them take the single-peaked pattern possessing a prominent peak as shown in Fig. 8 (g). This dosage-dependent IKK profiles are directly transferred to the cytoplasmic IκBα profiles. For the small dosage, the hyperbolic IKK profiles induce the exponentially decaying IκBα profiles as shown in Fig. 8 (c). On the contrary, for the large dosage, the noticeable peaks of the IKK profiles suppress the cytoplasmic IκBα levels and, when the peaks of the IKK profiles drop down to their steady state levels, the cytoplasmic IκBα levels recover back to their equilibrium levels in a damped oscillatory manner as shown in Fig. 8 (h). The nuclear NF-κB profiles follow the IκBα profiles but in an exactly

opposite way: the cytoplasmic IκBα sequesters NF-κB in the cytoplasm, inhibiting nuclear localization of NF-κB. Since the mRNA synthesis rate of the NF-κB target genes is assumed to be linearly dependent on the nuclear NF-κB concentration, the profiles of both A20 mRNA and IκBα mRNA follow the nuclear NF-κB profile after half an hour time lag.

B. Dosage-dependent distribution of the dynamic features: After stimulating the SE of the NF-κB system with the large (TR=1) or the small (TR=0.01) dosage, we obtain the distribution of each dynamic feature from a thousand nuclear NF-κB profiles as shown in Fig. 9. In Fig. 9 (a) and (c), both the First Maximum and the First Period share the similar dosage-dependent behavior: the smaller dosage induces the distribution mode located at the smaller First Maximum or the smaller First Period while the full half maximum width of the distribution is independent of the dosage. But, for both the First Translocation Time and the Ratio of the First Minimum to the First Maximum, the dosage-dependent behavior is opposite to the previous case as shown in Fig. 9 (b) and 9 (d): the larger dosage induces the distribution peaked at the earlier First Transition Time or at the smaller First Minimum level. Moreover, the larger dosage makes their distributions the more narrowly distributed. This indicates that the larger dosage induces the earlier and spikier response and the smaller dosage induces the more heterogeneous First Maximum and First Minimum levels of nuclear NF-κB. Lastly, both the ratios of the Second Maximum to the First Maximum and of the Steady State to the First Maximum share the similar dosage-dependent behavior as shown in Fig. 9 (e) and 9 (f): the smaller dosage induces the mode of the distribution at the larger values, i.e., closer to one. In other words, when stimulated by the smaller dosage, the levels of the First Maximum, of the subsequent maxima, and of the Steady State are the same, i.e., NF-κB profiles take either monotone-increasing pattern or single-peaked pattern with low peak amplitude. In addition, the full half maximum width of the distribution is unaffected by the change of the dosage.

C. Dosage-dependent distribution of the dynamic patterns: As shown in Fig. 10, when stimulated by the small (TR=0.01) dosage, 80 % of the nuclear NF-κB profiles are

damped-oscillatory whereas only 20 % of them are single-peaked. But, those damped oscillatory patterns are a lot like a single-peaked pattern. The distribution induced by the large dosage (TR=1) corresponds to that of the wild type case in Fig. 7. We note that the distribution of the dynamic patterns, the SE ensemble average, and individual profiles of nuclear NF-κB concentration upon the small (TR=0.01) dosage stimulation in Figs. 8 and 10 are very similar to those from the IκBα and IκBε knocked-out mutant upon the large (TR=1) dosage stimulation in Figs. 3 and 7. When the heterogeneity measure χ increases from its present value χ=30 % to χ=70 %, the small dosage stimulation generates more heterogeneous dynamic patterns, i.e., more equally distributed dynamic patterns of the nuclear NF-κB.

4. Sigmoidally shaped SE average of the dose-response curves

We numerically investigate the distribution of the dose-response curves from the SE of the NF-κB system. We generate the SE of the NF-κB system with only 50 replicates because of high computational cost to get one dose-response curve. The SE of NF-κB signaling system is stimulated with a persistent signal strength for 30 hours duration and the average (quasi-) steady state level of nuclear NF-κB concentration between 20 and 30 hours after stimulation is measured. To test for the presence of the hysteresis effect, we compute the dose-response curve twice, i.e., increase the signal strength from *TR=0.1* to *TR=0* in a step-like manner and then decrease it from *TR=0.1* to *TR=0.* For each replicate in the SE, both forward and backward dose-response curves look exactly the same and this indicates the absence of hysteresis effect in the NF-κB signaling system and take a sigmoidal shape as shown in Fig. 11. The steady state nuclear NF-κB levels change dramatically at the inflection points of the sigmoidal curves in Fig. 11. For the signal strength smaller than the inflection point of each curve, the stationary nuclear NF-κB level is very low while for the signal just greater than the inflection point, the stationary level quickly reaches a plateau. Lastly, the SE average of those individual dose-response curves is sigmoidally shaped.

III. DICUSSION

New predictions: In this paper, we devise a novel statistical method to mimic the protein dynamics in a population of the cells under the influence of extrinsic noise. We demonstrate, after making the SE average to match with a population level experimental data, that the SE of the signaling system produces several experimentally observable distributions of the dynamic characteristics of the protein profiles. The main predictions are listed as follows: (a) under the same experimental condition, the nuclear NF-κB profiles are expected to take the heterogeneous dynamic patterns at the single cell level, (b) the larger dosage induces the more oscillatory dynamic patterns of the nuclear NF-κB while the smaller dosage does the single-peaked patterns, (c) the larger (smaller) dosage makes the First translocation time narrowly-distributed (broadly-distributed) and the peak of its distribution shifted to the earlier (later) time, and (d) the shape of the dose-response curves both at the single cell level and the population level is sigmoidal. Most of our predictions, e.g., (a) – (c), have been verified by our colleagues (reference). We hope to elicit more experimental efforts to verify the above predictive dynamic behavior in the single cells.

Novel viewpoint of statistical ensemble analysis: We like to emphasize that the novelty of our SE analysis lies not on the technical part, but on the new viewpoint on the cellular response. All the previous papers focus mainly on the analysis of the dynamic behavior of the model dynamic systems in a restricted parameter space by the usage of the Monte Carlo sampling of the kinetic parameter values and the classification and/or sensitivity analysis of the resulting dynamic response (reference; Joo et al 2007). But, we start with a totally different viewpoint that the protein dynamics of the individual cells are intrinsically heterogeneous because they are exposed mainly to extrinsic noise and likely to have large fluctuations in the kinetic parameters controlling the abundance of the biochemical species in the cells.

Sigmoidally shaped dose-response curve: The sigmoidal shape of the dose-response curve reveals two important properties of the NF-κB signaling: the switching behavior

and the monostability (no hysteresis). The inflection points of the individual sigmoidal curves can play the role of the activation threshold of the NF-κB signaling pathway. As shown in Fig. 11, the NF-κB response is so little to the signal strength below the threshold while its response significantly increases for the signal strength just above the threshold. Knowing that some of the NF-κB target genes are the inflammatory cytokines and overly expressed inflammatory response is adversary to the host, we can speculate that the NF-κB signaling network employs this sigmoidal dose-response curve to down-regulate the excessive inflammatory response, i.e., turn it on only if the danger level is significantly high, otherwise shut it down. However, the amplitude and the timing of the first peak of the inflammatory cytokines such as TNFα are known to be critical to elicit the timely and effective immune response (Mann et al 2002). In this case, we'd better to measure the dosage-dependent transient dynamic response of NF-κB target genes and investigate the shape of the dose-(transient dynamic) response. Lastly, TNFα autocrine signaling forms the (+) feedback loop in the NF-κB signaling network and can induce the bistability, which may modify our results on the monostability.

True distribution of extrinsic noise: Our statistical analysis of the protein dynamics depends on how biologically and realistically the computationally generated SE of the NF-κB system represents a population of the individual cells. This question is equivalent to what is the true distribution of extrinsic noise, i.e., the distribution according to which the kinetic parameters should be sampled. In this paper, we simplify this problem greatly by assuming that this distribution is a uniform one. We devise a heuristic fitting algorithm to find the interval of the uniform distribution of the kinetic parameters by minimizing the discrepancy between the SE analysis and the population level experimental data. But, to make the sampling more biological, it should be taken into account that the distribution of extrinsic noise can change in time periodically as the cells undergo cell cycle. Moreover, though we assume no correlation between any pair of the kinetic parameter values, the parameters may be statistically dependent simply because the cellular energy resource must be limited: e.g., as one kinetic process gets accelerated, then the others should decrease in order to balance the cellular energy consumption. To simulate the protein dynamics in the real single cells, first, it is highly required to devise

the single cell experimental techniques from which we can infer this true distribution of extrinsic noise. Second, the optimization problem needs to be solved rigorously: to find the distribution of the kinetic parameters of the dynamic network which minimizes the difference between the SE average and the population-level experimental measurements and simultaneously reproduce the experimentally observed heterogeneous protein dynamics in the single cells.

5. Classification: Our choice of only four dynamic patterns of nuclear NF-κB profiles greatly simplifies the statistical analysis and helps us observe clearly the change of the distribution upon gene knocked-out perturbations. Our choice is based on the dynamical and mathematical characteristics of the protein profile. However, it is possible that this simplification neglects the other biologically important details of the nuclear NF-κB profiles. If we go by a different choice of the dynamic patterns, e.g., classification by period or by steady state level, it may change the distribution of the dynamic patterns and its change upon perturbations.

IV. METHODS

Six dynamic features of nuclear NF-κB profile: We define six dynamic features to represent the "unique" characteristics of temporal profiles of nuclear NF-κB concentration. As shown in Supporting Figure 2, the first translocation time depicts the time when the first peak occurs; the first period measures the time between the first two peaks; the first and the second maxima define the peak amplitudes of the first and the second peaks; the first minimum means the amplitude of the first valley; the steady state refers to the amplitude level at sufficiently long time. Making the first maximum level the reference, we present a scaled ratio, i.e., the level of the first minimum, the second maximum, and the steady state normalized by the first maximum. The distributions of the dynamical features are presented in Figs. 6 and 9.

Generation of the SE of NF-κB signaling network: Each kinetic rate constant listed in Table 1 is randomly sampled from an interval ($x_0(1-\chi), x_0(1+\chi)$) where x_0 is the reference value and χ is a heterogeneity measure. To enhance the efficacy of the sampling in the high dimensional space, we employ the Latin Hypercubic sampling method discussed in methods section. For this paper, we set $\chi = 0.3$. To generate the SE consisting of *N* replicates, we simply make *N* sets of randomly sampled kinetic parameters.

Algorithm to fit the SE average to population level experimental data: We will not attempt to fit the SE average to the entire time-series data. To try to do so results in notorious over-fitting: much more parameters to fit much less data. Moreover, biology data are rather qualitative than quantitative. Also, we learn that there are only a handful number of the kinetic parameters in the NF-κB signaling network whose variation significantly affects the temporal profile of the nuclear NF-κB concentration (Joo et al 2007). Our fitting algorithm is to fit the dynamic features of the SE average to those of the experimental time-series data. Based on our previous studies (Joo et al 2007), we choose two kinetic parameters most highly correlated with each dynamic feature and vary them until the dynamic features between the SE average and the experimental time-series data are matched. Here are the actual steps that we take: For step 1, use an educated guess for kinetic parameters and set the heterogeneity measure to $\chi = 0.9$. For step 2, generate the SE and the resulting protein dynamic profiles and calculate the deviation of the six dynamic features of the SE average from the target dynamic features. For step 3, identify the most deviated dynamic feature and modify two kinetic parameters associated with that dynamic feature. For step 4, repeat the steps one through three until the dynamic features get close to the target values. Fro step 5, when the good fitting is not achievable with the pre-set value of χ, we decrease it in a step-like manner. All the Figures 2 through 5 are obtained through the above fitting algorithm.

Numerical simulation of the NF-κB signaling network: A system of ordinary differential equations is derived from the NF-κB signaling network in Fig. 1 and the

kinetic parameters in Table 1. Using the Runge-Kutta 4th order, we numerically solve the dynamic model with the sampled kinetic parameters and with the initial conditions: the zero concentrations of all the other biochemical species and a sampled total concentration of cytoplasmic NF-κB. Before stimulating the system ($TR=0$), the dynamic system runs for 33 hours until its constituents reach their equilibrium values. Then, we simulate the persistent stimulation by turning on the reaction, IKKn → IKKa with a rate $TR \cdot K1$, i.e., by assigning a non-zero value to *TR*, where *TR* stands for the dosage of a stimulant.

Latin Hypercube sampling (LHS): LHS is a constrained Monte Carlo sampling scheme. The Monte Carlo sampling scheme is a conventional approach and a common choice for the uncertainty assessment of a computational model. By sampling repeatedly from the assumed joint probability function of the input variables and evaluating the response for each sample, the distribution of the response of the computer model can be estimated. This approach yields reasonable estimates for the distribution of the response if the number of samples is quite large. However, since a large sample size requires a large number of computations from the computer model (a potentially very large computational expense), an alternative approach, Latin Hypercube sampling, can be used. LHS yields more precise estimates with a smaller number of samples, and is designed to address the above concern (Swiler et al 2004). Suppose that the computer model has K kinetic rate variables and we want N samples. LHS selects N different values from each of K kinetic rate variables such that the range of each variable is divided into N non-overlapping intervals on the basis of equal probability. One value from each interval is selected at random with respect to the assumed probability density in the interval. The N values thus obtained for the first kinetic rate variable are paired in a random manner (equally likely combinations) with the N values of the second kinetic rate variable. These N pairs are combined in a random manner with the N values of the third kinetic rate variable to form N triplets, and so on, until N K-tuplets are formed. These N K-tuplets are the same as the N K-dimensional input vectors where the ith input vector contains specific values of each of the K kinetic rate variables to be used on the ith run of the computer model (Swiler et al 2004).

VI. REFERENCES:

[1] A. A. Cohen, N. Geva-Zatorsky, E. Eden, M. Frenkel-Morgenstern, I. Issaeva, A. Sigal, R. Milo, C. Cohen-Saidon, Y. Liron, Z. Kam, L. Cohen, T. Danon, N. Perzov, U. Alon (2008) Dynamic proteomics of individual cancer cells in response to a drug. Science 322: 1511-6.

[2] Elowitz MB, Levine AJ, Siggia ED, Swain PS (2002) Stochastic gene expression in a single cell. Science 297: 1183-1186.

[3] Swain PS, Elowitz MB, Siggia, ED (2002) Intrinsic and extrinsic contributions to stochasticity in gene expression. Proc Natl Acad Sci 99: 12795-12800.

[4] Blake WJ, Karn M, Cantor CR, Collins JJ (2003) Noise in eukaryotic gene expression. Science 422: 633-637.

[5] Raser JM, O'Shea EK (2005) Noise in gene expression: origins, consequences, and control. Science 309: 2010-2013.

[6] Raser JM, O'Shea EK (2004) Control of stochasticity in eukaryotic gene expression. Science 304: 1811-1814.

[7] Rosenfeld N, Young JW, Alon U, Swain SS, Elowitz MB (2005) Gene regulation at the single-cell level. Science 307: 1962-1965.

[8] Raj A, Perskin CS, Tranchina D, Vargas DY, Tyagi S (2006) Stochastic mRNA synthesis in mammalian cells. PLoS Biology 4: e309.

[9] McAdams HH, Shapiro L (1995) Circuit simulation of genetic networks. Science 269: 650-656.

[10] Arkin A, Ross J, McAdams, HH (1998) Stochastic kinetic analysis of developmental pathways bifurcation in phage λ-infected E. Coli cells. Genetics 149; 1633-1648.

[11] Thattai M, van Oudenaarden A (2001) Intrinsic noise in gene regulatory networks. Proc Natl Acad Sci 98: 8614-8619.

[12] Pedraza JM, van Oudenaarden A (2005) Noise propagation in gene networks. Science 307: 1965-1969.

[13] Lahav G, Rosenfeld N, Sigal A, Geva-Zatorsky N, Levine AJ, Elowitz MB, Alon U (2004) Dynamics of the p53-Mdm2 feedback loop in individual cells. Nat. Genet. 36: 147-150.
[14] Lahav G (2004) The strength of indecisiveness: oscillatory behavior for better cell fate determination. Science STKE 264: pe55-pe58.
[15] Barken D, Wang CJ, Kearns J, Cheong R, Hoffmann A, Levchenko A (2005) Comment on ``oscillations in NF-κB signaling control the dynamics of gene expression". Science 308: 52a.
[16] Nelson DE, Horton CA, See V, Johnson JR, Nelson G, Spiller DG (2005) Response to comments on ``oscillations in NF-κB signaling control the dynamics of gene expression". Science 308: 52b.
[17] Li Q, Verma, IM (2002) NF-κB regulation in the immune system. Nat. Rev. Immunol. 2: 725.
[18] Verma IM, Stevenson J (1997) IκB kinase: beginning, not the end. Proc Natl Acad Sci U S A 94: 11758-11760.
[19] Lee EG, Boone DL, Chai S, Libby SL, Chien M, Lodolce JP, Ma A. (2000) Failure to regulate TNF-induced NF-κB and cell death responses in A20-deficient mice. Science 289: 2350-2354.
[20] Albert B, Bray D, Lewis J, Raff M, Roberts K, Watson, JD (1994) Molecular biology of the cell. New York: Garland Publishing.
[21] Swiler LP, Wyss GD (2004) A user's guide to Sandia's Latin Hypercube smapling software: LHS UNIX library/standalone version. SAND Report: 2004-2439.
[22] Barken, D., Wang, C.J., Kearns, J., Cheong, R., Hoffmann, A., and Levchenko, A., 2005. Comment on ``oscillations in NF-κB signaling control the dynamics of gene expression". Science 308: 52a.
[23] Cheong, R., Bergmann, A., Werner, S., Regal, J., Hoffmann, A., and Levchenko, A., 2006. Transient IκB kinase activity mediates temporal NF-κB dynamics in response to a wide range of tumor necrosis factor-α doses. J. Biol. Chem. 281: 2945-2950.
[24] Covert, M.W., Leung, T.H., Gaston, J.E., and Baltimore, D., 2005. Achieving stability of lipopolysaccharide-induced NF-κB activation. Science 309: 1854-1857.

[25] Hayot, F., Jayaprakash, C., 2006. NF-κB oscillations and cell-to-cell variability. J. Theor. Biol. 240: 583-591.

[26] Hoffmann, A., Levchenko, A., Scott, M.L., and Baltimore, D., 2002. The IκB-NF-κB signaling module: temporal control and selective gene activation. Science 298: 1241-1245.

[27] Hoffmann, A., Baltimore, D., 2006. Circuitry of nuclear factor κB signaling. Immunological Reviews 210:171-186.

[28] Ihekwaba, A.E.C., Broomhead, D.S., Grimley, R.L., Benson, N., and Kell, D.B., 2004. Sensitivity analysis of parameters controlling oscillatory signaling in the NF-κB pathway: the roles of IKK and IκBα. Syst. Biol. 1: 93-103.

[29] Kearns, J.D., Basak, S., Werner, S.L., Huang, C.S., and Hoffmann, A., 2006. IκBε provides negative feedback to control NF-κB oscillations, signaling dynamics, and inflammatory gene expression. J. Chem. Biol. 173: 659-664.

[30] Lahav, G., 2004. The strength of indecisiveness: oscillatory behavior for better cell fate determination. Science STKE 264: pe55-pe58.

[31] Swiler, L.P., Wyss, G.D., 2004. A user's guide to sandia's Latin Hypercube Sampling software: LHS Unix Library/standalone version.

[32] Lipniacki, T., Paszek, P., Brasier, A.R., Luxon, B.A., and Kimmel, M., 2004. Mathematical model of NF-κB regulatory module. J. Theor. Biol. 228: 195-215.

[33] Lipniacki, T., Paszek, P., Brasier, A., Luxon, B.A., and Kimmel, M., 2006. Stochastic regulation in early immune response. Biophys. J. 90: 725-742.

[34] Nelson, D.E., Horton, C.A., See, V., Johnson, J.R., Nelson, G., and Spiller, D.G., 2005. Response to comments on ``oscillations in NF-κB signaling control the dynamics of gene expression". Science 308: 52b.

[35] Nelson, D.E., Ihekwaba, A.E.C., Elliott, M., Johnson, J.R., Gibney, C.A., Foreman, B.E., Nelson, G., See, V., Horton, C.A., Spiller, D.G., Edwards, S.W., McDowell, H.P., Unitt, J.F., Sullivan, E., Grimley, R., BEnson, N., Broomhead, D., Kell, D.B., White, M.R.H., 2004. Oscillations in NF-κB signaling control the dynamics of gene expression. Science 306: 704-708.

[36] Tian, B., Nowak, D.E., and Brasier, A.R., 2005. A TNF-induced gene expression program under oscillatory NF-κB control. BMC Genomics 6: 137-155.

[37] Verma, I.M., Stevenson, J., 1997. IκB kinase: beginning, not the end. Proc. Natl. Acad. Sci. USA 94:11758-11760.

[38] Werner, S.L., Barken, D., and Hoffmann, A., 2005. Stimulus specificity of gene expression programs determined by temporal control of IKK activity. Science 309: 1857-1861.

[39] Brown, K.S., Hill, C. C., Calero, G. A., Myers, C. R., Lee, K. H., Sethna, J. P., and Cerione R. A., 2004. The statistical mechanics of complex signaling networks: nerve growth factor signaling. Phys. Biol. 1: 184-195.

Figure Captions

Figure 1: Biochemical network model for IKK-IκB-NF-κB-A20 signaling module. Top panel: A schematic description of our comprehensive network model of NF-κB signaling. The arrows indicate activation and the perpendicular lines denote inhibition. In the bottom panel, the comprehensive network model consists of IKK (IκB kinase), IκB isoforms (IκB*i*, *i*=α, β, ε), and A20. NF-κBn and IκB*i*n denote their nuclear components. Squares are for proteins and hexagons are for mRNA. Black arrows indicate either association or dissociation or degradation of proteins while red (blue) arrows denote mRNA (protein) synthesis.

Figure 2: Individual time-series curves and their ensemble average of key protein concentrations are obtained from the computer-generated ensemble of 1000 replicates of a wild type NF-κB signaling system. We compare the computational results with the population-level experimental data from Ref. (Hoffmann et al 2002) side by side. Top left panel: nuclear concentration of NF-κB. The other remaining panels: cytoplasmic concentration of IκBα, IκBβ, and IκBε proteins.

Figure 3: Individual time-series curves and their ensemble average of key protein concentrations are obtained from the computer-generated ensemble consisting of 1000 replicates of a IκB double gene knocked-out mutant. Computational simulation results (left column) are compared with the population-level experimental data (right column) from Ref. (Hoffmann et al. 2002). Top panel: IκBβ and IκBε knocked-out mutant. Mid panel: IκBα and IκBβ knocked-out mutant. Bottom panel: IκBα and IκBε knocked-out mutant.

Figure 4: Individual time-series curves and their ensemble average of key protein concentrations are obtained from the computer-generated ensemble consisting of 1000 replicates of a wild type (right column) and a A20 knocked-out mutant (left column). Computational simulation results are compared with the population-level experimental

data from Ref. (Lee et al 2000) side by side. Top panels: nuclear concentration of NF-κB. Bottom panel: IKK concentration. Other key biochemical species profiles are presented in supporting figure 1.

Figure 5: Dependence of the individual time-series curves and the statistical ensemble average of nuclear NF-κB profiles obtained from IκBβ and IκBε genes knocked-out mutant on the heterogeneity measure χ (i.e., the interval size of the uniform distribution). χ=10 % for top left panel; χ=30 % for top right panel; χ=50 % for bottom left panel; χ=70 % for bottom panel.

Figure 6: Distributions of six dynamic features of nuclear NF-κB profiles are obtained from the ensemble of 1,000 replicates of a wild type (black), A20 knocked-out mutant (red), and three IκB double genes knocked-out mutants (blue, yellow, and green). The six dynamic features are the amplitude of the first peak (First Maximum), the timing of the first peak (First Translocation Time), the First Period, the First Minimum, the Second Maximum, and the Steady State: The last three values are normalized by the First Maximum.

Figure 7: Distributions of the dynamic patterns of the individual time-series curves of nuclear NF-κB profiles are obtained from the ensemble of 1,000 replicates of a wild type, A20 knocked-out mutant, and three IκB double genes knocked-out mutants. Top panel demonstrates four dynamic patterns: (A) single-peaked pattern, (B) under-damped oscillation, (C) hyperbolic pattern, and (D) sustained oscillation. Each individual time-series curve is classified into one of four dynamic patterns.

Figure 8: Individual time-series curves and their ensemble average of the key protein concentrations are obtained from the computer-generated ensemble consisting of 1000 replicates of a wild type system upon stimulation by small dosage (left column) or large dosage (right column).

Figure 9: Distributions of six dynamic features of nuclear NF-κB profiles are obtained

from the ensemble of 1,000 replicates of a wild type NF-κB signaling system with a small (red color; TR=0.01) or large (black-color; TR=1) dosage stimulation.

Figure 10: Distribution of the dynamic patterns of nuclear NF-κB profiles from the ensemble of 1,000 replicates of a wild type NF-κB signaling system upon a small (TR=0.01) or a large (TR=1) dosage stimulation. Yellow denotes sustained oscillation; red for damped oscillation; blue for single-peaked pattern.

Figure 11: The individual dose-response curves and their statistical ensemble average from the ensemble consisting of 50 computer-generated replicates of a wild type NF-κB signaling system.

Supporting Figure 1: Individual time-series curves and their ensemble average of key protein concentrations are obtained from the computer-generated ensemble consisting of 1000 replicates of a wild type (right column) and a A20 knocked-out mutant (left column). Computational simulation results are compared with the population-level experimental data from Ref. (Lee et al 2000) side by side. Top panels: cytoplasmic concentration of IκBα protein. Mid panel: concentration of IκBα mRNA. Bottom panel: A20 protein concentration.

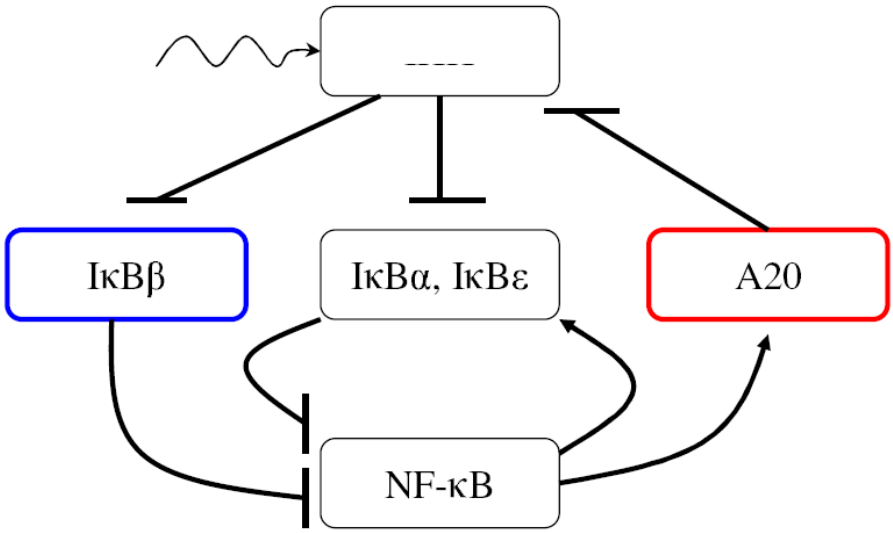
IκBβ
IκBα, IκBε
A20
NF-κB

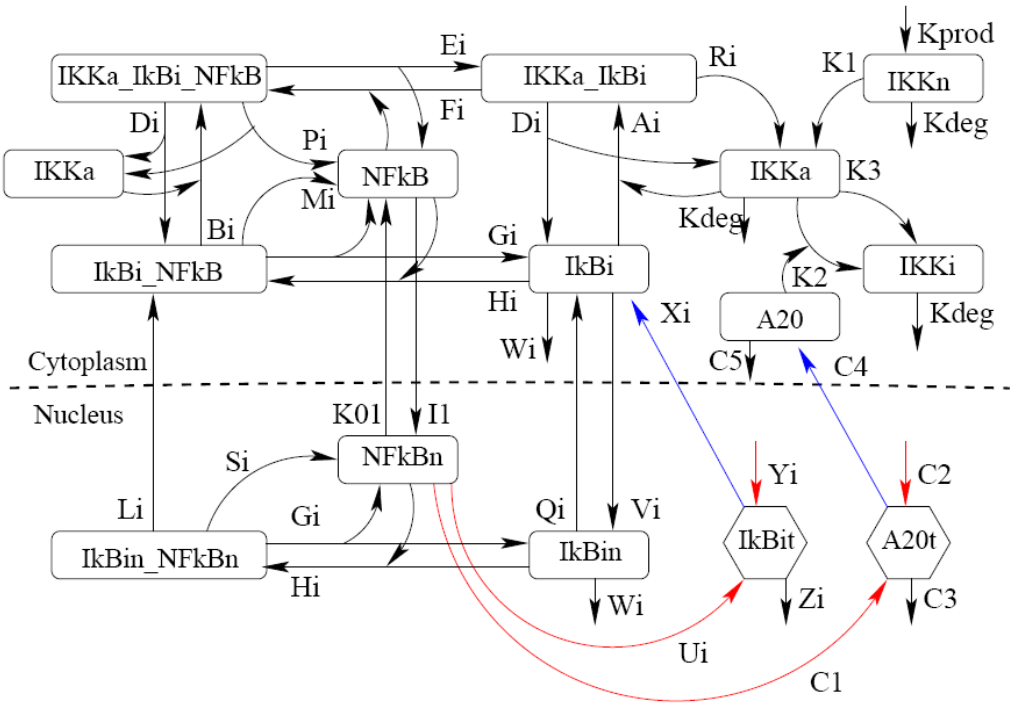
Kprod
Ei
Ri
K1
IKKa_IkBi_NFkB
IKKa_IkBi
IKKn
Fi
Di
Di
Ai
Kdeg
Pi
IKKa
NFkB
IKKa
K3
Mi
Kdeg
Bi
Gi
IkBi_NFkB
IkBi
IKKi
K2
Hi
Xi
A20
Kdeg
Wi
C5
C4
Cytoplasm
Nucleus
K01
I1
NFkBn
Si
Yi
C2
Li
Gi
Qi
Vi
IkBit
A20t
IkBin_NFkBn
IkBin
Hi
Wi
Zi
C3
Ui
C1

Figure 1

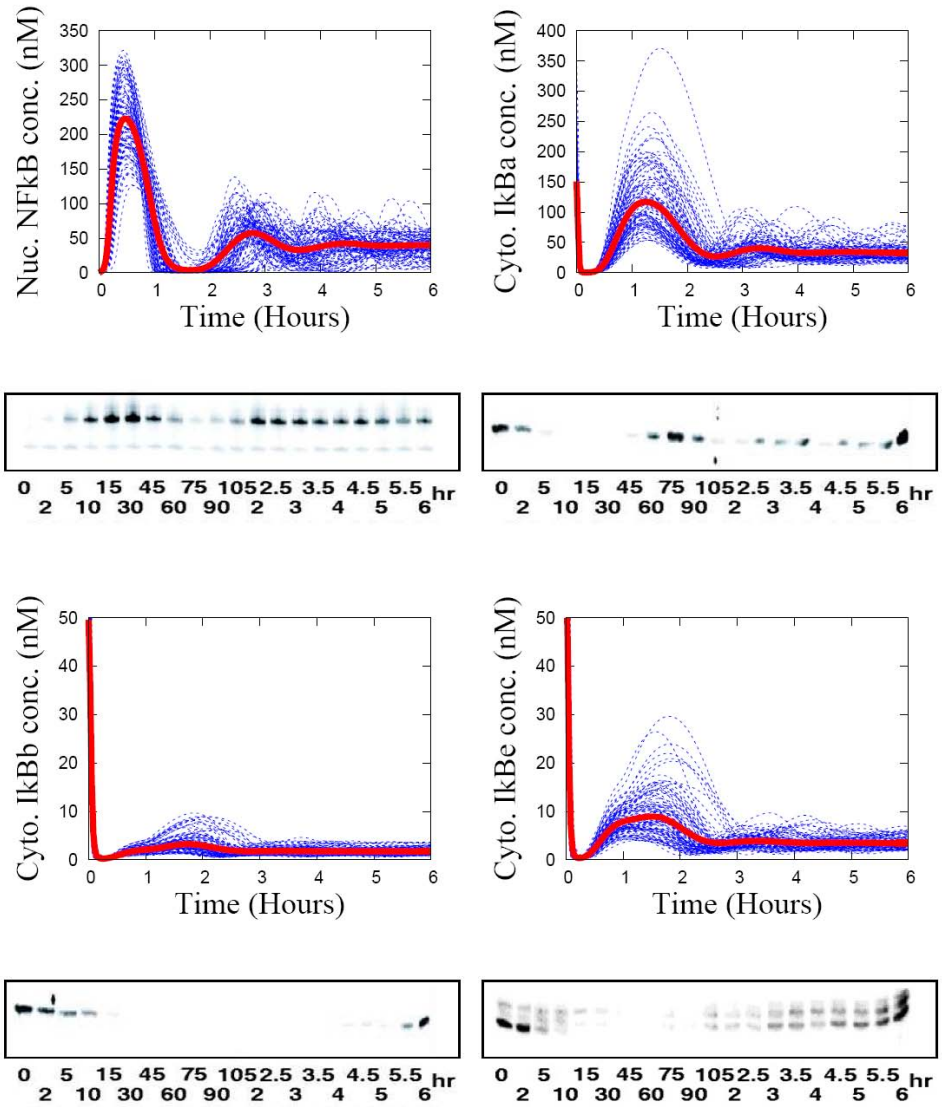
Nuc. NFkB conc. (nM)
Time (Hours)
Cyto. IkBa conc. (nM)
Time (Hours)
0 5 15 45 75 105 2.5 3.5 4.5 5.5 hr
2 10 30 60 90 2 3 4 5 6
Cyto. IkBb conc. (nM)
Time (Hours)
Cyto. IkBe conc. (nM)
Time (Hours)

Figure 2

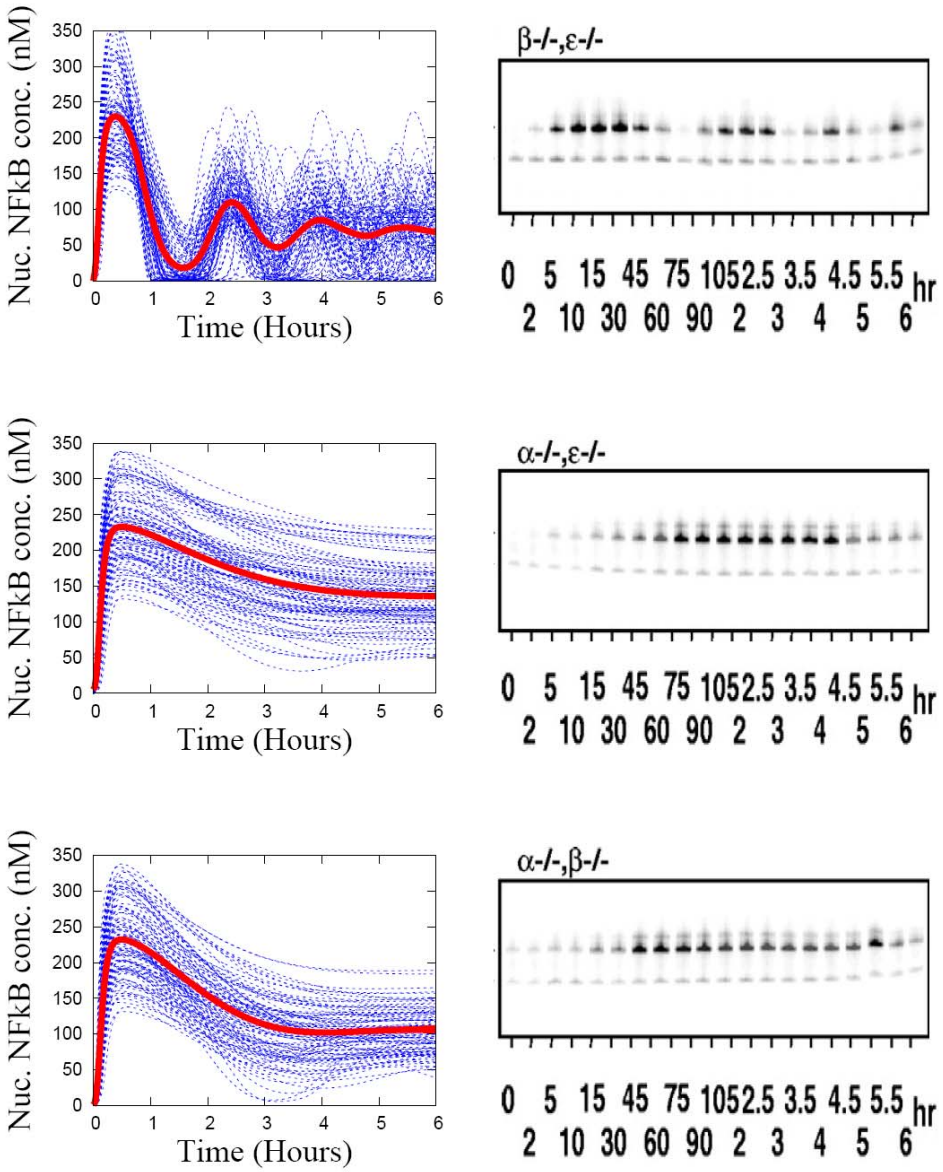
Nuc. NFkB conc. (nM)
Time (Hours)
β-/-,ε-/-
α-/-,ε-/-
α-/-,β-/-
0 5 15 45 75 105 2.5 3.5 4.5 5.5 hr
2 10 30 60 90 2 3 4 5 6

Figure 3

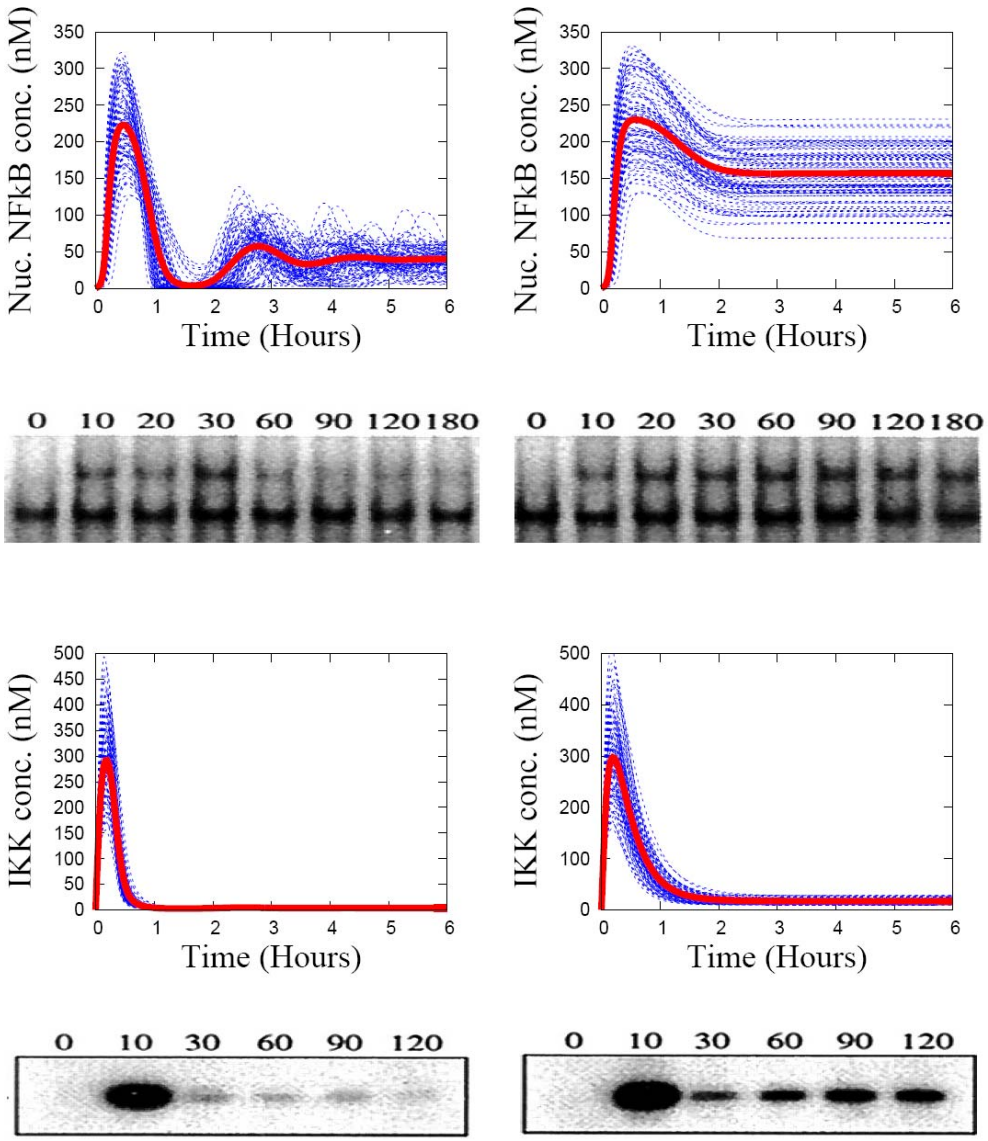
Nuc. NFkB conc. (nM)
Time (Hours)
0 10 20 30 60 90 120 180
IKK conc. (nM)
0 10 30 60 90 120

Figure 4

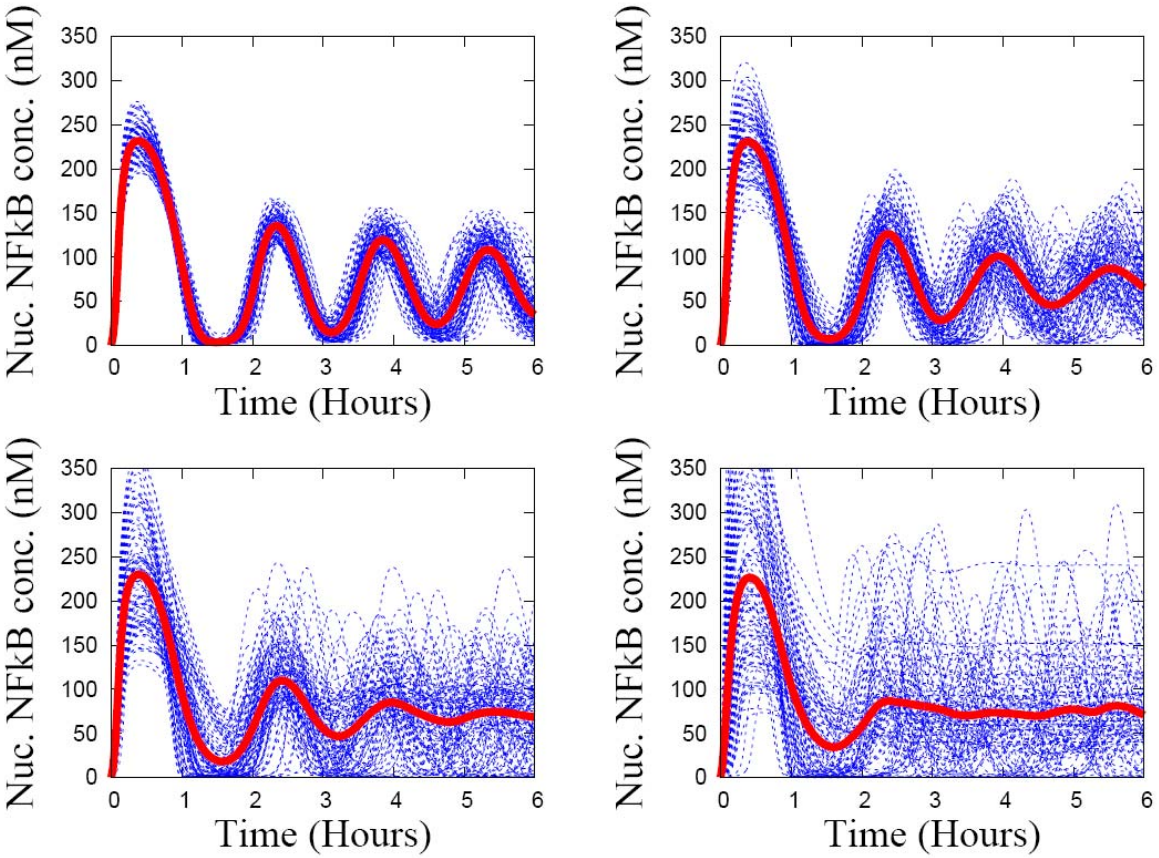
Nuc. NFkB conc. (nM)
Time (Hours)
0
50
100
150
200
250
300
350
0
1
2
3
4
5
6

Figure 5

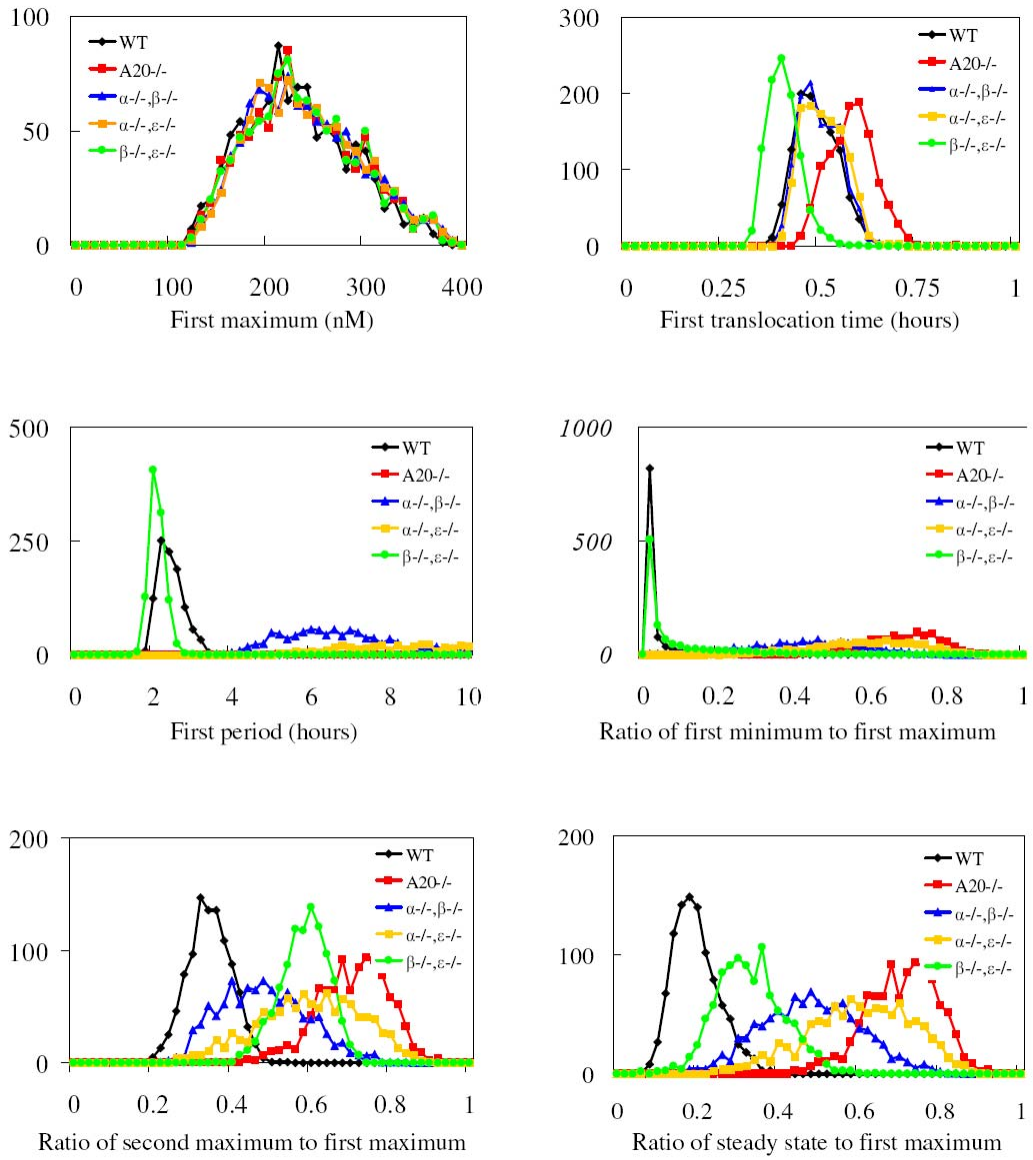
WT
A20-/-
α-/-,β-/-
α-/-,ε-/-
β-/-,ε-/-
First maximum (nM)
First translocation time (hours)
First period (hours)
Ratio of first minimum to first maximum
Ratio of second maximum to first maximum
Ratio of steady state to first maximum

Figure 6

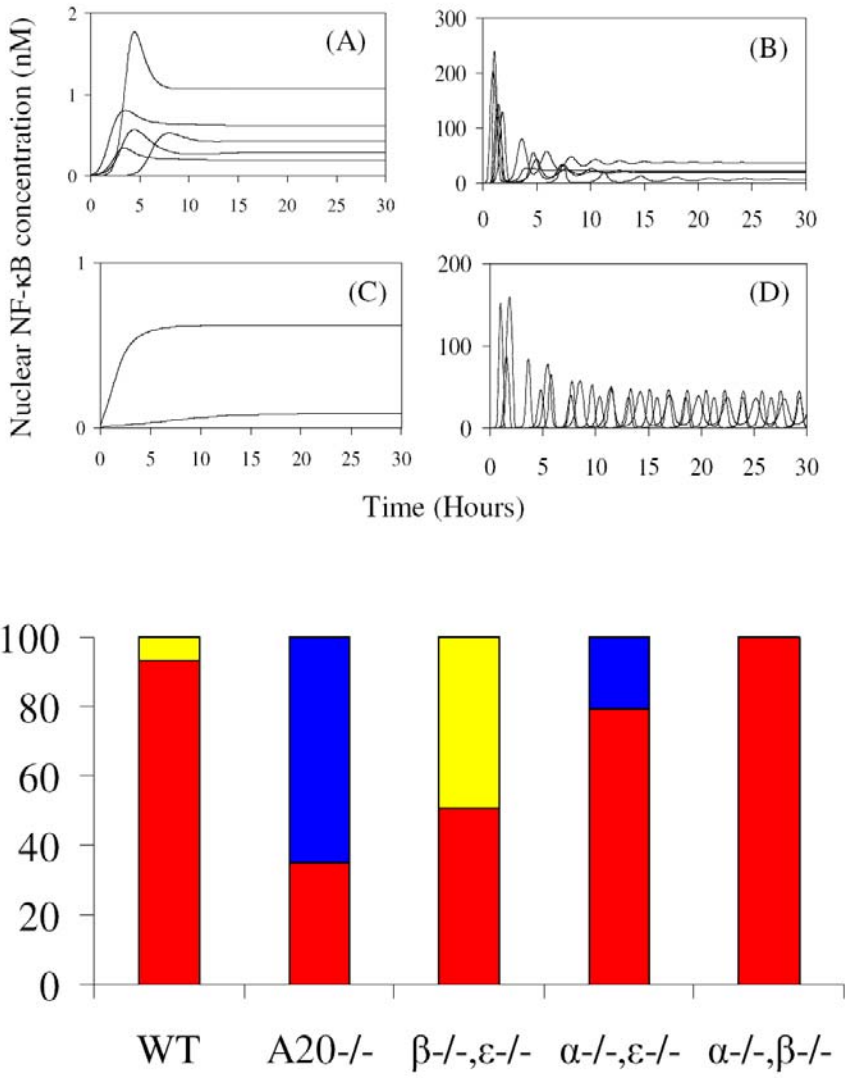
Nuclear NF-κB concentration (nM)
(A)
(B)
(C)
(D)
Time (Hours)
WT
A20-/-
β-/-,ε-/-
α-/-,ε-/-
α-/-,β-/-

Figure 7

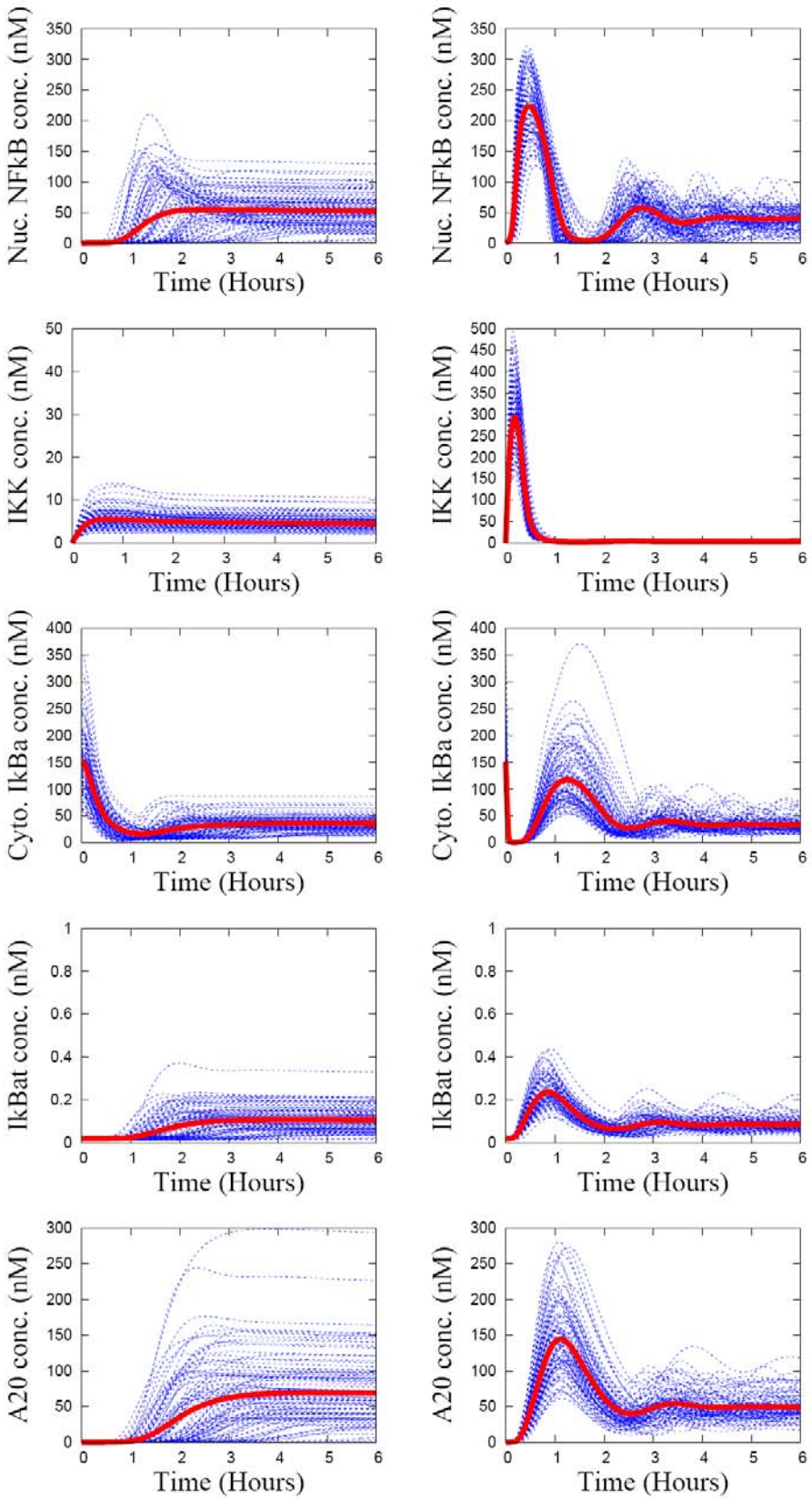
Nuc. NFkB conc. (nM)
Time (Hours)
Nuc. NFkB conc. (nM)
Time (Hours)
IKK conc. (nM)
Time (Hours)
IKK conc. (nM)
Time (Hours)
Cyto. IkBa conc. (nM)
Time (Hours)
Cyto. IkBa conc. (nM)
Time (Hours)
IkBat conc. (nM)
Time (Hours)
IkBat conc. (nM)
Time (Hours)
A20 conc. (nM)
Time (Hours)
A20 conc. (nM)
Time (Hours)

Figure 8

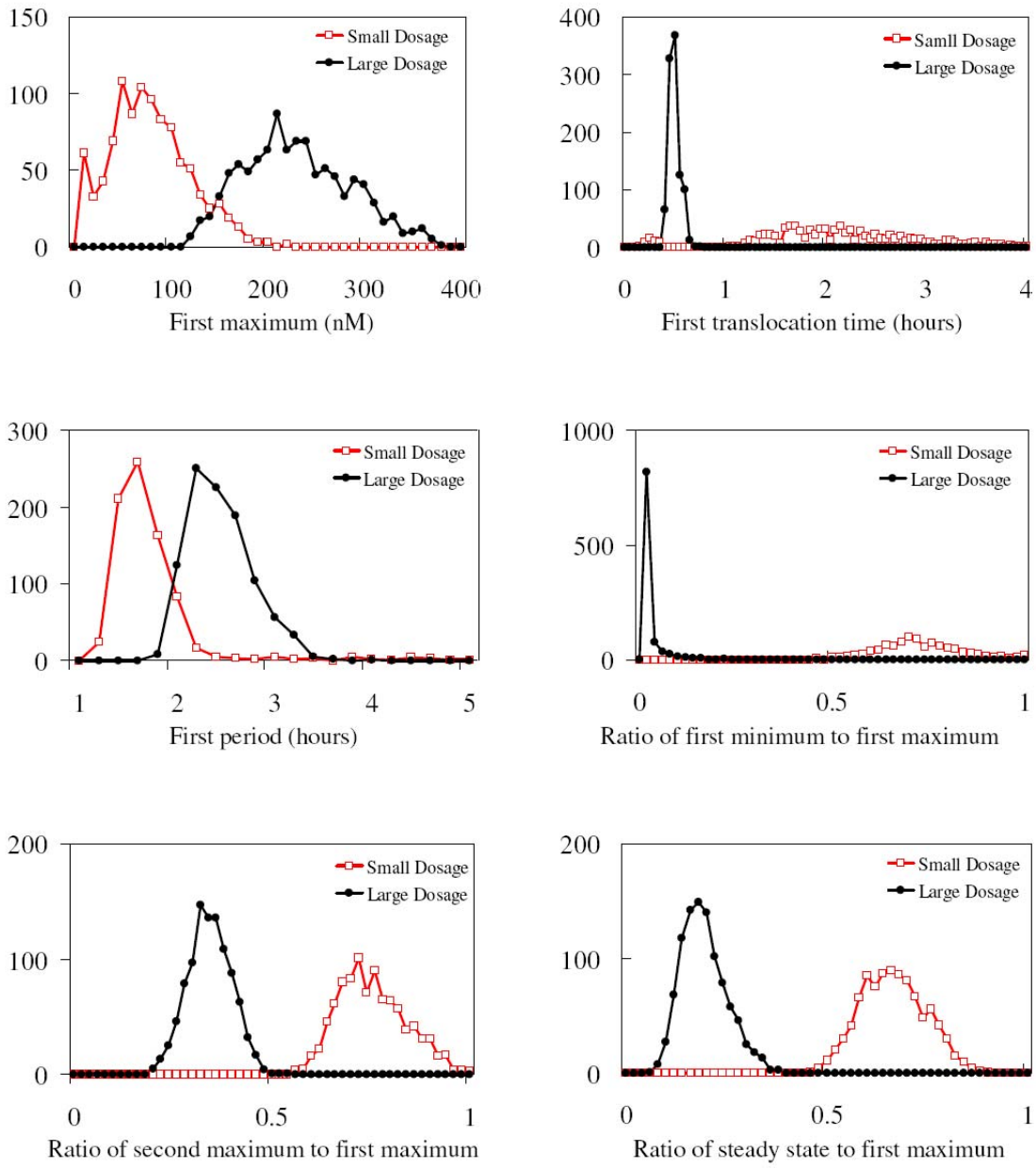
150
100
50
0
0
100
200
300
400
First maximum (nM)
Small Dosage
Large Dosage
400
300
200
100
0
0
1
2
3
4
First translocation time (hours)
Samll Dosage
Large Dosage
300
200
100
0
1
2
3
4
5
First period (hours)
Small Dosage
Large Dosage
1000
500
0
0
0.5
1
Ratio of first minimum to first maximum
Small Dosage
Large Dosage
200
100
0
0
0.5
1
Ratio of second maximum to first maximum
Small Dosage
Large Dosage
200
100
0
0
0.5
1
Ratio of steady state to first maximum
Small Dosage
Large Dosage

Figure 9

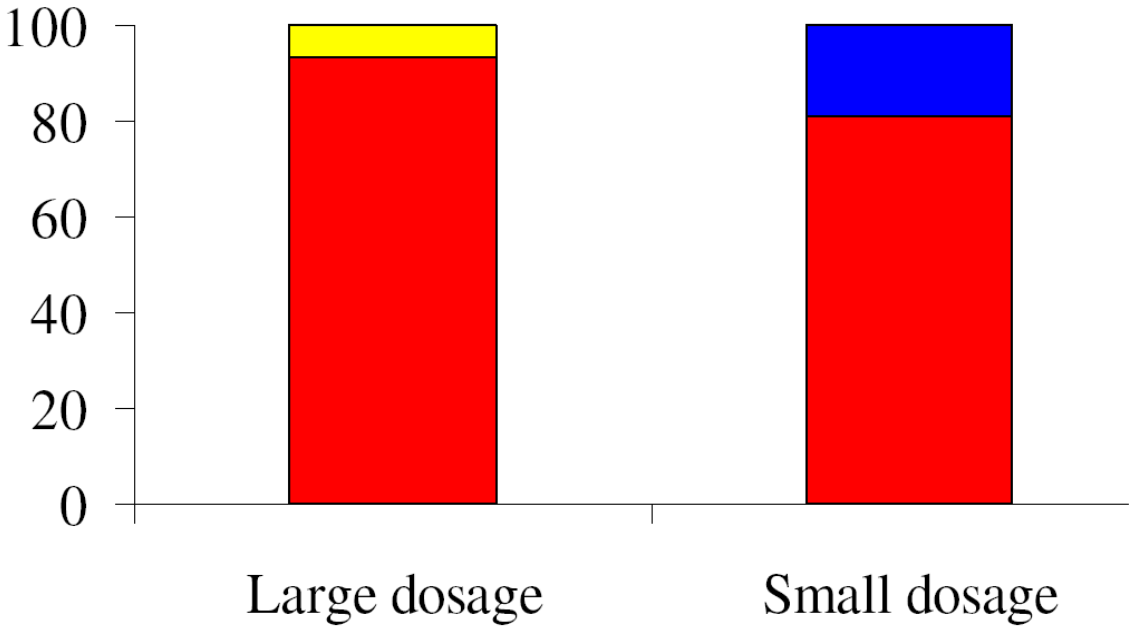

Figure 10

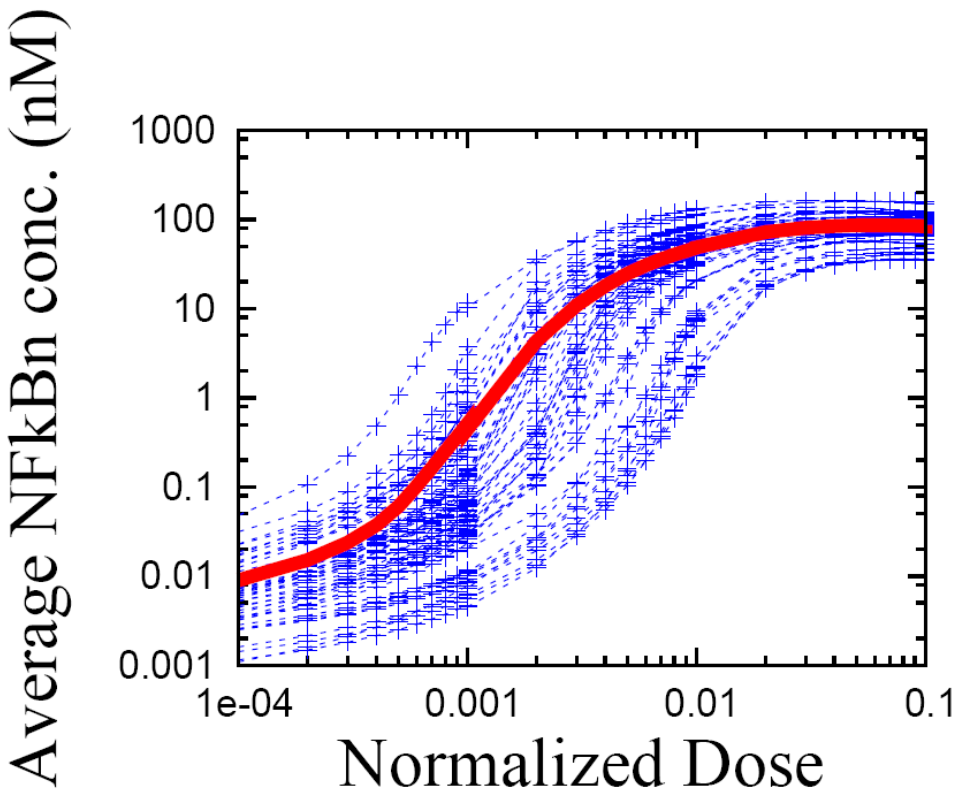

Figure 11

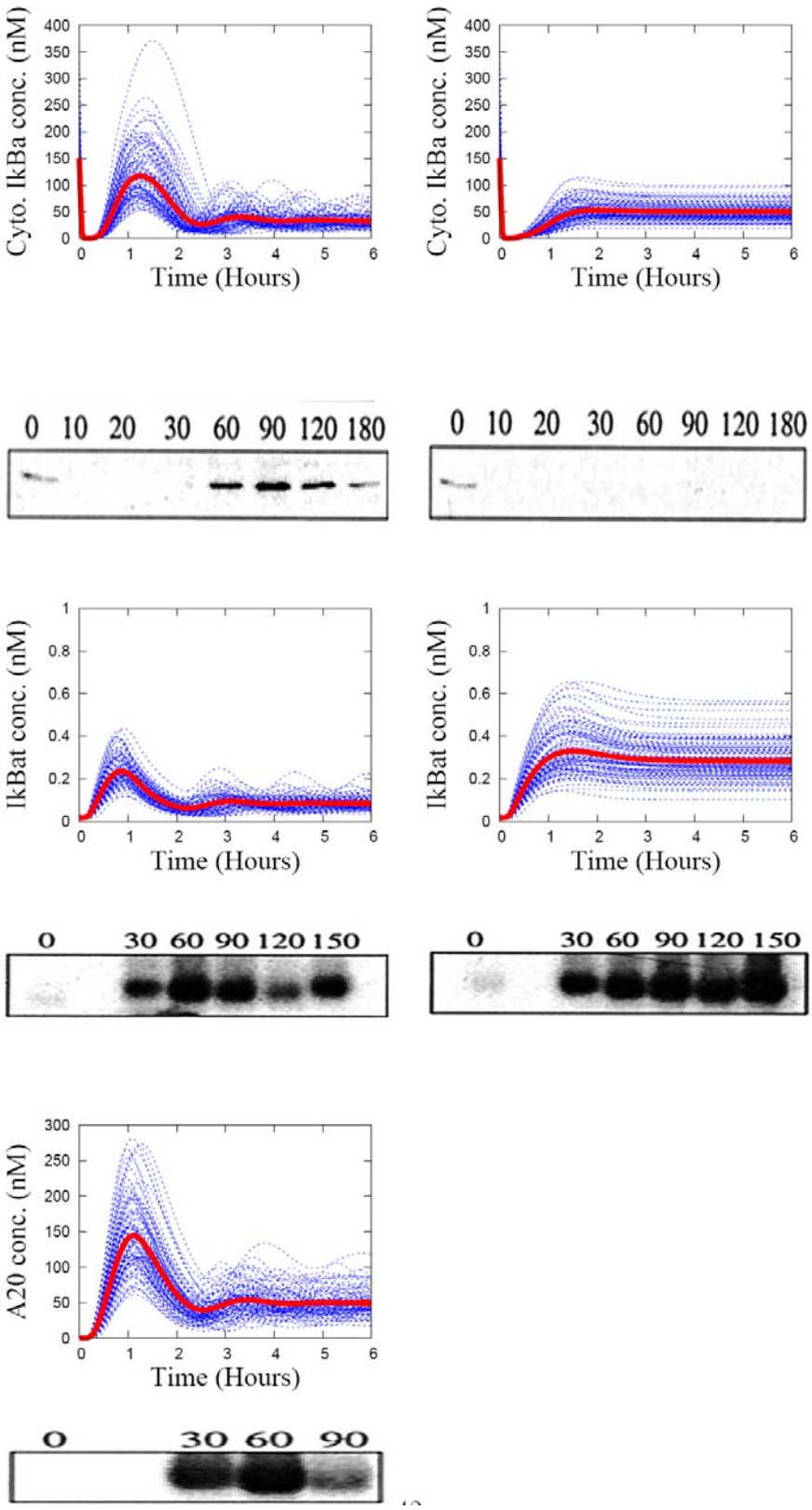

Supporting Figure 1

7. Different lipopolysaccharide chemotypes provoke a common Toll-like receptor 4 mediated response to different degrees.

Zhaoduo Zhang, Meiye Wu, Stephanie Morrison, Julie Kaiser, Nimisha Srivastava, Catherine S. Branda, Todd W. Lane, Bryan Carson, Jens Poschet, Tony Martino, Anup Singh, and Steven S. Branda

Abstract

Innate immune response to a pathogenic challenge is shaped by specificity determinants including pathogen recognition receptor (PRR) sensitivity to stimulation by different pathogen-associated molecular patterns (PAMPs). For example, Toll-like receptor 4 (TLR4) mediated responses vary with the molecular composition of the lipopolysaccharide (LPS) ligands that elicit them. Whether these responses differ only in *degree*, or also in *type*, is an unresolved issue that holds important implications for our understanding of TLR4-mediated signal transduction and, more broadly, the molecular mechanisms imparting specificity to the innate immune system. To address this issue, we carried out a systematic and comprehensive analysis of TLR4-mediated responses to different doses and chemotypes of LPS. By monitoring activation of many key nodes in the TLR4 signaling network, as well as production of many cytokines, we found that different LPS chemotypes elicit a TLR4-mediated response to different degrees, but that the essential nature of the response is conserved. These findings reinforce the view that different LPS chemotypes stimulate TLR4-mediated response through a common mechanism, and that the observed specificity in response stems from differences in signal strength.

Introduction

The innate immune system is primarily responsible for initiating host defense responses against pathogens. Sentry cells such as macrophages recognize pathogens through use of pattern recognition receptors (PRRs), which detect pathogen-associated molecular patterns (PAMPs) characteristic of particular classes of pathogen [J Clin Immunol 25:503; Mol Cells 23:1]. Activation of a PRR sets in motion a signal transduction cascade, typically leading to upregulated production of effector proteins such as pro-inflammatory enzymes, costimulatory molecules, and secreted signaling molecules (hereafter referred to broadly as "cytokines"). Induction of these responses is essential not only for early protection against infection [Cell Microbiol 9:1891], but also for encouraging development of adaptive immunity [Clin Exp Immunol 147:199; Sci STKE 402:pe48; Nature 438:364].

Often described as the "non-specific" counterpart to adaptive immunity, the innate immune system may in fact recognize and combat pathogens with heretofore unsuspected specificity. Recent discoveries of "new" PRRs and cognate PAMPs underscore the possibility that, as a rule, pathogens bear several different PAMPs and are recognized combinatorially, through integration of multiple PRR-induced signals [Crit Rev Immunol 22:217; J Clin Invest 118:413; Curr Opin Immunol 19:10]. Furthermore, an additional level of specificity is implied in the observation that different PAMPs acting on a common PRR can elicit different innate immune responses [Annu Rev Immunol 21:335; Clin Exp Immunol 140:395; PNAS 99:1503]. While both of these potential specificity determinants have garnered considerable attention, thus far only the latter has been characterized in some detail. In particular, several groups have investigated the specificity with which variants of lipopolysaccharide (LPS), a bacterial PAMP, elicit innate immune responses *via* activation of Toll-like receptor 4 (TLR4), its cognate PRR.

LPS, the major structural component of the outer membrane of Gram-negative bacteria, is a complex macromolecule consisting of three covalently linked domains: a distal segment comprised of a repeating, highly variable oligosaccharide (O-antigen) which is immunogenic; a middle segment comprised of a much shorter, non-repeating, more conserved oligosaccharide (core); and a proximal segment comprised of a glycolipid (lipid A) which anchors the LPS to the external surface of the bacterial outer membrane [Annu Rev Biochem 71:635]. The precise composition of LPS varies between different species and strains of bacteria [J Endotoxin Res 12:205], and can vary even within pure cultures [J Biol Chem 274:16819; J Biol Chem 275:28006; FEBS Lett 499:1; Infect Immun 72:5041]. In fact, certain bacteria are capable of expressing different chemotypes of LPS in response to changes in environmental conditions [Science 276:250; Science 286:1561; Biochem 44:1731; Infect Immun 70:4092; Mol Microbiol 52:1363].

It is well established that different LPS chemotypes can provoke different innate immune responses [J Endotoxin Res 7:167]. Indeed, even seemingly subtle modifications to LPS - changes in lipid A phosphorylation or acylation patterns, for example - can dramatically alter its immunobiological activity. In some instances pathogens appear to take advantage of this phenomenon, expressing "non-stimulatory" LPS and thereby evading recognition by the innate immune system [J Endotoxin Res 12:205; Ann N Y Acad Sci 1105:202; Infect Immun 70:4092; Mol Microbiol 52:1363]. The significance of this virulence strategy is evident in the fact that *Yersinia pestis*, the causitive agent of the plague, can be rendered avirulent simply by forcing it to constitutively express a "stimulatory" chemotype of LPS [Nat Immunol 7:1066]. Because of its implications for host-pathogen interactions, including the development of sepsis [Int J Med Microbiol 297:365], the relationship between LPS composition and immunobiological activity has been studied extensively. With the identification of TLR4 as the PRR responsible for

host recognition of LPS [Blood Cells Mol Dis 24:340; Science 282:2085], there has been equally intense interest in elucidating the relationship between LPS composition and efficacy in activating the TLR4-mediated signaling pathway. Not surprisingly, such studies generally have found that LPS chemotypes of high immunobiological activity strongly induce activation of the TLR4 signaling network, whereas "non-stimulatory" LPS chemotypes do not [*e.g.*, Int Immunol 16:1467; Int Immunol 18:785; Infect Immun 73:2940; Nat Immunol 7:1066]. The simplest explanation for these observations is that "stimulatory" LPS chemotypes engage the TLR4 receptor complex productively whereas "non-stimulatory" LPS chemotypes do not, and this difference is maintained at the level of TLR4 network activation and induction of innate immune responses. However, it is also possible that "stimulatory" LPS chemotypes engage the TLR4 network in a categorically different way, and that this is reflected in differences in TLR4 network activation and innate immune response. Each of these models draws some support from published observations. For instance, Duanas *et al.* reported that "stimulatory" LPS (derived from *E. coli*) induced a TLR4 network response virtually identical to that induced by 500-fold higher concentrations of "non-stimulatory" LPS (derived from *F. tularensis holarctica* LVS) [Int Immunol 18:785]. In contrast, Zughaier *et al.* reported that matched doses of different LPS chemotypes (derived from a variety of bacteria) induced markedly different TLR4 network responses [Infect Immun 73:2940]. Unfortunately, neither study provides sufficient evidence to convincingly support one model at the expense of the other; too few LPS doses were tested, too few TLR4 network nodes were assessed, and consequently the results may be explained by either model.

In order to determine whether different LPS chemotypes elicit innate immune responses that differ only in *degree*, or also in *type*, we carried out a systematic and comprehensive analysis of TLR4-mediated responses to different doses and chemotypes of LPS. By monitoring activation of many key nodes in the TLR4 signaling network, as well as

production of many cytokines, we found that different LPS chemotypes elicit TLR4-mediated response to different degrees, but that the essential nature of the response is conserved. These findings support the idea that different LPS chemotypes stimulate TLR4-mediated responses *via* a common signal transduction mechanism, and that specificity in response is simply a manifestation of differences in signal strength.

Materials and Methods

Cell Culture

The murine macrophage cell line RAW264.7 (TIB-71) was obtained from American Type Culture Collection (ATCC). RAW264.7 cells were maintained in DMEM supplemented with 10% FBS (Gemini Bio-Products), 2 mM glutamine (Invitrogen), and 20 mM HEPES (Invitrogen) [*i.e.*, RAWGM1, as *per* Alliance for Cell Signaling (AfCS) Solution Protocol PS00000510 (http://www.signaling-gateway.org/data/ProtocolLinks.html)], at 5% CO_2 and 37°C. For routine passaging the cells were grown on non-treated disposable tissue culture vessels and harvested through brief exposure to EDTA (Versene solution; Invitrogen), as *per* AfCS Procedure Protocol PP00000159).

Francisella tularensis subspecies *novicida* strain Utah 112 (NR-13) was obtained from BEI Resources (Manassas, VA). *F. tularensis* subsp. *novicida* cells were maintained in tryptic soy broth (BBL 211768) supplemented with 0.1% L-cysteine, at 37°C with shaking at 250 rpm.

Purification of Bacterial Lipopolysaccharides (LPS)

LPS was extracted from *F. tularensis* subsp. *novicida* cells using a protocol based upon that described by Darveau and Hancock [J Bacteriol 155:831]. Cells were harvested from 12 L overnight cultures through centrifugation, washed once with 10 mM Tris-HCl pH 8 + 2 mM $MgCl_2$, and resuspended in 175 ml of 10 mM Tris-HCl pH 8 + 2 mM $MgCl_2$ + 100 μg/ml DNase I (Sigma-Aldrich DNEP) + 25 μg/ml RNase A (Sigma-Aldrich R4875) for incubation at 4°C for 16 h. The cells were then lysed using an EmulsiFlex-C5 (Avestin), and DNase I and RNase A were added to 100 μg/ml and 25 μg/ml, respectively, for incubation at 37°C for 2 h. Stock solutions of 500 mM EDTA and 20% SDS in 10 mM Tris-HCl pH 8 were added to the cell lysate for final concentrations of

100 mM and 2%, respectively, and the mixture centrifuged at 50,000 x *g* at 20°C for 30 min. The cleared supernatant (~570 ml) was transferred to a clean flask, and proteinase E (Sigma-Aldrich 81748) was added to a final concentration of 200 μg/ml, for incubation at 37°C with shaking at 150 rpm for 16 h. The preparation was then split into two aliquots for precipitation of LPS, in order to reduce the risk of co-precipitation of SDS. Each aliquot was combined with two volumes of freshly made 375 mM $MgCl_2$ in 95% ethanol, and was cooled to 0°C in a frozen ethanol bath. The aliquots were then centrifuged at 12,000 x *g* at 0°C for 15 minutes, and the LPS pellets resuspended in 10 mM Tris-HCl pH 8 + 100 mM EDTA + 2% SDS, and combined for a total volume of 650 ml. LPS aggregates were further dispersed through two rounds of sonication (1 min each), the pH was adjusted to 7 through addition of NaOH, and the sample incubated at 85°C for 30 min, in order to ensure denaturation of detergent-resistant proteins. After cooling to RT, the pH was re-adjusted to 9.5 through addition of NaOH, proteinase E was added to 25 μg/ml, and the sample incubated at 37°C with shaking at 150 rpm for 16 h. LPS was precipitated and pelleted as before, the combined pellets resuspended in 500 ml of 10 mM Tris-HCl pH 8, and the sample sonicated as before. Mg-EDTA precipitates were removed from the sample by centrifugation at 1000 rpm for 5 min, and $MgCl_2$ was added to the transferred supernatant for a final concentration of 25 mM. Finally, purified LPS was harvested from the sample through centrifugation at 200,000 x *g* at 20°C for 2 h; the clear, waxy LPS pellets were resuspended in endotoxin-free water and lyophilized for storage at -20°C.

Phospholipids were removed from the *F. tularensis* subsp. *novicida* LPS using a modified Folch extraction method [REF]. The lyophilized LPS was resuspended in 2:1 chloroform:methanol to a final concentration of 2% (w/v) and then centrifuged at 10,000 rpm at 4°C. After two rounds of extraction the LPS pellet was air-dried for storage at -20°C.

Lipoprotein contaminants were removed from our preparations of *F. tularensis* subsp. *novicida* "smooth" LPS, as well as from commercial preparations of *Escherichia coli* O55:B5 "smooth" LPS (Sigma-Aldrich L-4524) and *Salmonella minnesota* Re 595 "rough" LPS, using a standard phenol extraction method [J Immunol 165:618]. LPS samples were resuspended at 5 mg/ml in endotoxin-free water containing 0.2% triethylamine, and sodium deoxycholate was added for a final concentration of 0.5%. Then, an equal volume of water-saturated phenol was added, and the mixture vortexed intermittently at RT for 5 min, followed by incubation on ice for 5 min. After centrifugation at 10,000 x *g* at 4°C for 2 min, the aqueous phase was carefully transferred to a new tube and set aside. To the organic phase an equal volume of 0.2% triethylamine + 0.5% sodium deoxycholate was added, and the extraction procedure was repeated. After combining the aqueous phase samples, an equal volume of water-saturated phenol was added, and the extraction procedure was repeated for a third time. Each of the final aqueous phase samples were mixed with 2.75 volumes of 100% ethanol and 0.01 volume of 3 M sodium acetate, the samples incubated at -20°C for at least 1 h, and the precipitated LPS harvested through centrifugation at 10,000 x *g* at 4°C for 10 min. The LPS pellets were washed once with cold 100% ethanol and then air-dried for storage at -20°C.

LPS Quantitation by KDO Assay

LPS preparations were assessed for KDO content as a measure of LPS concentration, using a colorimetric assay and protocol based on that described by Karkhanis *et al.* [Anal Biochem 85:595]. Small (50 µl) aliquots of LPS samples and KDO standards were mixed with equal volumes of 0.036 N H_2SO_4 and boiled for 20 min in sealed screw-cap microcentrifuge tubes. After cooling to RT, 25 µl of periodate reagent (0.04 M $NaIO_4$ in 0.125 N H_2SO_4) was added to each tube, and the mixture incubated at RT in the dark.

After 20 min, 50 µl of arsenite reagent (2.6% $NaAsO_2$ in 0.5 N HCl) were added to each tube, causing the mixture to transiently develop a brown hue. Upon becoming colorless once again, each sample was mixed with 250 µl of 0.3% thiobarbituric acid (Sigma-Aldrich), vortexed, and incubated at 100°C for 10 min. To the hot mixure 125 µl of dimethyl sulfoxide was added, the tube vortexed, and after cooling OD_{550} was measured. Buffer served as the blank, and dilutions (31.25 µM to 500 µM) of purified KDO (Sigma-Aldrich) were used to generate a standard curve.

LPS Challenge of Macrophages and Sample Preparation for Western Analysis and ELISA

RAW264.7 cells were harvested as usual, introduced to fresh RAWGM1 medium, and then used to seed 10 cm diameter tissue-culture-treated petri dishes (BD Biosciences #35305) at a density of $3x10^6$ cells/dish. After 24 h of growth, the conditioned medium (10 ml) was removed for replacement with 9 ml of fresh RAWGM1, and the cultures were allowed to equilibrate at 5% CO_2 and 37°C for at least 1 h. LPS challenge was initiated upon addition of 1 ml of thoroughly-suspended LPS in RAWGM1 and immediate mixing by rapid but gentle swirling of the petri dish. After further incubation at 5% CO_2 and 37°C for a pre-determined amount of time, the conditioned medium of each culture was transferred to a 15 ml Falcon tube on ice; these samples were soon thereafter centrifuged at 400 x *g* for 5 min in order to pellet any contaminating cells, and the supernatants transferred to new tubes for storage at -80°C and eventual profiling of cytokine content. Upon removal of the conditioned medium 500 µl of 1.5X SBCe sample buffer [AfCS Solution PS00000533] were immediately added to the petri dish, and the adherent cells contained therein were harvested through use of a cell scraper and P-1000 Pipetman. Each sample was immediately transferred to a locking-lid microcentrifuge tube, incubated at 100°C for 5 min, and then stored at -80°C for eventual use in Western analysis experiments.

Western Analysis

10 μl aliquots of each sample, and 10 μl of SeeBlue Plus2 protein standard ladder (Invitrogen), were loaded into the wells of a Novex 4-20% Tris-Glycine Midi gel (Invitrogen). After electrophoresis at 150V for ~90 min, proteins were transferred from the gel to a nitrocellulose membrane using the iBlot system (Invitrogen). The membrane was then incubated in blocking buffer (5% (w/v) powdered milk in TBS/T) at RT with gentle agitation for 1 h, washed three times with TBS/T, and incubated with a primary antibody of interest, diluted appropriately in 5% BSA (Sigma) in TBS/T, at 4°C with gentle agitation for 16 h. The membrane was then washed three times with TBS/T, and incubated with an appropriate HRP-conjugated secondary antibody (GE Healthcare), diluted 1:200 in 5% powdered milk in TBS/T, at RT for 2 h. The wash steps were repeated, and the membrane was exposed to ChemiGlow reagent (AlphaInnotech) for 2 min before detection using an AlphaImager (AlphaInnotech).

ELISA

Conditioned media harvested from LPS-challenged RAW264.7 cell cultures were assessed for cytokine content using ELISA kits (R&D Systems) designed to specifically detect murine cytokines TNFα, RANTES, IP10, MCP5, G-CSF, IL1β, MCP1, MIP2, and MIP1β. In many cases the samples required appropriate dilution with RAWGM1 in order to reduce cytokine levels to fall within the working range of the assay.

Flow Cytometry

RAW264.7 cells were harvested as usual, introduced to fresh RAWGM1 medium, and then used to seed ultra-low attachment petri dishes (Corning #3262) or low-attachment 96-well microtiter plates (Corning #3474), at a density of 10^6 cells/dish. After equilibration at 5% CO_2 and 37°C for at least 2 h, LPS challenge was initiated upon

addition of X ml of thoroughly-suspended LPS in RAWGM1. After further incubation at 5% CO_2 and 37°C for a pre-determined amount of time, the cells were fixed upon addition of paraformaldehyde (Electron Microscopy Sciences) to a final concentration of 1-2% and incubation at RT for 10 min. The fixed cells were harvested by centrifugation at 400 x *g* at 4°C for 5 min and washed twice with BD stain buffer with BSA (BD Biosciences #554657) prior to downstream processing.

For detection of surface-exposed, non-activated TLR4-MD2 receptor complex, 2.5×10^5 fixed cells were resuspended in 25 ul of BD stain buffer containing 5 μg/ml (1:20) of PE-labeled MTS510 antibody (Abcam ab21319), and incubated in the dark at 4°C for 45 min. The cells were then washed twice with BD stain buffer, harvested by centrifugation at 300 x *g* for 5 min, resuspended in 200 μl of BD stain buffer, and the fluorescence intensity measured using a BD FACScan flow cytometer.

For detection of intracellular proteins of interest, fixed and washed RAW 264.7 cells were permeabilized through resuspension in cold methanol to a final concentration of 10^6 cells/ml and incubation at 4°C for 10 min. Permeabilized cells were harvested by centrifugation at 300 x *g* for 5 min, and washed twice with BD stain buffer. 10^6 cells were incubated with 50 μl of one of the following antibodies, at 4°C for 45 min: phospho-ERK1/2-AlexaFluor488 (Cell Signaling #4374) at 1:25 dilution; phospho-p38(pT180/pY182)-PE (BD Biosciences 612565) at 1:2 dilution; and phospho-NFκB (Ser536) (Cell Signaling #3033) at 1:200 dilution. Cells were then washed twice with BD stain buffer and, in the case of the phospho-NFκB stained cells, incubated with 50 μl of (1:1000) goat anti-rabbit secondary antibody conjugated to AlexaFluor488 (Invitrogen #11008) at 4°C in the dark for 30 min.

All stained samples were resuspended in 250 μl BD staining buffer for analysis on the BD FACscan flow cytometer.

Figures

Fig. 1. Effect of LPS dose and chemotype on activation of the TLR4-MD2 receptor complex. RAW264.7 macrophages were challenged with different doses (100 pM to 1 µM, 10X dilution series) of LPS derived from *E. coli* O55:B5 (Ec), *S. enterica* serotype minnesota Re 595 (Se), and *F. tularensis novicida* Utah 112 (Ft). At the times indicated, the cells were harvested; stained with PE-labeled MTS510 antibody, which specifically recognizes inactive TLR4-MD2 receptor complexes [J Exp Med 198:1035]; and relative fluorescence intensities (RFIs, expressed in arbitrary units) of individual cells measured by flow cytometry. **A.** Histograms showing mean RFIs measured in a representative experiment. **B.** Bar-graphs showing the medians of normalized mean RFIs (MRFIs, expressed in arbitrary units), and standard errors, calculated from data generated in three independent experiments. The background of each bar-graph is partially shaded to facilitate comparisons with the others.

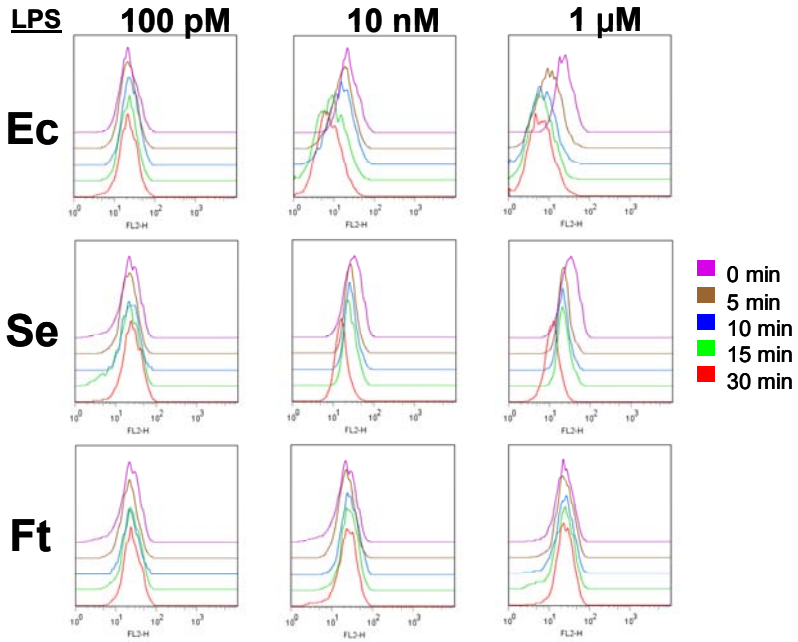

Fig. 2. Effect of LPS dose and chemotype on activation of TLR4 network node NFκB. RAW264.7 macrophages were challenged with different doses (100 pM to 1 μM, 10X dilution series) of LPS derived from *E. coli* O55:B5 (Ec), *S. enterica* serotype minnesota Re 595 (Se), and *F. tularensis novicida* Utah 112 (Ft). At the times indicated, the cells were harvested; stained with Alexa488-labeled anti-RelA-P antibody; and relative fluorescence intensities (RFIs, expressed in arbitrary units) of individual cells measured by flow cytometry. **A.** Histograms showing mean RFIs measured in a representative experiment. **B.** Bar-graphs showing the medians of normalized mean RFIs (MRFIs, expressed in arbitrary units), and standard errors, calculated from data generated in three independent experiments. The background of each bar-graph is partially shaded to facilitate comparisons with the others.

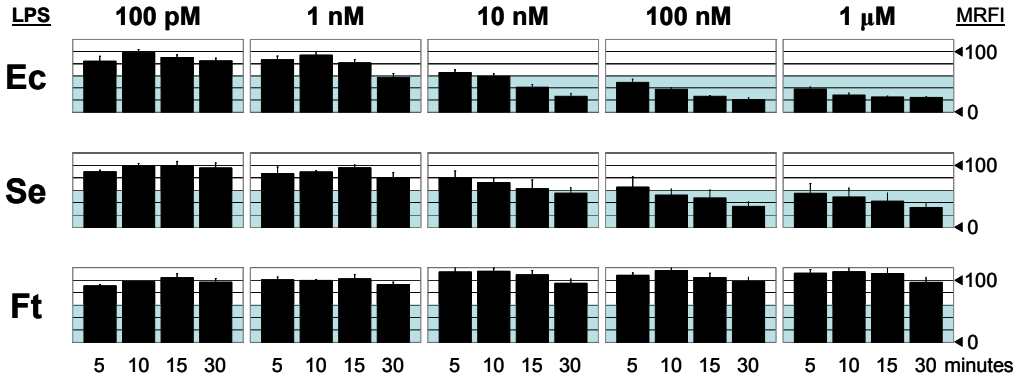

Fig. 3. Effect of LPS dose and chemotype on activation of TLR4 network nodes p38, ERK, IκB*α*, and IRF3. RAW264.7 macrophages were challenged with different doses (100 pM to 1 μM, 10X dilution series) of LPS derived from *E. coli* O55:B5 (Ec), *S. enterica* serotype minnesota Re 595 (Se), and *F. tularensis novicida* Utah 112 (Ft). At the times indicated, the cells were harvested, lysed in the presence of protease and phosphatase inhibitors, and the extracts examined by Western analysis, using antibodies to detect: **A.** Total and phosphorylated p38; **B.** Total and phosphorylated ERK; **C.** Total IκBα; and **D.** Total and phosphorylated IRF3. All images are representative of results

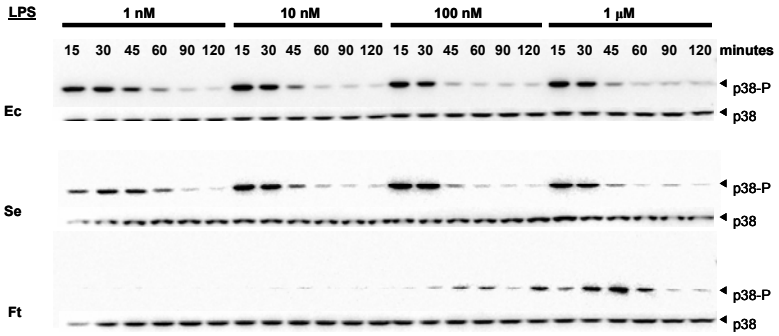

generated in three independent experiments.

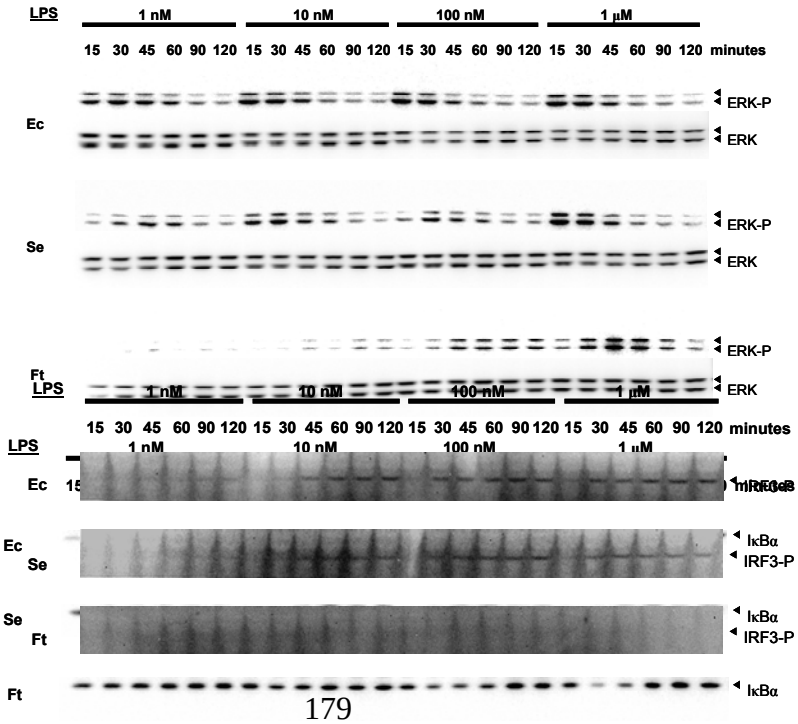

Fig. 4. Effect of LPS dose and chemotype on production of cytokines. Conditioned media were harvested from the RAW264.7 cultures described in the legend of Fig. 2, and their cytokine content measured by ELISA. **A.** IL-6 production in response to different doses of *E. coli* O55:B5 (Ec), *S. enterica* serotype minnesota Re 595 (Se), and *F. tularensis novicida* Utah 112 (Ft) LPS. **B.** Production of eight cytokines in response to different doses of Ec, Se, and Ft LPS.

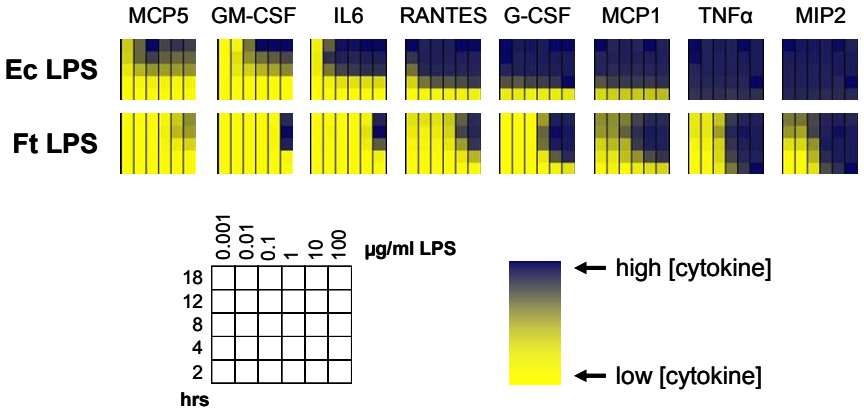

Distribution:

1	MS 9291	Glenn Kubiak	8600
1	MS 9004	Malin Young	8620
5	MS 9291	Anup Singh	8621
1	MS9018	Central Technical Files	8945-1
2	MS0899	Technical Library	9616
1	MS0188	D. Chavez, LDRD Office	1030
1	MS 9121	Jill Hruby	8100
1	MS 9121	Duane Lindner	8120